

Approved for distribution

SIMULATION OF RAM-ACCELERATOR FLOWFIELDS

by

Vincent Gregory Weirs

A thesis submitted to the Graduate Faculty of
North Carolina State University
in partial fulfillment of the
requirements for the degree of
Master of Science

Department of Mechanical and Aerospace Engineering

Raleigh, North Carolina
September 1994

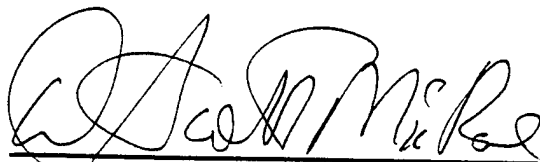
Approved by:



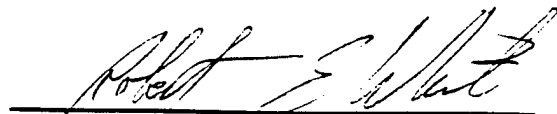
Dr. Graham V. Candler
Advisory Committee Co-Chairman



Dr. Fred R. DeJarnette
Advisory Committee Co-Chairman



Dr. D. Scott McRae
Advisory Committee Member



Dr. Robert E. White
Advisory Committee Minor Representative

ABSTRACT

Weirs, Vincent Gregory. Simulation of Ram-Accelerator Flowfields (Under the direction of Dr. Graham V. Candler)

Ram-accelerators are devices that use combustion to accelerate projectiles to high velocities. Shaped projectiles are propelled through an accelerator tube by expansion of combustion products. Ignition of the premixed fuel and oxidizer is shock-induced. Tailoring the shape of the projectile results in improvements in performance. In this research numerical simulations of the reacting flowfield surrounding the projectile are obtained and analyzed.

Computational Fluid Dynamics (CFD) methods are used to solve the extended Navier-Stokes equation set. Chemical kinetics are modelled by a quasi-global reaction mechanism including 10 species and 12 reactions. Flow is assumed to be laminar. The governing equations are discretized using a finite-volume formulation. Inviscid fluxes are calculated using a Roe-TVD scheme, while standard central differences are used for the viscous terms. A modified form of the diagonal implicit method is used to advance the solution from initial conditions to the steady state. Some species mass conservation equations are replaced by elemental mass conservation equations to improve convergence. As a whole, the simulations demonstrate the value of CFD to the aerospace engineering field. Physical models are evaluated, numerical methods are tested, and flow phenomena are analyzed.

In the course of the research, the advantages and drawbacks of the quasi-global mechanism are exhibited. Compared to a more detailed model the reaction front is smeared, and the model must be calibrated with established data. However, the quasi-global mechanism offers reasonable accuracy at a significantly lower computational cost than more detailed models.

More research must be devoted to the modified diagonal implicit scheme. For some choices of replaced species, the method allows negative mass fractions to develop in the evolution of the simulations. These negative fractions can persist and may remain in the obviously aphysical steady state solution. Careful testing was done to ensure the

difficulties were avoided in the results presented in this thesis. However, a thorough inquiry must be made to expose the underlying problems with the modified diagonal implicit scheme.

The ram-accelerator simulations assess the performance of the double-cone projectile geometry. The double-cone forebody was proposed to delay unstarts to higher Mach numbers. No unstarts were observed for Mach numbers ranging from 7 to 15. The simulations show the projectile performs as designed. A large separated region of flow is located behind the projectile shoulder. It is the result of a shockwave/boundary layer interaction on the afterbody. The size of the separation is affected by the ignition location. The separation is largest when combustion and consequent energy release occurs only downstream of the region; for that situation the expansion of combustion product enhances the shockwave/boundary layer interaction. Further numerical studies are necessary to assess performance for different fill pressures and gas mixtures. More detailed physical models could also be included.

**SIMULATION OF
RAM-ACCELERATOR FLOWFIELDS**

by

Vincent Gregory Weirs

A thesis submitted to the Graduate Faculty of
North Carolina State University
in partial fulfillment of the
requirements for the degree of
Master of Science

Department of Mechanical and Aerospace Engineering

Raleigh, North Carolina
September 1994

Approved by:



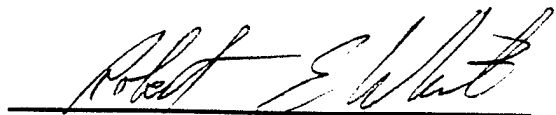
Dr. Graham V. Candler
Advisory Committee Co-Chairman



Dr. Fred R. DeJarnette
Advisory Committee Co-Chairman



Dr. D. Scott McRae
Advisory Committee Member



Dr. Robert E. White
Advisory Committee Minor Representative

BIOGRAPHY

Vincent Gregory Weirs was born in Greenwich, Connecticut on October 25, 1969, to Vincent and Joanna Weirs. He grew up in High Point, North Carolina, with his parents and brother Alan. He earned a Bachelor of Science degree in Aerospace Engineering from North Carolina State University in 1991. After completing this thesis Greg will begin work on a Doctor of Philosophy degree, also in Aerospace Engineering, at the University of Minnesota in Minneapolis.

ACKNOWLEDGEMENTS

This thesis would not have been possible without the wisdom and experience of many people. I thank Dr. Graham Candler for his expertise, but in particular for his patience, guidance, and contagious enthusiasm. I also thank Dr. Scott McRae for his knowledge of CFD and his instructive habit of answering my questions with some of his own. I am indebted to Dr. Fred DeJarnette for his advice and for the Mars Mission Research Center facility at NCSU; I fear I will not soon have an office as comfortable as the one I now leave. I appreciate the unending efforts of Dr. Hassan Hassan in bettering the department and thank him for teaching me about combustion, among other things. I thank Dr. Bob White for his lessons in vector and parallel computing algorithms and for serving as my minor representative even if there is no formal record of my attendance in his classes.

I am also grateful to my fellow students for their support and encouragement. Drs. Basil Hassan and Jim Keenan, almost Dr. Rick Perrell, and David Hash shared their frustrations, their successes, and their coding tricks. I thank Mary Hudson for her ability to put things in perspective. I thank Patrick Canupp for seeing me through the worst. Finally, my appreciation for the love and support of my family, which has been critical to the completion of this degree, cannot be understated.

I am indebted to Ken Jones for the use of his workstation. I am also thankful for the support I have received from the Mars Mission Research Center at North Carolina State University, funded by NASA under Grant No. NAGW-1331. I gratefully acknowledge the Department of Defense for the National Defense Science and Engineering Graduate Fellowship I was awarded. Last but not least, I thank the Southeastern Consortium for Electrical Engineering Education (SCEEE), which administers that fellowship, for their efforts and patience.

TABLE OF CONTENTS

	<i>Page</i>
LIST OF TABLES	vi
LIST OF FIGURES	vii
LIST OF SYMBOLS	viii
I BACKGROUND AND MOTIVATION	1
I.1 Introduction	1
I.2 The Ram-Accelerator Concept	1
I.3 Unstarts	4
I.4 The Scope of Present Work	6
II GOVERNING EQUATIONS	8
II.1 Introduction	8
II.2 Conservation Equations for Reacting Flow	8
II.3 Equation of State	13
II.4 Constitutive Relations	15
II.5 Transport Properties	16
II.6 Chemical Source Terms	19
II.7 Boundary Conditions	24
III NUMERICAL METHOD	26
III.1 Introduction	26
III.2 Vector Form of the Governing Equations	26
III.3 Finite Volume Discretization	28
III.4 Evaluation of the Explicit Terms	32
III.5 Evaluation of the Implicit Terms	39
III.6 Solution Advancement	44
III.7 Boundary Conditions	45
IV BLUNT BODY SIMULATIONS	48
IV.1 Introduction	48
IV.2 Flow Conditions	48
IV.3 Discussion of the Simulations	50
V RAM-ACCELERATOR SIMULATIONS	55
V.1 Introduction	55
V.2 Ram-Accelerator Geometry and Simulation Conditions	55
V.3 Discussion of the Flowfields	57
V.4 Discussion of the Separation Bubble	63
V.5 Unstart Characteristics	65

VI	CONCLUSIONS	67
VI.1	Conclusions	67
VI.2	Future Work	68
	REFERENCES	71
A	THE ELEMENTAL FORMULATION	77
B	PHYSICAL CONSTANTS	80
C	GENERALIZED COORDINATE TRANSFORMATION	85
D	DIAGONALIZATION OF THE FLUX JACOBIANS	88

LIST OF TABLES

<i>Table</i>		<i>Page</i>
B.1	Molecular Constants	81
B.2	Molecular parameters for Lennard-Jones 6-12 potentials	82
B.3	Collision integral curve-fit coefficients	82
B.4	Polynomial coefficients for Gibbs' free energies: low temperature range	83
B.5	Polynomial coefficients for Gibbs' free energies: high temperature range	83
B.6	Quasi-global methane reaction mechanism	84

LIST OF FIGURES

<i>Figure</i>		<i>Page</i>
1.1	Schematic of a generic, ram-accelerator projectile flowfield.	2
1.2	Double-cone projectile geometry.	6
3.1	Property value and grid definition locations for a representative cell.	29
4.1	Blunt body mesh and representative temperature contours.	49
4.2	Pressure profile comparison using the original rate.	52
4.3	Temperature profile comparison using the original rate.	52
4.4	Pressure profile comparison using the doubled rate.	53
4.5	Temperature profile comparison using the doubled rate.	53
5.1	Ram-accelerator computational mesh and projectile geometry.....	56
5.2	Features of the ram-accelerator flowfield.	57
5.3	Mach number contours.	58
5.4	Density contours.	59
5.5	Methane mass fraction contours.	60
5.6	Carbon dioxide mass fraction contours.	61
5.7	Mach number contours for Mach 17 and Mach 19 cases.	62
5.8	Methane mass fraction contours for Mach 17 and Mach 19 cases.	63
5.9	Mach number contours and streamlines illustrating the separation bubble....	64
5.10	Streamlines showing expansion for nonreacting and reacting Mach 9 flow....	65
C.1	Surface cosines for a representative mesh cell.	86

LIST OF SYMBOLS

Roman Symbols

A^n, B^n	Flux vector Jacobians in the ξ - and η -directions, respectively
A_{\pm}^n, B_{\pm}^n	Split-flux Jacobians in the ξ - and η -directions, respectively
A_r	Arrhenius pre-exponential coefficient for reaction r
a	Speed of sound of the gas
C_i	Chemical symbol of species i
\bar{C}_v	Constant-volume, translational-rotational specific heat for the gas mixture
$c_{v,s}$	Constant-volume, translational-rotational specific heat of species s
$c_{v,trans,s}$	Constant-volume, translational specific heat of species s
$c_{v,rot,s}$	Constant-volume, rotational specific heat of species s
$c_{v,vib,s}$	Constant-volume, vibrational specific heat of species s
D	Common diffusion coefficient for all species
D_s	Binary diffusion coefficient of species s
$D_{i,j}$	Diagonal matrix in the solution advancement method
Da	Grid Damköhler number
E_s	Total energy per unit volume of species s
$E_{v,s}$	Vibrational energy per unit volume of species s
F, G	Respectively, flux vectors in the x - and y -coordinate directions
F_I, G_I	Inviscid components of F and G , respectively
F_V, G_V	Viscous components of F and G , respectively
F', G'	Respectively, flux vectors in the ξ - and η -coordinate directions
ΔG_r^0	Difference in Gibbs' free energies of reactants and products of reaction r
g_s^0	Molar standard Gibbs' free energy of species s
h_s	Specific enthalpy of species s
h_s^0	Specific enthalpy of formation of species s
\hat{i}, \hat{j}	Unit vectors in the x - and y -directions, respectively
il	Number of grid points in the ξ -direction
jl	Number of grid points in the η -direction

$K_{eq,r}$	Equilibrium constant based on concentration for reaction r
k_B	Boltzmann constant
$k_{f,r}$	Forward reaction rate constant for reaction r
$k_{b,r}$	Backward reaction rate constant for reaction r
Δn_r	Difference in number of moles of reactants and products of reaction r
M	Transformation matrix between conserved and primitive variables
M_∞	Free stream Mach number
M_s	Molecular weight of species s
P_A, P_B	Matrices of the right eigenvectors of A and B , respectively
$P_{s,i}$	Momentum exchange term for species s
p	Pressure of the gas mixture
p_s	Partial pressure of species s
Q_s	Energy exchange term for species s
$q_{t,j}$	Total heat flux vector of the gas mixture
$q_{t,s,j}$	Total heat flux vector of species s
R	Universal gas constant
\bar{R}	Specific gas constant for the gas mixture
RR_r	Reaction rate of reaction r
r_A, r_B	Spectral radii of A and B , respectively
\bar{S}	Grid cell surface vector
$S_{i+1/2}$	Area of the $i + 1/2$ cell face
S_i	Average of the areas of the $i + 1/2$ and $i - 1/2$ cell faces
Sc	Schmidt number
s'_{ix}, s'_{iy}	Direction cosines for the $i + 1/2$ cell face
s'_{jx}, s'_{jy}	Direction cosines for the $j + 1/2$ cell face
T^*	Reduced temperature
T	Temperature of the gas mixture
t	Time coordinate
Δt	Time step
U	Vector of conserved variables

u	Mass-averaged velocity in the x -direction
u'	Mass-averaged contravariant velocity in the ξ -direction
u_j	Mass-averaged velocity vector
u_s	Diffusion velocity in the x -direction for species s
\tilde{u}_e	Diffusion velocity in the x -direction for element e
$u_{s,j}$	Velocity vector of species s
V	Vector of primitive variables
v	Mass-averaged velocity in the y -direction
v'	Mass-averaged contravariant velocity in the η -direction
v_s	Diffusion velocity in the y -direction for species s
\tilde{v}_e	Diffusion velocity in the y -direction for element e
$v_{s,j}$	Diffusion velocity vector of species s
$\tilde{v}_{e,j}$	Diffusion velocity vector of element e
\dot{w}_s	Chemical source term for species s
X_s	Mass fraction of species s
x, y	Coordinate directions in physical space
x_j	Generalized coordinate in index notation
Y_s	Mole fraction of species s
y_c	Cell centroid radius for axisymmetric calculations
Z^n	Chemical Jacobian

Greek Symbols

$\alpha_{e,s}$	Coefficients of the linear combination relating the elemental densities to the species densities
$\beta_{s,t}$	Coefficients of the linear combination relating the replaced species densities to the elemental and retained species densities
Γ	Ratio defining the Roe-average state
γ	Ratio of specific heats
$\delta_{i,j}$	Kronecker delta; $\delta_{i,j} = 1$ if $i = j$, but 0 otherwise
ϵ_s, σ_s	Lennard-Jones potential parameters for species s
η_r	Arrhenius temperature exponent for reaction r

$\theta_{d,r}$	Arrhenius characteristic temperature of dissociation for reaction r
$\theta_{v,s,m}$	Characteristic temperature of vibration of mode m of species s
κ	Coefficient of heat transfer for the gas mixture
κ_s	Coefficient of heat transfer for species s
Λ_A, Λ_B	Diagonal matrices containing eigenvalues of, respectively, A and B
λ	Coefficient of bulk viscosity
μ	Coefficient of viscosity for the gas mixture
μ_s	Coefficient of viscosity for species s
$\nu_{i,r}', \nu_{i,r}''$	Stoichiometric coefficients of species i as, respectively, a reactant and a product in reaction r
ξ, η	Coordinate directions in computational space
ρ	Mass density of the gas mixture
ρ_s	Mass density of species s
$\tilde{\rho}_e$	Mass density of element e
$\tau_{i,j}$	Viscous stress tensor for the gas mixture
$\tau_{s,i,j}$	Viscous stress tensor for species s
τ_{fluid}	Approximate time for a particle to cross a grid cell
$\tau_{rxn,f,r}$	Characteristic time scale of the forward reaction for reaction r
$\tau_{rxn,b,r}$	Characteristic time scale of the backward reaction for reaction r
τ_s	Chemical time scale for species s
$\Omega_{i,j}$	Volume of cell i, j
$\Omega_{ss}^{(2,2)*}$	Elastic collision integral

Subscripts

i, j	Integers denoting values of ξ and η coordinates
∞	Denotes free stream value

Superscripts

n	Denotes iteration level
r	Switch specifying 2-D or axisymmetric coordinates; $r = 0$ for 2-D, $r = 1$ for axisymmetric

CHAPTER I

BACKGROUND AND MOTIVATION

I.1 Introduction

A ram-accelerator is a device for accelerating projectiles to high velocities. It relies on chemical energy release in a thermodynamic cycle similar to that of a ramjet engine. Practical research and development has been underway for less than a decade. While the concept has been proven, there are still many technical issues to resolve. The operation cycle can break down for several reasons, and the projectile consequently loses thrust.

Numerical simulations are valuable to the ram-accelerator and computational fluid dynamics (CFD) communities. To the former, information difficult or impossible to measure experimentally is made available. In this thesis, the conditions which lead to 'unstarts' are sought. CFD benefits from the validation of numerical models; this will become apparent in the following chapters.

In this chapter the ram-accelerator is described; the theory underlying its operation and the applications of such a device are presented. Several proposed unstart mechanisms are described. During the course of the discussion the experimental and numerical investigations to date are reviewed. Finally, the objectives of this thesis are outlined.

I.2 The Ram-Accelerator Concept

The ram-accelerator concept details a gasdynamic method of accelerating projectiles. The components consist of a long, constant-diameter tube and a shaped projectile. Initially the accelerator tube is filled with premixed ratios of fuel, oxidizer, and, in most cases, a diluent. The mixture is quiescent and pressurized to between 20 and 50 *atm*. The projectile at its widest has a cross-sectional area less than that of the tube. The forebody is generally conical. The afterbody usually tapers to a circular base. Fins on the afterbody align the projectile with the tube.

The projectile enters the tube at a supersonic velocity, generally between Mach 2 and Mach 4; an external means of acceleration, such as a traditional powder gun or light gas

gun, is used as a preaccelerator. Once the projectile enters the accelerator tube, an oblique shock forms off the nose. It reflects off the tube wall and the projectile, compressing and heating the gas. Eventually these shockwaves raise the temperature enough to ignite the fuel, and chemical energy is released into the flow. As the burned gas expands, it accelerates the projectile. A schematic is shown in Figure 1.1.

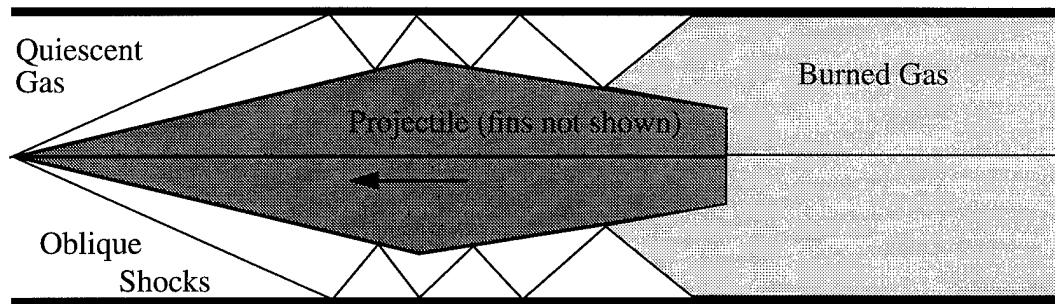


Figure 1.1 Schematic of a generic, ram-accelerator projectile flowfield.

The accelerator tube is initially pressurized, with thin diaphragms sealing the ends. Usually the tube is composed of separate sections, which can be individually pressurized with different gas mixtures. By staging the fill pressures and mixtures, the acceleration of the projectile can be controlled.

Three modes of ram-accelerator operation have been distinguished.¹ They are based on the speed of the projectile relative to the Chapman-Jouget (C-J) detonation wave speed. The subdetonative regime extends up to 90% of the C-J velocity. Combustion is subsonic (in the projectile frame of reference) and occurs primarily in the wake. One or several projectile lengths downstream, the flow is thermally choked. The transdetonative regime extends from 90% to 110% of the detonation wave speed; combustion may be of subsonic, supersonic, or mixed character. In the superdetonative regime the projectile velocity is above 110% of the C-J speed, and generally combustion is supersonic. Note that these regimes are only roughly defined, and other modes have been proposed.²

1. Hinkey, Burnham, and Bruckner (1992) describe these operational modes.

2. See, for example, Hertzberg, Bruckner, and Bogdanoff (1988).

Theoretically projectiles can be accelerated to velocities as high as 10 *km/sec*. So far velocities to ~ 2.7 *km/sec* have been obtained in the 38 *mm*-diameter tube at the University of Washington,³ which has the oldest, most developed ram-accelerator research program. The majority of experimental work has been on the subdetonative regime. Since the demonstration of the concept, experimental research has been initiated at the U. S. Army Research Laboratory (ARL),⁴ where a 120 *mm* accelerator has been fired, and at the French-German Research Institute of Saint-Louis (ISL),⁵ where a 90 *mm* ram-accelerator is being developed.

The flowfield within the ram-accelerator tube is complex. Besides the series of shock-waves, there are contact surfaces, expansions, boundary layers, flow separations, chemical induction zones, and energy-release fronts. All of these features interact with each other, further complicating the analysis. Numerical simulations must accurately resolve these flow phenomena and interactions. Computational flowfield solutions carried out at ARL⁶ show that, in general, a nonequilibrium treatment of combustion chemistry is required. At Science Applications International Corp. (SAIC)⁷ intermolecular force effects (real gas effects) have been shown to be significant. Additional simulations have been carried out by Amtec Engineering,⁸ Yungster at the University of Washington and later at NASA-Lewis⁹, and a group at the Naval Research Laboratory (NRL).¹⁰ Almost all researchers have found that viscous terms must be included in the simulations and that turbulence modelling affects the results. While the fins on the projectile make the flowfield three-dimensional, most numerical studies assume axisymmetric flow. Despite this simplification, good agreement with experimental data has been obtained.

Several applications of the concept have been proposed. One of the best uses for the

-
3. See Knowlen, Higgins, and Bruckner (1994).
 4. Recent publications are Kruczynski (1991) and Kruczynski, Liberatore, and Kiwan (1994).
 5. See Srulijes, Smeets, and Seiler (1992).
 6. See the series of references by Nusca (1991), (1993) and (1994), and Kruczynski and Nusca (1992).
 7. See Sinha, York, Dash, Drabczuk, and Rolader (1992).
 8. See Soetrisno and Imlay (1991) and Soetrisno, Imlay and Roberts (1992) and (1993).
 9. See Yungster, Eberhardt, and Bruckner (1991), Yungster (1991) and (1992), and Yungster and Rabinowitz (1993).
 10. There are a series of papers by Li, Kailasanath, and Oran, et. al., in the list of references.

ram-accelerator is as a research tool. As a means of accelerating masses up to 10 km/sec, the device can provide experimental hypersonic flow data, supplementing ballistic ranges, shock tubes, and wind tunnels. Since, by its nature, it relies on shock-induced, and at transdetonative and superdetonative speeds, supersonic combustion, the ram-accelerator is a valuable testbed for fundamental research of those phenomena. Research applications are not limited to gas dynamics; materials analyses and impact studies are also plentiful. A key advantage of the concept is that scaling to large projectile diameters and masses is straightforward. Other hypervelocity acceleration concepts suffer from either power or material property limitations. Because scaling is not an issue, the ram-accelerator is being considered as an economical method of placing acceleration-insensitive payloads into orbit.

I.3 Unstarts

The establishment of a steady, thrust-producing flowfield upon entrance of the accelerator tube is a significant achievement.¹¹ All the intricacies of the starting process are not yet understood. Typically experimental facilities use a proven 'starting' mixture in the first tube section to ensure a successful injection and to isolate the starting transients from the remainder of the tube.¹² The dynamics of the projectile entering the accelerator are not considered here.

Once a stable flowfield is attained, steady operation may be interrupted for a number of reasons. The deterioration of the cycle and consequent loss of thrust is referred to as unstart. Structural failure of the projectile is one reason for unstarts. Recent efforts at the University of Washington¹³ have demonstrated that aluminum forebodies can not withstand the high heat transfer of some gas compositions. Operation may also be inhibited by projectile canting; if the axes of the accelerator tube and projectile are not

11. Some difficulties experienced at ARL are described in Kruczynski, Liberatore, and Kiwan (1994).

12. See Knowlen, Higgins, and Bruckner (1994).

13. Experimental documentation of structural failures is given in Knowlen, Higgins, and Bruckner (1994). A numerical simulation of the heating of a projectile forebody is presented in Chew and Bruckner (1994).

aligned, variations in the shock strength from the projectile tip can ignite the mixture prematurely. Projectiles with five fins have shown better performance than four-fin types because they do not allow as much canting.¹⁴ Numerical simulations confirm the sensitivity of stable operation to slight errors in projectile alignment.¹⁵

Unstarts can result even for well-aligned, structurally sound projectiles. Such gasdynamic unstarts generally fall into one of three categories, all of which end with significant energy release ahead of the projectile. Because the energy is released prematurely high pressures are experienced on the forebody, and thrust is lost. In the first mechanism, a detonation wave forms in the wake and propagates upstream past the projectile body. It either remains attached to the projectile nose or propagates through the tube ahead of the projectile. Behind this detonation wave all the fuel is burned, so the heat release occurs too early. This type of unstart generally occurs when the flow in the wake is thermally choked.

In the second mechanism, the projectile boundary layer is heated by the impingement of a shockwave on the afterbody.¹⁶ Ignition occurs at the impingement point and combustion propagates upstream through the boundary layer to the forebody. As combustion moves along the projectile, it spreads to the rest of the flowfield. The third class of gasdynamic unstarts sets an upper speed limit on the projectile. Above some speed the oblique shockwave formed at the nose is strong enough to ignite the flow. When this happens, the energy release may strengthen the shock and form a detonation wave that propagates upstream. Alternatively the energy release raises pressure on the forebody enough to decelerate the projectile. It is important to note that combustion in the forebody boundary layer or behind the initial shockwave does not necessarily result in an unstart. If the energy release is not too great, the rest of the flowfield will not ignite until further downstream. Ideally, however, there is no combustion ahead of the projectile.

For the second and third unstart mechanisms described, projectile geometry modifications have been proposed to delay or eliminate premature combustion. Rom and coworkers¹⁷ propose a forward facing step be included at the projectile shoulder. This step causes

14. See Hinkey, Burnham and Bruckner (1992).

15. See Soetrisno, Imlay, and Roberts (1993).

16. This mechanism can be seen in the numerical simulations by Yungster (1991).

17. See Rom and Avital (1992), and Tivanov and Rom (1993).

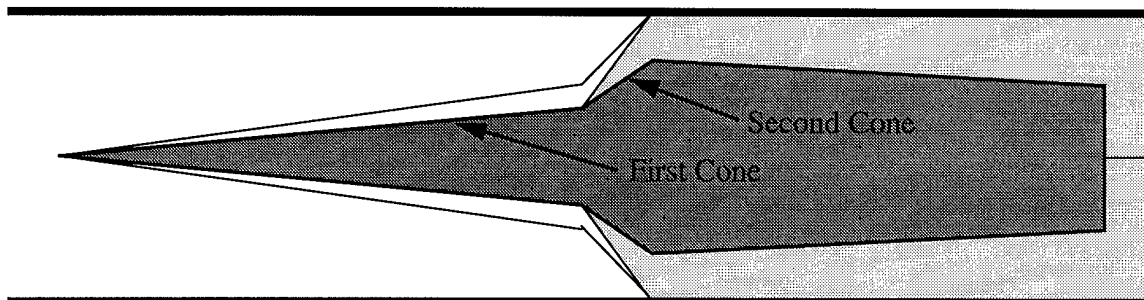


Figure 1.2 Double-cone projectile geometry.

a strong shock to form, which ignites the gas at the desired location. A similar variation offered by Yungster¹⁸ consists of a double-cone forebody, shown in Figure 1.2. (The fins are not shown in the figure.) The first cone angle is small to weaken the initial shock and reduce drag. At some point downstream the cone angle steepens, forming the second cone. The shock formed by the second cone is strong enough to ignite the gas mixture.

I.4 The Scope of Present Work

Ideally the numerical simulation of ram-accelerator flowfields would include models for all the physical phenomena that occur. A detailed chemical model including a multitude of species with reliable, experimental validation at ram-accelerator conditions would be employed. The effects of intermolecular forces would be included because of the high pressures encountered. Turbulence would also be accurately modelled. The physical domain, including the wake, would be represented using a fine mesh for the entire flowfield. The simulation would be fully three-dimensional and time-accurate.

Unfortunately, computer speed and memory are limited; some models are too expensive computationally. Others are of limited or unverified accuracy. As a result compromises are made to reduce the complexity and cost of the simulations. Despite the compromises reasonably accurate flowfield solutions have been obtained by many researchers. Comparison with experimental data demonstrates that the salient physics are included in the models and important trends can be predicted.

18. See Yungster (1993).

In this thesis ram-accelerator flowfields are simulated over a range of velocities. The objective is an assessment of the unstart characteristics of the double-cone geometry. In particular, interest is centered on the unstart mechanisms involving combustion in the forebody boundary layer or ignition by the initial shockwave. The simulations are axisymmetric, laminar, steady, and do not encompass the projectile wake. Including the wake dramatically increases the cost of the simulations but does not play a significant role in the unstart mechanisms to be studied. For similar reasons fins on the afterbody of the projectile are omitted. The gas mixture is assumed to be thermally perfect, reacting methane-air.

The solution advancement scheme has been used for reentry flows, but not for combusting flows. A secondary objective is to further establish the 'modified diagonal implicit' scheme.¹⁹ The simulations show steady-state solutions for two reasons. Unsteady simulations demand more CPU time and more memory for storage of intermediate solutions. The diagonal implicit scheme is not time accurate and would have to be replaced; further validation would not be possible. The details of the physical models, the numerical solution technique, and the resulting flowfields are discussed in the following chapters.

19. The modified diagonal implicit scheme is presented in Candler and Olynick (1991) and Hassan, Candler, and Olynick (1992), as well as in Chapter III.

CHAPTER II

GOVERNING EQUATIONS

II.1 Introduction

In this chapter, the equations governing chemically reacting flowfields are introduced. The assumptions in the equations are also discussed. Some assumptions are inherent in the equations themselves, while in other cases simplifications are made to make solution feasible.

The coupled, nonlinear, partial differential equations that describe the conservation of mass, momentum, and energy are collectively called the Navier-Stokes equations. They are augmented for application to chemically reacting flows. The definition of the total energy and a gas law specify the state of the gas. Constitutive relations provide expressions for diffusion of mass, momentum, and energy. The evaluation of empirical coefficients required for these expressions is explained in the section on Transport Properties. The models for mass transfer between chemical species are described in the Chemical Source Terms section. Finally, the boundary conditions for ram-accelerator flowfields are examined.

II.2 Conservation Equations for Reacting Flow

The spatial and temporal evolution of fluid properties is described by the Navier-Stokes equations. This set of nonlinear, partial differential equations specifies the conservation of mass, momentum, and energy. The fundamental assumption in the equations is that a continuum description of the gas is applicable. For flows in which the characteristic length scale is similar to a mean free path, a particle description is appropriate. For ram-accelerator flowfields, and combustion flowfields in general, gas densities are high enough to apply the Navier-Stokes set. By the same reasoning, no-slip conditions are valid at gas-solid interfaces, and linear constitutive relations are accurate.

The Navier-Stokes equations can be augmented to model chemically reacting flows. To do so, the conservation equations are applied to each chemical species in a

multi-component mixture and appropriate source terms are added to account for mass, momentum, and energy exchanges between species. The Navier-Stokes equation set can also be extended to model thermal nonequilibrium, the effects of an electric field, and radiation, but these effects are not included in the present work.

At this point the Navier-Stokes equations, expressed in index notation, are introduced. The natural extension of index notation is to Cartesian systems although it can be applied to any orthogonal coordinate system. In Chapter III notation specific to two-dimensional and axisymmetric geometries will be addressed. The conservation of mass for species s is expressed as

$$\frac{\partial \rho_s}{\partial t} + \frac{\partial}{\partial x_j} (\rho_s u_{s,j}) = \dot{w}_s. \quad (2.2.1)$$

The conservation of momentum for species s is given by

$$\frac{\partial}{\partial t} (\rho_s u_{s,i}) + \frac{\partial}{\partial x_j} (\rho_s u_{s,i} u_{s,j} + p_s \delta_{i,j} + \tau_{s,i,j}) = P_{s,i}, \quad (2.2.2)$$

and the conservation of energy is given by

$$\frac{\partial}{\partial t} (\rho_s E_s) + \frac{\partial}{\partial x_j} [(\rho_s E_s + p_s) u_{s,j} + u_{s,i} \tau_{s,i,j} + q_{t,s,j}] = Q_s. \quad (2.2.3)$$

In theory the above equations could be solved for the species densities, velocities, and energies to obtain flowfield solutions. Clearly the size of the system, and thus the computational expense of the solution, grows rapidly with the number of species. In practice some simplifying assumptions are made to reduce the number of equations.

For a gas model comprised of ns chemical species, there are ns mass conservation equations. For species s , the density is denoted by ρ_s and the velocity in the j^{th} direction is $u_{s,j}$. The net production or destruction due to chemical reactions is \dot{w}_s ; the treatment of \dot{w}_s is elucidated in Section II.6. The species velocities can be rewritten as the mass-averaged velocity, u_j , plus a perturbation called the diffusion velocity, $v_{s,j}$:

$$u_{s,j} = u_j + v_{s,j}. \quad (2.2.4)$$

The diffusion velocity is assumed to be small compared to the mass-averaged velocity, which is defined by

$$u_j = \sum_{ns} \frac{\rho_s}{\rho} u_{s,j} \quad (2.2.5)$$

where the total density is the sum of the species densities,

$$\rho = \sum_{ns} \rho_s. \quad (2.2.6)$$

Substituting the mean and diffusion velocities for $u_{s,j}$ in the species continuity equations,

$$\frac{\partial \rho_s}{\partial t} + \frac{\partial}{\partial x_j} (\rho_s u_j) + \frac{\partial}{\partial x_j} (\rho_s v_{s,j}) = \dot{w}_s. \quad (2.2.7)$$

By summing all the species continuity equations, the conservation of total mass is recovered. This holds because total mass is not created or destroyed by chemical reactions,

$$\sum_{ns} \dot{w}_s = 0, \quad (2.2.8)$$

and because there is no net diffusive flux,

$$\sum_{ns} \rho_s v_{s,j} = 0. \quad (2.2.9)$$

To reduce the number of equations, the species momentum equations are summed in each coordinate direction. Dalton's law of partial pressures states the mixture pressure is the sum of the species pressures:

$$p = \sum_{ns} p_s. \quad (2.2.10)$$

The shear stress for the mixture is also the sum of the species quantities:

$$\tau_{i,j} = \sum_{ns} \tau_{s,i,j}. \quad (2.2.11)$$

With the assumption that all particle collisions are elastic, the sum of the momentum source terms is zero:

$$\sum_{ns} P_{s,i} = 0. \quad (2.2.12)$$

The elastic collision assumption is consistent with the use of the ideal gas equation of state, which is discussed in the next section.

With these relations, the mass-averaged momentum equations are

$$\frac{\partial}{\partial t}(\rho u_i) + \frac{\partial}{\partial x_j}(\rho u_i u_j + p \delta_{i,j} + \tau_{i,j}) = 0. \quad (2.2.13)$$

The symbol $\delta_{i,j}$ is the Kronecker delta. By the mass-averaging, a significant reduction in the number of equations is accomplished. The evaluation of the momentum exchange terms $P_{s,i}$ is no longer required, which is also a notable simplification. However, the diffusion velocities must now be approximated because there are fewer equations than unknowns.

The species energy equations are mass-averaged in the same manner as the momentum equations. Since the total energy is conserved,

$$\sum_{ns} Q_s = 0. \quad (2.2.14)$$

The heat flux vector is the sum of the species contributions:

$$q_{t,j} = \sum_{ns} q_{t,s,j}. \quad (2.2.15)$$

The total energy equation is now written as

$$\frac{\partial}{\partial t}(\rho E) + \frac{\partial}{\partial x_j} \left[(\rho E + p) u_j + u_i \tau_{i,j} + q_{t,j} + \sum_{ns} \rho_s h_s v_{s,j} \right] = 0. \quad (2.2.16)$$

A detailed definition of the total energy per unit mass, ρE , is given in the next section. The evaluation of the heat flux vector, the shear stress tensor, and the diffusion velocities are described in Section II.4.

For reasons which will be thoroughly discussed in Chapter III, some of the species mass conservation equations are replaced by elemental mass conservation equations. Since the species equations implicitly conserve elemental masses, as well as the total mass, the physics described by the equation set are unchanged; the equations have merely been recast in different variables. There are still a total of ns mass conservation equations.

The first ne species mass conservation equations are replaced by elemental mass conservation equations, but the remaining $ns - ne$ species equations are retained. When chemical reactions occur, the elemental masses are not affected; consequently, there are no source terms for the elemental continuity equations:

$$\frac{\partial \tilde{\rho}_e}{\partial t} + \frac{\partial}{\partial x_j} (\tilde{\rho}_e u_j) + \frac{\partial}{\partial x_j} (\tilde{\rho}_e \tilde{v}_{e,j}) = 0. \quad (2.2.17)$$

The density of element e , $\tilde{\rho}_e$, is related to all the species densities by the linear combination

$$\tilde{\rho}_e = \sum_{s=1}^{ns} \alpha_{e,s} \rho_s \quad e = 1, \dots, ne, \quad (2.2.18)$$

where ne is the number of elements. The total density is now defined by

$$\rho = \sum_{e=1}^{ne} \tilde{\rho}_e. \quad (2.2.19)$$

The diffusion velocity for element e , $\tilde{v}_{e,j}$, is related to the species diffusion velocities by

$$\tilde{\rho}_e \tilde{v}_{e,j} = \sum_{s=1}^{ns} \alpha_{e,s} \rho_s v_{s,j} \quad e = 1, \dots, ne. \quad (2.2.20)$$

Given the ne elemental conservation equations and the $ns-ne$ species conservation equations, the replaced species densities can be obtained by

$$\rho_s = \sum_{t=1}^{ne} \beta_{s,t} \tilde{\rho}_t + \sum_{t=ne+1}^{ns} \beta_{s,t} \rho_t \quad s = 1, \dots, ne. \quad (2.2.21)$$

The coefficients $\alpha_{e,s}$ and $\beta_{s,t}$ are functions of the elemental and species molecular weights. The determination of these coefficients is detailed in Appendix A.

With the explicit inclusion of the elemental conservation equations, the conserved variables are the elemental densities, $\tilde{\rho}_e$, $e = 1, \dots, ne$, the retained species densities, ρ_s , $s = ne + 1, \dots, ns$, the momentum in each spatial dimension, ρu_i , and the total energy, ρE . In practice the densities of the replaced species, ρ_s , $s = 1, \dots, ne$, are also calculated because many quantities are more difficult to evaluate in terms of the elemental densities. For this reason the equations in this chapter are expressed in the full set of species densities.

In summary, a set of nonlinear partial differential equations describing fluid flow is presented. The set consists of ns equations for the chemical composition, a momentum

equation for each coordinate direction, and a total energy equation. The governing equations are expressed on a per-unit-volume basis.

Conservation of elemental mass:

$$\frac{\partial \tilde{\rho}_e}{\partial t} + \frac{\partial}{\partial x_j} (\tilde{\rho}_e u_j) + \frac{\partial}{\partial x_j} (\tilde{\rho}_e \tilde{v}_{e,j}) = 0 \quad e = 1, \dots, ne \quad (2.2.22)$$

Conservation of species mass:

$$\frac{\partial \rho_s}{\partial t} + \frac{\partial}{\partial x_j} (\rho_s u_j) + \frac{\partial}{\partial x_j} (\rho_s v_{s,j}) = \dot{w}_s \quad s = ne + 1, \dots, ns \quad (2.2.23)$$

Conservation of momentum:

$$\frac{\partial}{\partial t} (\rho u_i) + \frac{\partial}{\partial x_j} (\rho u_i u_j + p \delta_{i,j} + \tau_{i,j}) = 0 \quad (2.2.24)$$

Conservation of total energy:

$$\frac{\partial}{\partial t} (\rho E) + \frac{\partial}{\partial x_j} \left[(\rho E + p) u_j + u_i \tau_{i,j} + q_{t,j} + \sum_{ns} \rho_s h_s v_{s,j} \right] = 0 \quad (2.2.25)$$

II.3 Equation of State

In this section the relations between the conserved variables and the non-conserved, intensive variables p and T are presented. Once the conserved variables have been calculated, the temperature is determined iteratively from the definition of the total energy. An iterative solution is required because of the treatment of the vibrational energy. The pressure is then determined from the ideal gas law.

In ram-accelerator flowfields, pressures can reach hundreds or even thousands of atmospheres. For such high pressures, intermolecular forces may have a significant effect on the state of the gas. However, the fluid is assumed to be a mixture of thermally perfect gases for simplicity. For such a mixture, the ideal gas law relates the pressure to the temperature, T , and density:

$$p = \sum_{ns} p_s = \sum_{ns} \rho_s \frac{R}{M_s} T, \quad (2.3.1)$$

where R is the universal gas constant and the molecular weight for a species is denoted

M_s .

The total energy is comprised of translational-rotational, vibrational, chemical, and kinetic components:

$$\rho E = \sum_{s=1}^{ns} \rho_s c_{v,s} T + \sum_{s=1}^{nv} \rho_s E_{v,s} + \sum_{s=1}^{ns} \rho_s h_s^o + \sum_{s=1}^{ns} \rho_s \frac{u_i u_i}{2}. \quad (2.3.2)$$

The energy conservation equation requires the specific enthalpy, h_s , for each species. This is given by

$$h_s = c_{v,s} T + E_{v,s} \Big|_{s \leq nv} + h_s^o + \frac{p_s}{\rho_s}. \quad (2.3.3)$$

In both these equations, $c_{v,s}$ is the constant-volume, translational-rotational specific heat. It is a function of the molecular weight and internal structure of the species. Contributions from the translational and rotational modes are summed:

$$c_{v,s} = c_{v,trans,s} + c_{v,rot,s}. \quad (2.3.4)$$

The contribution to $c_{v,s}$ from the fully excited translational mode is the same for all species, $\frac{3R}{2M_s}$. The rotational mode is also assumed to be fully excited:

$$c_{v,rot,s} = \begin{cases} 0 & \text{for monatomics} \\ \frac{R}{M_s} & \text{for diatomics and linear polyatomics} \\ \frac{3R}{2M_s} & \text{for 3-D polyatomics} \end{cases}. \quad (2.3.5)$$

There are three rotational modes for rotational energy for molecules, each of which contributes $\frac{1R}{2M_s}$ to the specific heat. Because rotation about the bond-axis is insignificant compared to the other two axes for diatomic and linear polyatomic molecules, only two modes contribute to the rotational specific heat. Monatomics have no internal structure and thus store no rotational energy. Note that the vibrational modes also contribute to the heat capacities of molecules, but this is accounted for in the vibrational energy term discussed below.

The vibrational energy modes are partially excited. The total vibrational energy is the sum of the species vibrational energies. Monatomic species have no vibrational energy

and are listed last. The first nv species are polyatomic and consequently store energy in vibrational modes. Each of these species has $ndeg(s)$ significant vibrational modes with characteristic temperature $\theta_{v,s,m}$. For each species the energy in all modes is summed with degenerate modes counted multiple times:

$$E_{v,s} = \frac{R}{M_s} \sum_{m=1}^{ndeg(s)} \left[\frac{\theta_{v,s,m}}{\exp\left(\frac{\theta_{v,s,m}}{T}\right)} \right]. \quad (2.3.6)$$

Note that while the vibrational modes are partially excited, they are in equilibrium with the translational and rotational energies. As a result a single temperature characterizes the internal energy of the gas particles, and a separate partial differential equation for the vibrational energy is not required. The temperature must be found iteratively from the definition of the energy; Equation (2.3.2) can not be manipulated to a closed form for T because of the vibrational energy terms. Finally, curve fits for thermodynamic properties are not required with this formulation of the total energy; the θ_v 's specify the variance of the heat capacities with temperature.

The third term of Equation (2.3.2) establishes a reference level of energy. When a species is produced or consumed by chemical reaction, the energy released or absorbed is accounted for by the enthalpy of formation, h_s^o . Kinetic energy due to the macroscopic motion of the gas is included in the fourth term. The enthalpies of formation are found in the literature and are listed for each species in Appendix B, as are the molecular weights and characteristic vibrational temperatures.¹

II.4 Constitutive Relations

Constitutive relations give expressions for the diffusion velocities, the stress tensor, and the heat flux vector. The diffusion of mass, momentum, and energy are dependent on first order gradients of, respectively, concentration, velocity, and temperature.

In this work mass diffusion results from flowfield concentration gradients. Pressure

1. Data is from Stull (1965) and (1971), Dixon-Lewis (1984), and McBride, HeimeI, Ehlers, and Gordon (1963).

and temperature driven mass diffusion are neglected. Additionally it is assumed that diffusion is binary; that is, species s diffuses into a bath of similar particles. The binary diffusion assumption is reasonable when the molecular weights of all species are about the same. With these assumptions, the diffusion velocities are found from Fick's Law,

$$\rho_s v_{s,j} = -\rho D_s \frac{\partial X_s}{\partial x_j}, \quad (2.4.1)$$

where D_s is the binary diffusion coefficient and X_s is the mass fraction of species s ,

$$X_s = \frac{\rho_s}{\rho}. \quad (2.4.2)$$

More accurate methods for the determination of the diffusion velocities are available but are computationally more intensive.²

Shear stresses in the fluid are a consequence of velocity gradients. The gas mixture is treated as a Newtonian fluid, for which

$$\tau_{i,j} = -\mu \left(\frac{\partial u_i}{\partial x_j} + \frac{\partial u_j}{\partial x_i} \right) - \lambda \frac{\partial u_k}{\partial x_k} \delta_{i,j}. \quad (2.4.3)$$

The Stokes hypothesis for the bulk viscosity is used to specify λ :

$$\lambda = -\frac{2}{3}\mu. \quad (2.4.4)$$

The heat flux vector arises from temperature gradients in the flow. Fourier's Law stipulates

$$q_{i,j} = -\kappa \frac{\partial T}{\partial x_j}. \quad (2.4.5)$$

Evaluation of the binary diffusion coefficient, D_s , the coefficient of molecular viscosity, μ , and the heat transfer coefficient, κ , is discussed in the next section.

II.5 Transport Properties

The coefficients D_s , μ , and κ are required for the calculation of the viscous

2. A method involving a series solution for the diffusion velocities is outlined in Oran and Boris (1987), pp. 253-255, and is also described in Wilson (1991).

phenomena described by the constitutive relations. Kinetic theory provides some information, but ultimately experimental measurements are necessary to arrive at values for the coefficients.

Attention is first given to the coefficient of viscosity. The approach taken consists of two parts. A first-order approximation to the coefficient is obtained for each species as a pure gas. Then these species quantities are combined using a mixing rule to get a value of μ for the mixture.

From kinetic theory,

$$[\mu_s]_1 = 2.6693 \times 10^{-6} \frac{\sqrt{M_s T}}{\sigma_s^2 \Omega_{ss}^{(2,2)*}(T^*)}. \quad (2.5.1)$$

The subscript 1 specifies the species viscosity coefficient is a first-order approximation. In this equation, T^* is the reduced temperature, defined by

$$T^* = \frac{k_B T}{\epsilon_s} \quad (2.5.2)$$

where k_B is the Boltzmann constant. The constants σ_s and ϵ_s are Lennard-Jones potential parameters. The symbol $\Omega_{ss}^{(2,2)*}$ is the elastic collision integral;

$$\Omega^{(2,2)*} = A^* \Omega^{(1,1)*}. \quad (2.5.3)$$

For each species, A^* and $\Omega^{(1,1)*}$ are calculated from polynomials in T^* . The Lennard-Jones parameters and curve fit coefficients are taken from Dixon-Lewis³ and are repeated in Appendix B. With the listed values, the units of $[\mu_s]_1$ are *kg/m-sec*.

Wilke's semi-empirical mixing rule⁴ is employed to obtain a mixture viscosity coefficient from the species coefficients. The rule is

$$\mu = \sum_{s=1}^{ns} \left[\frac{Y_s [\mu_s]_1}{\sum_{r=1}^{ns} Y_r \phi_{s,r}} \right], \quad (2.5.4)$$

3. See Dixon-Lewis (1984).

4. See Wilke (1950).

where

$$\phi_{s,r} = \frac{1}{\sqrt{8}} \left(1 + \frac{M_s}{M_r} \right)^{-\frac{1}{2}} \left[1 + \left(\frac{[\mu_s]_1}{[\mu_r]_1} \right)^{\frac{1}{2}} \left(\frac{M_r}{M_s} \right)^{\frac{1}{4}} \right]^2. \quad (2.5.5)$$

The mole fraction of species s is

$$Y_s = \frac{\rho_s}{M_s} \left(\sum_{r=1}^{ns} \frac{\rho_r}{M_r} \right)^{-1}. \quad (2.5.6)$$

The mixture heat transfer coefficient is also found by first determining pure species values and then combining them with the Wilke rule. The species heat transfer is related to the viscosity. It is assumed that the transport of translational energy can be correlated with the velocity, but for internal energy there is no such correlation. This assumption is called the Eucken correlation.⁵ The result is

$$\kappa_s = [\mu_s]_1 \left(\frac{5}{2} c_{v, \text{trans}, s} + c_{v, \text{rot}, s} + c_{v, \text{vib}, s} \right). \quad (2.5.7)$$

Previously $c_{v, \text{trans}, s}$ and $c_{v, \text{rot}, s}$ have been discussed. The vibrational specific heat is just

$$c_{v, \text{vib}, s} = \frac{\partial E_{v, s}}{\partial T} = \frac{R}{M_s} \sum_{m=1}^{ndeg(s)} \frac{\left(\frac{\theta_{v, s, m}}{T} \right)^2 \exp\left(\frac{\theta_{v, s, m}}{T} \right)}{\left[\exp\left(\frac{\theta_{v, s, m}}{T} \right) - 1 \right]^2}. \quad (2.5.8)$$

As with the viscosity, Wilke's rule is used to find the mixture heat transfer coefficient:

$$\kappa = \sum_{s=1}^{ns} \left[\frac{Y_s \kappa_s}{\sum_{r=1}^{ns} Y_r \phi_{s,r}} \right]. \quad (2.5.9)$$

The binary diffusion coefficient is estimated by assuming a constant Schmidt number of 1/2:

$$Sc = \frac{\mu}{\rho D} = \frac{1}{2}, \quad (2.5.10)$$

5. See Vincenti and Kruger (1965), pp. 19-21.

where it is further assumed that all species diffuse at the same rate and have the same D . Because molecular and diatomic hydrogen have molecular weights much lower than the other chemical species in the gas model, they should diffuse more rapidly. Some investigators use higher values for D_H and D_{H_2} to account for the inaccuracy of the binary diffusion assumption, which is the source of the underestimated diffusion for the less massive species. However, this practice sacrifices the conservation of mass and is not implemented here.

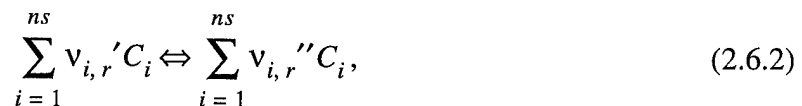
II.6 Chemical Source Terms

The chemical source terms account for the change in mixture composition due to chemical reaction. A nonequilibrium treatment is appropriate because the characteristic chemical time scale is on the same order as the characteristic fluid time scale. An assumed set of chemical reactions is used to model the change in species mass fractions throughout the flow. There are several drawbacks to the model, but these are outweighed by the savings in computational resources.

A general chemical reaction can be described by the stoichiometric equation



In this equation, species i has the chemical symbol C_i . The stoichiometric coefficients for the reactants are denoted by v_i' and for the products by v_i'' . There are a total of n chemical species involved as reactants, products, or collision partners. The general equation above in fact represents two opposing reactions. The forward reaction proceeds from reactants, on the left, to products, on the right. For the backward reaction the reactants and products are reversed, and the reaction proceeds from right to left. The notation can be used for a set of opposing reactions. In that case,



where r refers to the particular reaction. When a set of reactants is considered, n is the number of chemical species in the gas model so $n = ns$. If species j does not participate in

reaction s , then $v_{j,s}' = v_{j,s}'' = 0$.

According to the law of mass action, the reaction rate, RR_r , is given by

$$RR_r = k_{f,r} \prod_{i=1}^{ns} [C_i]^{v_{i,r}'} - k_{b,r} \prod_{i=1}^{ns} [C_i]^{v_{i,r}''}, \quad (2.6.3)$$

where $k_{f,r}$ and $k_{b,r}$ are respectively the forward and backward reaction rate constants for reaction r . The square brackets denote the concentration (*particles/volume*) of the enclosed species. The reaction rate and the chemical source terms are closely related; for species s the net production or consumption of mass, after all nr chemical reactions are considered, is

$$\frac{\dot{w}_s}{M_s} = \frac{d}{dt}[C_s] = \sum_{r=1}^{nr} (v_{s,r}'' - v_{s,r}') RR_r. \quad (2.6.4)$$

The forward rate constant is expressed in the modified Arrhenius form,

$$k_{f,r} = A_r T^{\eta_r} \exp\left(-\frac{\theta_{d,r}}{T}\right). \quad (2.6.5)$$

The characteristic temperature of dissociation, $\theta_{d,r}$, the temperature exponent, η_r , and the pre-exponential factor, A_r , are parameters determined by experimental methods and are found in the literature.

The backward reaction rate constant is determined from the forward rate constant and the equilibrium constant based on concentration, $K_{eq,r}$:

$$K_{eq,r} = \frac{k_{f,r}}{k_{b,r}}. \quad (2.6.6)$$

The equilibrium constant is calculated using the Gibbs' free energies of each species that participates in the reaction. From chemical thermodynamics,

$$K_{eq,r} = (RT)^{-\Delta n_r} \exp\left(-\frac{\Delta G_r^o}{RT}\right), \quad (2.6.7)$$

where

$$\Delta n_r = \sum_{i=1}^{ns} v_{i,r}'' - \sum_{i=1}^{ns} v_{i,r}' \quad (2.6.8)$$

and

$$\Delta G_r^o = \sum_{i=1}^{ns} \nu_{i,r}'' g_i^o - \sum_{i=1}^{ns} \nu_{i,r}' g_i^o. \quad (2.6.9)$$

The molar standard Gibbs' free energy of formation for a species, g_i^o , is calculated from a polynomial in T . The curve fit coefficients are determined experimentally⁶ and are listed in Appendix B.

The assumed set of chemical reactions is called a chemical kinetics mechanism. In practice, a particular mechanism is valid for a given range of conditions or flow situations. Species and reactions are included or omitted based on their significance in the mechanism's intended application. The significance of a particular reaction or species is not always clear.

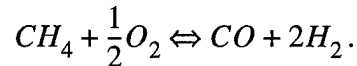
In addition to the reactions, a mechanism specifies the parameters for determining the forward rate constants. The parameters are chosen to match relevant experimental data. Although the modified Arrhenius form for the rate constants can be derived from kinetic theory, the actual determination of A_r , η_r , and $\theta_{d,r}$ is difficult. Because of uncertainties in these rate parameters and the closely related issue of the importance of particular reactions, many different mechanisms have been proposed for hydrocarbon combustion.

For the present studies, methane is used as the fuel and oxygen as the oxidizer. Nitrogen is also included in the mixture as a diluent. Much work has been done to determine the behavior of hydrocarbon fuels in internal combustion and gas turbine engines. Unfortunately the resulting kinetics mechanisms are complex, including as many as 50+ species and hundreds of reactions. Since the required computational time and memory scale roughly as the square of the number of species, complex mechanisms can not be used except for very simple flows. Furthermore, most combustion mechanisms have been developed for modeling subsonic flames at or near atmospheric pressures. Ram-accelerator flowfields are supersonic or hypersonic, and pressures range to hundreds or even thousands of atmospheres.

A quasi-global model is used in the current research. In the quasi-global methane

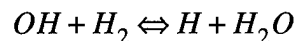
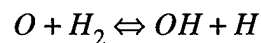
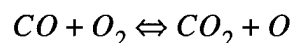
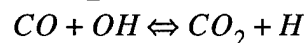
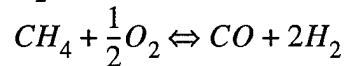
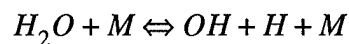
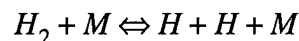
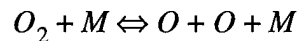
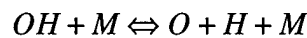
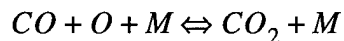
6. The Gibbs' free energy data is listed in McBride, HeimeI, Ehlers, and Gordon (1963).

reaction mechanism of Westbrook and Dryer,⁷ methane and oxygen form carbon monoxide and hydrogen in a global reaction:



A set of elementary reactions models the oxidation of CO and H_2 . The global reaction represents a number of elementary reactions in a single step. It is fundamentally different from the elementary reactions it approximates because, in reality, CH_4 and O_2 do not form carbon monoxide and hydrogen directly. In an elementary reaction, the reactants are converted to products without intermediate steps.

The quasi-global mechanism involves the reacting species CH_4 , CO , CO_2 , O_2 , H_2O , H_2 , OH , O , and H . Nitrogen, N_2 , is also included as a diluent in the gas model. The mechanism includes 12 reactions, including the global reaction. The reactions are



M is a collision partner; it can be any species. The rate parameters are listed in Appendix B. The sixth reaction is the global reaction. The original reference also includes the radicals HO_2 and H_2O_2 . These species are important for modelling ignition at lower temperatures. Ignition in ram-accelerators occurs at higher temperatures; additionally, the use of the quasi-global model nullifies their effects on ignition in this mechanism, as explained

7. See Westbrook and Dryer (1981).

below. Therefore, HO_2 and H_2O_2 and the reactions they participate in are neglected in this thesis.⁸

The global reaction has a phenomenological forward reaction rate, given by

$$RR_{6,f} = A_6 \exp\left(-\frac{\theta_{d,6}}{T}\right) [CH_4]^a [O_2]^b. \quad (2.6.10)$$

The form of the rate is the same as the modified Arrhenius expression, except the concentration exponents a and b are *not* the stoichiometric coefficients; they are parameters chosen to match experimental data. In this case $a = -0.3$ and $b = 1.3$. Since the fuel exponent is negative, the forward reaction rate approaches infinity as the fuel concentration approaches zero. This can cause problems for numerical schemes.⁹ To alleviate the difficulty Westbrook and Dryer suggested¹⁰ the opposing reaction be included with the rate

$$RR_{6,b} = \frac{A_6}{1000} \exp\left(-\frac{\theta_{d,6}}{T}\right) [CH_4]^{a'} [O_2]^{b'}. \quad (2.6.11)$$

In the backward reaction, $a' = -0.5$ and $b' = 1.3$. For the global reaction the reaction rate is thus

$$RR_6 = RR_{6,f} - RR_{6,b}, \quad (2.6.12)$$

and the methane concentration is bounded.

Because several elementary reactions are approximated with a single global reaction, the quasi-global mechanism is not as accurate as a detailed mechanism. In the Westbrook and Dryer model, the global reaction replaces elementary reactions associated with chain initiation and hydrocarbon radicals, and as a consequence the details of the reaction front are lost. In particular, the temperature and species mass fractions through the reaction front will not be correctly predicted. On the other hand, the burned-gas composition and temperature should be accurately resolved because the oxidation of carbon monoxide and hydrogen are modelled by elementary reactions. Additionally, the range of applicability of

8. Soetrisno and Imlay (1992) used the quasi-global model for ram-accelerator studies. They omitted the HO_2 and H_2O_2 species and the associated reactions without adverse effects.

9. See Westbrook and Dryer (1981).

10. The opposing reaction and rate listed here are proposed in Coffee (1985).

the mechanism is further reduced by representing several elementary reactions with a single global reaction. The authors¹¹ point out the pre-exponential factor should be taken as an initial estimate. Established data at conditions near those to be simulated should be used to calibrate A_G . The details of such a calibration are discussed in Chapter IV.

It has also been reported that the quasi-global is sensitive to the modeling of the viscous terms.¹² The flame speed depends to some degree on the diffusion of mass, momentum, and energy, so the initial calibration of the global reaction rate relies on the treatment of the viscous terms in the original reference. Since the fuel and oxidizer are premixed in the ram-accelerator and since the pre-exponential coefficient will be recalibrated anyway, the sensitivity to the viscous modeling is less critical in the present work.

The advantage of the quasi-global mechanism is that it includes only 9 reacting species and 12 reactions. Computationally it is much less expensive than a full, detailed mechanism. The disadvantages of the quasi-global model have been noted; it is an approximation to the behavior a detailed mechanism predicts at 'design' conditions. However, at ram-accelerator conditions, the available detailed mechanisms are no less suspect but much more expensive than the quasi-global model. For this reason the quasi-global mechanism is employed in this thesis.

II.7 Boundary Conditions

In the laboratory, the ram-accelerator projectile travels through the pressurized accelerator tube. The tube has a constant-diameter and cross-section and is filled with a homogeneous mixture of fuel, oxidizer, and diluent. Before the arrival of the projectile the gas is quiescent. Different sections of the tube are divided by diaphragms and can be independently pressurized and fueled. To obtain the desired performance, the pressure and mixture composition are varied in the different tube sections. The acceleration of the projectile and the flowfield it induces are clearly transient in the laboratory frame of reference.

The simulation considers the steady-state flowfield only; it is assumed that the transient, real-world flowfield is accurately approximated by a series of steady-state,

11. See Westbrook and Dryer (1981).

12. See Coffee (1985).

numerical solutions. In the simulation, the projectile is still and the gas flows past it. Ahead of the projectile, the gas velocity is constant and equal to the projectile speed being simulated. At the projectile surface, the continuum assumption stipulates the gas velocity is zero with respect to the projectile. Similarly the no-slip condition applies at the accelerator tube wall. In the simulation, the wall moves at the same speed as the free-stream gas because in the laboratory the projectile moves from one end of the tube to the other.

As the projectile accelerates, it is heated by skin friction and the high temperatures of the burned gas. The dynamics of the temperature field within the projectile are not considered in this study, and until reasonable estimates of the wall and projectile surface temperatures are available, adiabatic flowfield boundaries are assumed.¹³ For simplicity a non-catalytic assumption is employed for the tube and projectile surfaces.

With the above boundary conditions, which specify composition, velocity, and temperature at the projectile and accelerator tube surfaces, the governing equations can be solved over the interior of the computational domain.

13. Nusca (1993) points out that the wall temperature specification significantly affects the flow-field, but that until experimental measurements are available an adiabatic wall condition is appropriate.

CHAPTER III

NUMERICAL METHOD

III.1 Introduction

The equations introduced in Chapter II are solved numerically. The partial differential equations are rewritten as algebraic difference equations, for which many solution techniques have been established. Spatial terms are upwinded or centrally differenced. An implicit, iterative method is used to advance the flowfield from an initial condition to the steady-state solution. Evolution of the flow properties is driven by the conditions at the boundaries of the computational domain.

III.2 Vector Form of the Governing Equations

The governing equations are written in vector form. Some changes are made in the notation. Specifically, the indices specifying coordinate directions are no longer used. With the modifications, the equations describe two-dimensional or axisymmetric flow. The partial differential equation set is expressed as

$$\frac{\partial U}{\partial t} + \frac{\partial F}{\partial x} + \frac{1}{y^r} \frac{\partial}{\partial y} (y^r G) = W. \quad (3.2.1)$$

For two-dimensional Cartesian coordinates, $r = 0$.

If $r = 1$, the equations describe axisymmetric flow in cylindrical coordinates. Then the geometry, and consequently the flow, is symmetric about some centerline. The y -coordinate is the radial distance from this centerline. The source vector, W , contains some new terms that arise from the coordinate system. Other modifications due to the choice of the coordinates will be discussed when necessary.

The conserved variables comprise the vector U :

$$U = (\tilde{\rho}_1, \dots, \tilde{\rho}_{ne}, \rho_{ne+1}, \dots, \rho_{ns}, \rho u, \rho v, \rho E)^T. \quad (3.2.2)$$

The mass-averaged velocities in the x - and y -directions are u and v . The conserved variables are the same in both coordinate systems.

The flux vectors, F and G , are separated into inviscid and viscous components:

$$F = F_I + F_V = \begin{bmatrix} \tilde{\rho}_1 u \\ \vdots \\ \tilde{\rho}_{ne} u \\ \rho_{ne+1} u \\ \vdots \\ \rho_{ns} u \\ \rho u^2 + p \\ \rho uv \\ (\rho E + p) u \end{bmatrix} + \begin{bmatrix} \tilde{\rho}_1 \tilde{u}_1 \\ \vdots \\ \tilde{\rho}_{ne} \tilde{u}_{ne} \\ \rho_{ne+1} u_{ne+1} \\ \vdots \\ \rho_{ns} u_{ns} \\ \tau_{xx} \\ \tau_{xy} \\ u\tau_{xx} + v\tau_{xy} + q_{tx} + \sum_{ns} \rho_s h_s u_s \end{bmatrix}. \quad (3.2.3)$$

The elemental diffusion velocities in the x -direction have symbol \tilde{u}_e , while the species diffusion velocities are given by u_s . Similarly, for the y -direction, elemental and species diffusion velocities are denoted \tilde{v}_e and v_s , and the flux vector is

$$G = G_I + G_V = \begin{bmatrix} \tilde{\rho}_1 v \\ \vdots \\ \tilde{\rho}_{ne} v \\ \rho_{ne+1} v \\ \vdots \\ \rho_{ns} v \\ \rho uv \\ \rho v^2 + p \\ (\rho E + p) v \end{bmatrix} + \begin{bmatrix} \tilde{\rho}_1 \tilde{v}_1 \\ \vdots \\ \tilde{\rho}_{ne} \tilde{v}_{ne} \\ \rho_{ne+1} v_{ne+1} \\ \vdots \\ \rho_{ns} v_{ns} \\ \tau_{xy} \\ \tau_{yy} \\ u\tau_{xy} + v\tau_{yy} + q_{ty} + \sum_{ns} \rho_s h_s v_s \end{bmatrix}. \quad (3.2.4)$$

The source vector contains terms that account for mass transfer between species due to chemical reactions and a term that arises from the axisymmetric coordinate system:

$$W = (0, \dots, 0, \dot{w}_{ne+1}, \dots, \dot{w}_{ns}, 0, r(p - \tau_{\theta\theta})/y, 0)^T. \quad (3.2.5)$$

The first ne entries are zero since the elemental mass densities are unchanged by reactions. The source term in the y -momentum equation results from the axisymmetric coordinates.

III.3 Finite Volume Discretization

The partial differential vector equation (3.2.1) can be discretized, resulting in a large system of algebraic difference equations. A finite-volume formulation over the computational mesh is used. Inviscid, viscous, and implicit terms arise in the discretization and are handled differently. The discussion opens with the definition of the computational domain.

The strategy taken by the numerical method is to represent the physical domain by a limited number of points. At those points, which make up the computational domain, the governing equations are solved. The flowfield properties anywhere in the physical domain can then be determined by interpolation from the points in the computational domain. The underlying assumption in this approach is that the physical domain can be accurately represented by this collection of discrete points. If enough points are included, the assumption is valid.

To represent complicated geometries, general curvilinear grids are preferred over rectangular-celled meshes. The equations are transformed from the physical space (x, y) to the computational space (ξ, η) . The calculation concerns the values of the properties at the discrete points that have integer values of ξ and η . These integer values are given by the indices i and j , respectively. A generic grid cell is shown in Figure 3.1. In the finite-volume formulation, the coordinates $x_{i,j}$ and $y_{i,j}$ refer to the physical location of the lower left corner of the computational cell. However, for all the properties, such as $p_{i,j}$, $\tilde{p}_{e,i,j}$, $u_{i,j}$, and so forth, the indices i and j refer to values at the cell center.

For each cell, Equation (3.2.1) is integrated to give

$$\int_{\Omega} \frac{\partial U}{\partial t} d\Omega + \int_{\Omega} \frac{1}{y^r} \left(\frac{\partial}{\partial x} \langle y^r F \rangle + \frac{\partial}{\partial y} \langle y^r G \rangle \right) d\Omega = \int_{\Omega} W d\Omega, \quad (3.3.1)$$

where Ω is the volume of the cell. On a general curvilinear grid, the cells are not aligned with the coordinate axes. For this reason the radius included for the axisymmetric coordinates is applicable to both the F and G fluxes.

The divergence theorem is invoked for the flux terms:

$$\int_{\Omega} \frac{1}{y^r} \left(\frac{\partial}{\partial x} \langle y^r F \rangle + \frac{\partial}{\partial y} \langle y^r G \rangle \right) d\Omega = \frac{1}{y^r} \int_S \left(y^r F \hat{i} + y^r G \hat{j} \right) \cdot d\vec{S}. \quad (3.3.2)$$

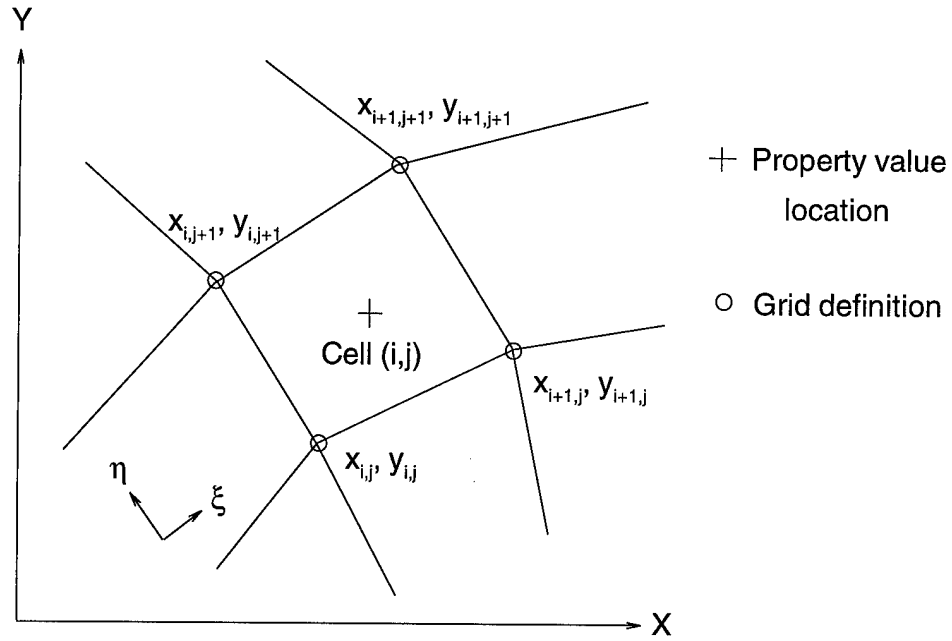


Figure 3.1 Property value and grid definition locations for a representative cell.

The volume integral is recast as a surface integral, where the surface, S , encloses the volume Ω , and \hat{i} and \hat{j} are, respectively, unit normal vectors in the x - and y -directions. In the current research the grid is fixed throughout the computation, so Equation (3.3.1) can be expressed as

$$\Omega \frac{\partial U}{\partial t} + \frac{1}{y^r} \int_S \left(y^r F \hat{i} + y^r G \hat{j} \right) \cdot d\vec{S} = \Omega W. \quad (3.3.3)$$

The temporal term is forward-differenced, and the surface integral is replaced as a sum; then

$$\Omega \frac{\delta U}{\Delta t} + \frac{1}{y^r} \sum_{\text{Sides}} \left(y^r F \hat{i} + y^r G \hat{j} \right) \cdot \vec{S} = \Omega W, \quad (3.3.4)$$

where $\delta U^n = U^{n+1} - U^n$. The superscript here denotes the iteration of the numerical scheme. The time level of the fluxes and the source vector will be specified below.

At this point consider the summation. For each cell side the appropriate \vec{S} is used. For example, consider the $i + 1/2$ cell side:

$$\bar{S}_{i+1/2} = \left(\{s_{ix}' \hat{i} + s_{iy}' \hat{j}\} S \right)_{i+1/2}, \quad (3.3.5)$$

where s_{ix}' and s_{iy}' are direction cosines and S is the area of the cell side. Similarly for the $j + 1/2$ cell side,

$$\bar{S}_{j+1/2} = \left(\{s_{jx}' \hat{i} + s_{jy}' \hat{j}\} S \right)_{j+1/2}. \quad (3.3.6)$$

The direction cosines and cell side areas are closely related to the mesh metrics and their inverses. The calculation of these quantities is discussed in Appendix C, along with other grid-related variables.

With these definitions, fluxes can be defined in curvilinear coordinates. Denoting the rotated fluxes by F' and G' ,

$$F' = F s_{ix}' + G s_{iy}' \quad (3.3.7)$$

and

$$G' = F s_{jx}' + G s_{jy}'. \quad (3.3.8)$$

The definition of the contravariant velocities depends on the cell face being considered. For $i + 1/2$ cell faces,

$$u' = u s_{ix}' + v s_{iy}' \quad v' = -u s_{iy}' + v s_{ix}', \quad (3.3.9)$$

while for $j + 1/2$ cell faces,

$$u' = u s_{jy}' - v s_{jx}' \quad v' = u s_{jx}' + v s_{jy}'. \quad (3.3.10)$$

Defining contravariant velocities simplifies the notation.

Now the equation to be solved at each point i, j is

$$\delta U_{i,j}^n + \frac{\Delta t}{y_{c,i,j}^r \Omega_{i,j}} \left\{ y_{i+\frac{1}{2}}^r F'_{i+\frac{1}{2}}^{n+1} S_{i+\frac{1}{2}} + y_{j+\frac{1}{2}}^r G'_{j+\frac{1}{2}}^{n+1} S_{j+\frac{1}{2}} - y_{i-\frac{1}{2}}^r F'_{i-\frac{1}{2}}^{n+1} S_{i-\frac{1}{2}} - y_{j-\frac{1}{2}}^r G'_{j-\frac{1}{2}}^{n+1} S_{j-\frac{1}{2}} \right\} = W_{i,j}^{n+1} \Delta t \quad (3.3.11)$$

where the time level $n + 1$ has been specified for F' , G' , and W . The cell centroid radius is denoted by y_c ; it is not evaluated at the same location as the radii multiplying the fluxes F and G . For the quantities with a single subscript, the other index is implied; it is either i

or j , whichever is absent.

Since the conserved variables at iteration $n + 1$ are not yet known, the fluxes at $n + 1$ are estimated based on the solution at iteration n . The fluxes are linearized by

$$F'^{n+1} = F'^n + \left. \frac{\partial F'}{\partial U} \right|_n \delta U^n = F'^n + A^n \delta U^n \quad (3.3.12)$$

and

$$G'^{n+1} = G'^n + \left. \frac{\partial G'}{\partial U} \right|_n \delta U^n = G'^n + B^n \delta U^n. \quad (3.3.13)$$

The matrices A and B are the flux Jacobians. The source vector can be linearized in the same manner:

$$W^{n+1} = W^n + \left. \frac{\partial W}{\partial U} \right|_n \delta U^n = W^n + Z^n \delta U^n, \quad (3.3.14)$$

where Z is the chemical Jacobian.

With the linearizations above, Equation (3.3.11) is written

$$\begin{aligned} \frac{y_{c,i,j}^r \Omega_{i,j}}{\Delta t} \left(I - Z_{i,j}^n \Delta t \right) \delta U_{i,j}^n & \quad (3.3.15) \\ & + \left(y^r S \right)_{i+\frac{1}{2}, i+\frac{1}{2}} A_{i+\frac{1}{2}, j}^n \delta U_{i+\frac{1}{2}, j}^n + \left(y^r S \right)_{j+\frac{1}{2}, j+\frac{1}{2}} B_{i, j+\frac{1}{2}}^n \delta U_{i, j+\frac{1}{2}}^n \\ & - \left(y^r S \right)_{i-\frac{1}{2}, i-\frac{1}{2}} A_{i-\frac{1}{2}, j}^n \delta U_{i-\frac{1}{2}, j}^n - \left(y^r S \right)_{j-\frac{1}{2}, j-\frac{1}{2}} B_{i, j-\frac{1}{2}}^n \delta U_{i, j-\frac{1}{2}}^n = -\Delta U_{i,j}^n \end{aligned}$$

The left-hand side of this equation is referred to as the implicit side. The right-hand side is called the explicit side, and is defined by

$$\begin{aligned} \Delta U_{i,j}^n & = y_{i+\frac{1}{2}}^r F'_{i+\frac{1}{2}, i+\frac{1}{2}}^n S_{i+\frac{1}{2}} + y_{j+\frac{1}{2}}^r G'_{j+\frac{1}{2}, j+\frac{1}{2}}^n S_{j+\frac{1}{2}} & (3.3.16) \\ & - y_{i-\frac{1}{2}}^r F'_{i-\frac{1}{2}, i-\frac{1}{2}}^n S_{i-\frac{1}{2}} - y_{j-\frac{1}{2}}^r G'_{j-\frac{1}{2}, j-\frac{1}{2}}^n S_{j-\frac{1}{2}} \\ & - y_{c,i,j}^r \Omega_{i,j} W_{i,j}^n \end{aligned}$$

The evaluation of the right-hand side is discussed in the next section, while the treatment

of the implicit side is covered in Section III.5. A technique for solving Equation (3.3.15) is explained in Section III.6.

III.4 Evaluation of the Explicit Terms

First, consider the inviscid fluxes $F''_{I\ i+1/2}$ and $G''_{I\ j+1/2}$. For supersonic and hypersonic flows the inviscid terms are hyperbolic, characterized by discontinuities such as shock waves. Upwind, shock-capturing methods have been developed to accurately resolve such discontinuities. The original upwind methods eliminated spurious, numerical oscillations associated with central-difference schemes but were only first-order accurate. These upwind methods have been extended to global, second-order accuracy by the addition of nonlinear numerical dissipation; a subset of these modern methods contains the Total Variation Diminishing, or TVD, schemes. For the simulations presented in the following chapters, the upwind method of Roe¹ is extended to second-order accuracy by the non-MUSCL upwind TVD scheme of Yee.² These numerical techniques were developed for one-dimensional, perfect-gas flows but have been also applied to a wide variety of multidimensional, real gas flows in thermochemical nonequilibrium with great success. Only cursory descriptions of Roe's scheme and the Yee TVD extension are given here; thorough treatment of the underlying theory is well documented in the references.

Most of the modern upwind schemes are based on the signs of the eigenvalues of the flux Jacobians. The Jacobian A is decomposed to

$$A = P_A \Lambda_A P_A^{-1} \quad (3.4.1)$$

where Λ_A is a diagonal matrix with the eigenvalues of A on the diagonal and P_A is the corresponding matrix of right eigenvectors. In practice it is difficult to obtain these matrices unless a similarity transform is used. In that case,

$$A = M \tilde{A} M^{-1} = M P_{\tilde{A}} \Lambda_{\tilde{A}} P_{\tilde{A}}^{-1} M^{-1} \quad (3.4.2)$$

where

-
1. See Roe (1984).
 2. See Yee (1989).

$$\tilde{A} = P_A^{-1} \Lambda_A P_A^{-1} = \frac{\partial V}{\partial U} \frac{\partial F'}{\partial V} \quad (3.4.3)$$

and

$$M = \frac{\partial U}{\partial V}. \quad (3.4.4)$$

The eigenvalues of \tilde{A} and A are the same. The vector V is composed of the primitive variables:

$$V = (\tilde{\rho}_1, \dots, \tilde{\rho}_{ne}, \rho_{ne+1}, \dots, \rho_{ns}, u, v, p)^T. \quad (3.4.5)$$

The same decomposition is done for the η direction,

$$B = M \tilde{B} M^{-1} = M P_B^{-1} \Lambda_B P_B^{-1} M^{-1} = P_B \Lambda_B P_B^{-1}. \quad (3.4.6)$$

A detailed explanation of the diagonalization process and resulting definition of the above matrices is given in Appendix D.³

Given the above matrices, many different upwind schemes can be implemented. Generally they are differentiated by the choice of the 'average state' at which the Jacobian terms are evaluated. The average state for the $i + 1/2$ cell face, denoted here by the subscript *avg*, is some weighted average of the i and $i + 1$ states. Roe's approximate Riemann solver represents the flux as

$$F'_{I, i+1/2} = \frac{1}{2} (F'_{I, i} + F'_{I, i+1} - P_{A, avg} |\Lambda_{A, avg}| \alpha_{A, avg}) \quad (3.4.7)$$

where

$$\alpha_{A, avg} = P_{A, avg}^{-1} (U_{i+1} - U_i). \quad (3.4.8)$$

In practice the components $\lambda_{A, avg}^{(l)}$ that comprise the eigenvalue matrix are limited to prevent the appearance of aphysical expansion shocks. The superscript (l) refers to the particular components of the vector. The $|\lambda_{A, avg}^{(l)}|$ are replaced by the function $\psi(\lambda_{A, avg}^{(l)})$, where

3. Thorough treatment of the relationships between the conserved, primitive, and characteristic variables for nonreacting flows is given in Hirsch (1990), Chapter 16. Extension to reacting flows is straightforward.

$$\psi(z) = \begin{cases} |z| & |z| \geq \delta_1 \\ \frac{z^2 + \delta_1^2}{2\delta_1} & |z| \leq \delta_1 \end{cases} \quad (3.4.9)$$

and

$$\delta_1 = \delta_2 (|u'| + |v'| + |a(s'_{ix} + s'_{iy})|). \quad (3.4.10)$$

In the original reference,⁴ suggested values for δ_2 are between 0.05 and 0.25. In this work, δ_2 is specified as a function of the pressure gradient:

$$\delta_2 = \max(0.15, 0.5|pg|), \quad (3.4.11)$$

where

$$pg = \frac{p_{i+1,j} - p_{i,j}}{\frac{1}{2}(p_{i+1,j} + p_{i,j})}. \quad (3.4.12)$$

This specification of δ_2 increases numerical damping in the vicinity of shocks.

For Roe's scheme, the average state is chosen such that the numerical flux exactly captures shock and contact discontinuities. The Roe-averaged variables are defined as follows:

$$\tilde{\rho}_{e,avg} = \frac{\tilde{\rho}_{e,i} + \Gamma \tilde{\rho}_{e,i+1}}{1 + \Gamma}, \quad (3.4.13)$$

$$\rho_{s,avg} = \frac{\rho_{s,i} + \Gamma \rho_{s,i+1}}{1 + \Gamma}, \quad (3.4.14)$$

$$u_{avg} = \frac{u_i + \Gamma u_{i+1}}{1 + \Gamma}, \quad (3.4.15)$$

and

$$H_{avg} = \frac{H_i + \Gamma H_{i+1}}{1 + \Gamma}, \quad (3.4.16)$$

where

4. See Yee (1989).

$$\Gamma = \sqrt{\frac{\rho_{i+1}}{\rho_i}}. \quad (3.4.17)$$

The total enthalpy is defined by

$$H = \frac{\rho E + p}{\rho}. \quad (3.4.18)$$

All other variables at the averaged state are determined from the above quantities. In a similar fashion Roe's scheme is applied to the $j + 1/2$ cell face to obtain $G'_{I j+1/2}$.

Only slight modifications are required for the TVD extension to second-order accuracy. The non-MUSCL, upwind, TVD numerical flux of Yee is

$$F'_{I i+1/2} = \frac{1}{2} (F'_{I i} + F'_{I i+1} - P_{A, avg} \Phi_{A, avg}), \quad (3.4.19)$$

where the average state can be determined from any of the first-order upwind schemes. In this work, the Roe average is used. The components of the vector Φ are denoted by $\phi^{(l)}$, and are defined by

$$\phi^{(l)} = \psi \left(\lambda_{A, avg}^{(l)} + \gamma_{A, avg}^{(l)} \right) \alpha_{A, avg}^{(l)} - \sigma \left(\lambda_{A, avg}^{(l)} \right) [g_{i+1}^{(l)} + g_i^{(l)}]. \quad (3.4.20)$$

The function ψ , the eigenvalues $\lambda^{(l)}$, and the $\alpha^{(l)}$ are the same as before. For steady flows, the function σ is defined by

$$\sigma(z) = \frac{1}{2} \psi(z). \quad (3.4.21)$$

The $g_i^{(l)}$ is the limiter. The limiter controls how much numerical dissipation is added to damp spurious oscillations associated with second-order accuracy. For all fields (all l), a *minmod* limiter used in the current work:

$$g_i^{(l)} = \text{minmod} \left(\alpha_{A, i-1/2}^{(l)}, \alpha_{A, i+1/2}^{(l)} \right) \quad (3.4.22)$$

where

$$\text{minmod}(x, y) = \text{sign}(x) \cdot \max(0, \min[|x|, y \cdot \text{sign}(x)]) . \quad (3.4.23)$$

The subscripts on $\alpha^{(l)}$ refer to the average states for the cell faces on the left ($i - 1/2$) and right ($i + 1/2$) sides of cell i . Other limiters were implemented, but no significant differences were seen in the solutions. Finally,

$$\gamma_{A, avg}^{(l)} = \sigma \left(\lambda_{A, avg}^{(l)} \right) \begin{cases} \left(g_{i+1}^{(l)} - g_i^{(l)} \right) / \alpha_{A, avg}^{(l)} & \alpha_{A, avg}^{(l)} \neq 0 \\ 0 & \alpha_{A, avg}^{(l)} = 0 \end{cases} \quad (3.4.24)$$

This completes the discussion of the explicit inviscid terms.

The terms comprising the viscous fluxes are centrally differenced because they are parabolic in nature. The evaluation of $F'_{V i+1/2}$ and $G'_{V j+1/2}$ requires property values and derivatives at the cell face of interest. Cell face property values are found by averaging the quantities at the adjoining cells, i.e. $\rho_{i+1/2} = (\rho_i + \rho_{i+1}) / 2$. Two types of derivatives are required. Property derivatives are calculated in the computational domain. Mesh derivatives relate changes in the computational space to changes in the physical space.

Expressions for $\frac{\partial \phi}{\partial x}$ and $\frac{\partial \phi}{\partial y}$ are needed, where ϕ is any of the properties X_s , u , v , or T . Given these terms $F'_{V i+1/2}$ and $G'_{V j+1/2}$ are calculated from Equations (3.3.7) and (3.3.8). Applying the chain rule,

$$\frac{\partial \phi}{\partial x} = \frac{\partial \xi}{\partial x} \frac{\partial \phi}{\partial \xi} + \frac{\partial \eta}{\partial x} \frac{\partial \phi}{\partial \eta} \quad (3.4.25)$$

and

$$\frac{\partial \phi}{\partial y} = \frac{\partial \xi}{\partial y} \frac{\partial \phi}{\partial \xi} + \frac{\partial \eta}{\partial y} \frac{\partial \phi}{\partial \eta}. \quad (3.4.26)$$

As discussed in Appendix C, the mesh derivatives (or mesh metrics) $\frac{\partial \xi}{\partial x}$, $\frac{\partial \eta}{\partial x}$, $\frac{\partial \xi}{\partial y}$, and $\frac{\partial \eta}{\partial y}$ are more easily calculated in terms of their inverses. Then

$$\frac{\partial \phi}{\partial x} = \frac{1}{J} \left[y_{\eta} \frac{\partial \phi}{\partial \xi} - y_{\xi} \frac{\partial \phi}{\partial \eta} \right] \quad (3.4.27)$$

and

$$\frac{\partial \phi}{\partial y} = \frac{1}{J} \left[-x_{\eta} \frac{\partial \phi}{\partial \xi} + x_{\xi} \frac{\partial \phi}{\partial \eta} \right] \quad (3.4.28)$$

where

$$\frac{1}{J} = \frac{1}{x_{\xi} y_{\eta} - x_{\eta} y_{\xi}}. \quad (3.4.29)$$

Consider the $i + 1/2$ cell face. Property derivatives in the ξ -direction are centrally differenced by

$$\left. \frac{\partial \phi}{\partial \xi} \right|_{i+1/2, j} = \phi_{i+1, j} - \phi_{i, j} \quad (3.4.30)$$

while those in the η -direction are written

$$\left. \frac{\partial \phi}{\partial \eta} \right|_{i+1/2, j} = \frac{1}{2} \left[\frac{\phi_{i+1, j+1} - \phi_{i+1, j-1}}{2} + \frac{\phi_{i, j+1} - \phi_{i, j-1}}{2} \right]. \quad (3.4.31)$$

For the $j + 1/2$ cell face the following formulae are used:

$$\left. \frac{\partial \phi}{\partial \xi} \right|_{i, j+1/2} = \frac{1}{2} \left[\frac{\phi_{i+1, j+1} - \phi_{i-1, j+1}}{2} + \frac{\phi_{i+1, j} - \phi_{i-1, j}}{2} \right] \quad (3.4.32)$$

and

$$\left. \frac{\partial \phi}{\partial \eta} \right|_{i, j+1/2} = \phi_{i, j+1} - \phi_{i, j}. \quad (3.4.33)$$

With the above expressions, the terms comprising the viscous fluxes can be calculated using the relations in Chapter II.

The relations introduced in section II.6 are used to calculate the net production of the retained species and, if applicable, the source terms arising from the axisymmetric coordinate system. The evaluation of the axisymmetric terms is straight-forward. With slight modifications, the chemical source terms are calculated using the relations described in Chapter II.

For some combusting flowfield simulations, it is possible for a fast chemical reaction to completely convert reactants to products within a single mesh cell; that is, a reaction reaches equilibrium in a fraction of the time it takes for the reacting molecules to cross the cell. The energy released, and thus the temperature, is then overpredicted. Since reaction rates increase with temperature, the overprediction is amplified on the next iteration. The overall result is that 'runaway' reactions occur and the reaction front moves at an aphysical speed.⁵ It is pointed out by Eberhardt et. al.⁶ that while the grid cannot resolve such fast reactions, the associated difficulties can be circumvented by limiting the Damköhler

number. This is done by calculating a time scale for each reaction and a fluid time scale, comparing them, and then limiting the reaction rates of the disagreeable reactions.

The Damköhler number is the ratio of the fluid time scale to the time scale of the reaction, defined as

$$Da_r = \frac{\tau_{fluid}}{\tau_{rxn, r}} \quad (3.4.34)$$

where r is the index of the reaction. The fluid time scale for a cell is defined as

$$\tau_{fluid} = \frac{(|u'| + a) S_i + (|v'| + a) S_j}{\Omega} \quad (3.4.35)$$

The reaction time scales have different forms depending on the number of reactant and product species. Time scales for the forward and backward components of a reaction are calculated, and the more limiting of the two is used. For the generic exchange reaction



the two time scales are

$$\tau_{rxn, f} = \sqrt{(k_f C_A)^2 + (k_f C_B)^2} \quad (3.4.36)$$

and

$$\tau_{rxn, b} = \sqrt{(k_b C_C)^2 + (k_b C_D)^2}. \quad (3.4.37)$$

These time scales are estimates of the time required for reactant concentrations to decay to $1/e$ of the initial concentrations.⁷ For the forward reaction A and B are the reactants, but C and D are the reactants in the backward reaction. For other reaction forms, the time scales are slightly modified but are found in the same manner.

Once the above time scales are calculated, the forward and backward reaction rate constants are multiplied by the factor

$$f_r = \min(f_{f, r}, f_{b, r}) \quad (3.4.38)$$

where

5. See Oran and Boris (1987), pp. 523-524.

6. See Eberhardt and Imlay (1989).

7. See Kuo (1986), p. 154.

$$f_{f,r} = \frac{\min(\tau_{rxn,f,r}, Da_{max}\tau_{fluid})}{\tau_{rxn,f,r}} \quad (3.4.39)$$

and

$$f_{b,r} = \frac{\min(\tau_{rxn,b,r}, Da_{max}\tau_{fluid})}{\tau_{rxn,b,r}} \quad (3.4.40)$$

The Damköhler number is limited to Da_{max} , which in this work is 10. For $Da_{max} = 100$, no differences were observed in the solutions but convergence was degraded. Both the forward and backward rate coefficients are multiplied by the same factor, so the equilibrium constant is not affected by the limiting.

III.5 Evaluation of the Implicit Terms

The methods for calculating the explicit fluxes F'^n and G'^n have been described. Solution advancement schemes have been developed that require only these explicit fluxes and are aptly called explicit schemes. The time step for explicit schemes is limited by stability considerations, and for flows with fast chemical reactions the limitation can be severe. Implicit schemes alleviate the strictures on the time step, but the cost per iteration increases. The additional expense is for the calculation, and in particular the inversion, of the Jacobians.

The terms on the explicit side are modelled as accurately as is reasonable, because the final numerical solution satisfies the physics described by the right-hand side. In contrast, the implicit terms, namely A^n , B^n , and Z^n , are usually approximated. Previously the flux Jacobians were decomposed for the implementation of Roe's scheme, but they are evaluated differently for the implicit side. If properly designed and implemented, an implicit scheme will do two things. First, it will converge to the numerical solution dictated by the right-hand side. Second, it will reduce the number of iterations required, with the ultimate goal being the reduction of overall computer time. The approximations made on the left-hand side distinguish the different implicit solution advancement methods. More accurate approximations generally reduce the number of necessary iterations, but the cost per time step increases. The best solution advancement scheme, in terms of overall computer time,

depends on the particular flow problem and machine architecture.

A modified form of the diagonal implicit scheme of Eberhardt and Imlay⁸ is used in this thesis. The diagonal implicit scheme is an extension of the Lower-Upper-Symmetric-Gauss-Seidel (abbreviated LU-SGS) method of Yoon and Jameson⁹ to chemically reacting flows. To apply the LU-SGS scheme the fluxes on the implicit side are upwinded:

$$y_{i+\frac{1}{2}}^r S_{i+\frac{1}{2}} A_{i+\frac{1}{2}}^n \delta U_{i+\frac{1}{2}}^n = y_i^r S_i A_{+,i}^n \delta U_i^n + y_{i+1}^r S_{i+1} A_{-,i+1}^n \delta U_{i+1}^n. \quad (3.5.1)$$

The variables y_i and S_i are averages of the values at the $i + 1/2$ and $i - 1/2$ cell faces. Consequently $y_i = y_{c,i,j}$. The flux Jacobians are discussed in Appendix D. The split flux Jacobians are constructed such that A_+^n contains strictly nonnegative eigenvalues and A_-^n contains strictly nonpositive eigenvalues. Only the inviscid terms are included in the Jacobians. In a similar fashion $B_{j\pm\frac{1}{2}}^n$ is split. As a result Equation (3.3.15) is rewritten

$$\begin{aligned} y_{c,i,j}^r \left[\frac{\Omega_{i,j}}{\Delta t} I + S_i (A_{+,i}^n - A_{-,i}^n) + S_j (B_{+,j}^n - B_{-,j}^n) - \Omega_{i,j} Z_{i,j}^n \right] \delta U_{i,j}^n \\ + y_{c,i+1,j}^r S_{i+1} A_{-,i+1}^n \delta U_{i+1,j}^n - y_{c,i-1,j}^r S_{i-1} A_{+,i-1}^n \delta U_{i-1,j}^n \\ + y_{c,i,j+1}^r S_{j+1} B_{-,j+1}^n \delta U_{i,j+1}^n - y_{c,i,j-1}^r S_{j-1} B_{+,j-1}^n \delta U_{i,j-1}^n = -\Delta U_{i,j}^n \end{aligned} \quad (3.5.2)$$

The LU-SGS scheme represents the split flux Jacobians as follows:

$$A_{\pm}^n = \frac{1}{2} (A^n \pm r_A I) \quad B_{\pm}^n = \frac{1}{2} (B^n \pm r_B I). \quad (3.5.3)$$

The spectral radii of A^n and B^n are r_A and r_B , respectively. With this representation of the split flux Jacobians, note that

$$A_{+,i}^n - A_{-,i}^n = r_{A,i,j} I \quad (3.5.4)$$

and

$$B_{+,j}^n - B_{-,j}^n = r_{B,i,j} I. \quad (3.5.5)$$

Consequently Equation (3.5.2) can be simplified to

8. See Eberhardt and Imlay (1989).

9. See Yoon and Jameson (1987) and (1988).

$$\begin{aligned}
& y_{c,i,j}^r \left[\left(\frac{\Omega_{i,j}}{\Delta t} + r_{A,i,j} S_i + r_{B,i,j} S_j \right) I - \Omega_{i,j} Z_{i,j}^n \right] \delta U_{i,j}^n \\
& + y_{c,i+1,j}^r S_{i+1} A_{-,i+1}^n \delta U_{i+1,j}^n - y_{c,i-1,j}^r S_{i-1} A_{+,i-1}^n \delta U_{i-1,j}^n \\
& + y_{c,i,j+1}^r S_{j+1} B_{-,j+1}^n \delta U_{i,j+1}^n - y_{c,i,j-1}^r S_{j-1} B_{+,j-1}^n \delta U_{i,j-1}^n = -\Delta U_{i,j}^n
\end{aligned} \quad (3.5.6)$$

Observe that for the nonreacting case the chemical Jacobian is zero, and the terms in square brackets form a diagonal matrix. The inversion of a diagonal matrix is much less expensive, computationally, than a full matrix, and for this reason the LU-SGS scheme has a very low cost-per-time-step compared to other implicit methods.

The spectral radii are approximated by the maximum eigenvalues:

$$r_A = |u' + a| \quad r_B = |v' + a|. \quad (3.5.7)$$

Although the viscous terms are not included in the split flux Jacobians, an adjustment is made to the spectral radii for viscous flows. The term

$$\frac{S_i}{\Omega_{i,j}} \left(\frac{\kappa}{\rho \bar{C}_v + \sum_{s=1}^{ns} \rho_s c_{v, \text{vib}, s}} \right)_{i,j} \quad (3.5.8)$$

is added to r_A , where \bar{C}_v is defined in Appendix D. The same term is added to r_B except S_j replaces S_i .

With the inclusion of the full chemical Jacobian, the off-diagonal terms are no longer zero and the full matrix must be inverted. Eberhardt and Imlay approximated $Z_{i,j}^n$ in such a way that the diagonal form is retained. In the diagonal implicit scheme, only the first ns rows and ns columns of the chemical Jacobian are considered. The matrix $Z_{i,j}^n$ is represented by

$$Z_{i,j}^n = \text{diag} \left(\frac{1}{\tau_1}, \dots, \frac{1}{\tau_{ns}}, 0, 0, 0 \right). \quad (3.5.9)$$

Each chemical species has a chemical time scale, τ_s , that is based on the reactions in which the species participates. The time scale is defined by

$$\frac{1}{\tau_s} = \beta_c \left[\sum_{r=1}^{ns} \left(\frac{\partial \dot{w}_s}{\partial \rho_r} \right)^2 \right]^{\frac{1}{2}} \quad (3.5.10)$$

where $\frac{\partial \dot{w}_s}{\partial \rho_r}$ are the components of the first ns rows and columns of the full chemical Jacobian.

Based on its corresponding time scale, each species equation evolves at a different rate. The species equations are underrelaxed relative to the momentum and energy equations. The parameter β_c is an additional underrelaxation factor. For a species that participates in fast chemical reactions, $1/\tau_s$ is large; the corresponding mass conservation equation is underrelaxed to a greater degree than the equations associated with smaller values of $1/\tau_s$. For most other implicit methods, all equations evolve at the same rate. An advantage of the diagonal implicit scheme is that all equations are not slowed to a time step limited by the most restrictive equation; each equation evolves at a rate determined independently of the other equations.

The disadvantages of the scheme are also a result of the differing relaxation rates. As detailed by Candler and Olynick¹⁰ and Hassan et. al.,¹¹ the convergence properties of the diagonal implicit scheme suffer from several inconsistencies caused by the treatment of the chemical Jacobian. There are three disadvantages. First, elemental mass is not conserved when species evolve at different rates. Second, since the total density is found by summing the species densities, it evolves at a rate that is a weighted sum of the species evolution rates. Compared to the momentum and energy equations, the species equations are underrelaxed. The total density therefore lags the momentum and energy. The above authors have mitigated these difficulties by replacing some of the species mass conservation equations by elemental mass conservation equations. The chemical Jacobian of this modified diagonal implicit scheme is represented by

$$Z_{i,j}^n = \text{diag}\left(0, \dots, 0, \frac{1}{\tau_{ne+1}}, \dots, \frac{1}{\tau_{ns}}, 0, 0, 0\right) \quad (3.5.11)$$

where

$$\frac{1}{\tau_s} = \left[\sum_{r=1}^{ne} \left(\frac{\partial \dot{w}_s}{\partial \tilde{\rho}_r} \right)^2 + \sum_{r=ne+1}^{ns} \left(\frac{\partial \dot{w}_s}{\partial \rho_r} \right)^2 \right]^{\frac{1}{2}}. \quad (3.5.12)$$

10. See Candler and Olynick (1991).

11. See Hassan, Candler, and Olynick (1992).

The underrelaxation parameter β_c was found to be unnecessary using the elemental formulation. The elemental equations have $1/\tau_e = 0$ because there are no source terms for the elemental densities. When the total density is determined by summing the elemental densities, it is consistent with the momentum and energy because the elemental mass, momentum, and energy equations are all relaxed at the same rate. Because of these improvements, the elemental conservation equations are employed in this work.

The third disadvantage is that the diagonal implicit scheme, in both the original and modified forms, is suitable for finding steady-state solutions only. Temporal accuracy is forfeited because each species equation effectively has a different time step. For each species equation there is a different transformation between physical time and computational time (iteration number). Thus, there is no way to relate a single physical time to a given iteration number.

While the elemental formulation relieves some of the difficulties of the diagonal implicit scheme, another is created. Specifically, it is possible to calculate negative densities for the replaced species. The replaced species are those omitted from U , the vector of conserved variables; they have been replaced by elemental densities. The species included in the conserved variable vector are referred to as the retained species. The replaced species densities are computed from the elemental and retained species densities using Equation (2.2.21). That equation is valid for a specific location in physical space (x, y) and time (t) . However, it is implemented for each point in computational space (ξ, η) and time (iteration number n). As mentioned previously, at a given iteration the retained species are at different points in physical time because each retained species equation is relaxed at a different rate. Strictly speaking, the linear combination for computing the replaced species does not apply. As an simplistic example of how negative densities arise, suppose the species CO and CO_2 are retained while CH_4 is replaced. Further assume that CO has a small chemical time scale τ_{CO} compared to that of CO_2 . If CO is being oxidized to CO_2 , the production of CO_2 can be far greater than the depletion of CO because the latter has a smaller time scale. When elemental conservation is enforced (for carbon, in this example), the C in CO_2 must come from the replaced species CH_4 . A negative density is computed when more C is taken from CH_4 than actually exists even if

that is not physically possible.

To this point the equations have been developed without specifying which of the species are retained and which are replaced. The development of the flowfield from the initial conditions to the final numerical solution depends on the choice of retained species, because only the $ne + 1$ to ns time scales are used. For some selections negative densities may arise, while for others all replaced densities will be positive. Based on careful numerical experiments, the replaced species are CH_4 , O_2 , H_2 , and N_2 in this thesis. No significant negative densities were observed in the flowfields presented.

The occurrence of negative densities was not reported by Candler and Olynick or by Hassan et. al., who used the elemental formulation for reentry flowfields. The gas model in those studies was 8- or 11-species air, both of which consider only the elements nitrogen and oxygen. It is possible that negative densities are more likely to occur for gas models with more elements. It is also possible that they arise because of the global reaction, which has a nonstandard rate form. However, the example above suggests chemical models with only Arrhenius rates are no less susceptible.

The diagonal implicit scheme is not time-accurate, and it could be argued that therefore only the steady state solution has any physical meaning. The occurrence of negative densities during the transient should not cause alarm because the intermediate solutions have no significance. However, the use of these negative densities in many of the relations described in Chapter II can lead to inconsistencies that ultimately prevent the development of the correct numerical solution. During testing of the algorithm, some choices for replaced species resulted in negative, monotonically decreasing CO_2 mass fractions. Obviously the final solution was aphysical. For this reason, thorough testing and validation of computer programs employing the diagonal implicit scheme is highly recommended. Clearly further investigation into the conditions which lead to negative replaced species densities is warranted.

III.6 Solution Advancement

When the entire computational domain is considered, Equation (3.5.6) is a large, block-pentadiagonal system. At the beginning of an iteration, an approximate solution for

the entire flowfield is known. The solution is improved during the iteration, and after a number of iterations it is a close approximation to the physical solution described by the governing equations.

An iteration consists of several steps. First the explicit terms are evaluated, as discussed in Section III.4, and ΔU^n is calculated for the interior mesh cells. The interior cells are all those within the boundary of the physical domain. For a grid of size il by jl , where il is the number of points in the ξ -direction and jl is the number in the η -direction, the interior cells have $i = 2, \dots, il - 1$ and $j = 2, \dots, jl - 1$.

Second, Equation (3.5.6) is approximately solved by two Gauss-Seidel sweeps. On the forward sweep, from the lower left corner to the upper right corner of the mesh,

$$\delta U_{i,j}^{n*} = D_{i,j}^{-1} \left(y_{c,i-1,j}^r S_{i-1} A_{+,i-1}^n \delta U_{i-1,j}^{n*} + y_{c,i,j-1}^r S_{j-1} B_{+,j-1}^n \delta U_{i,j-1}^{n*} - \Delta U_{i,j}^n \right) \quad (3.6.1)$$

On the backward sweep,

$$\delta U_{i,j}^n = \delta U_{i,j}^{n*} - D_{i,j}^{-1} \left(y_{c,i+1,j}^r S_{i+1} A_{-,i+1}^n \delta U_{i+1,j}^n + y_{c,i,j+1}^r S_{j+1} B_{-,j+1}^n \delta U_{i,j+1}^n \right). \quad (3.6.2)$$

For both sweeps, the diagonal matrix is

$$D_{i,j} = y_{c,i,j}^r \left[\left(\frac{\Omega_{i,j}}{\Delta t} + r_{A,i,j} S_i + r_{B,i,j} S_j \right) I - \Omega_{i,j} Z_{i,j}^n \right]; \quad (3.6.3)$$

it is this diagonal matrix that is easily inverted, resulting in a low cost per iteration.

At the end of the backward sweep δU^n is known for the interior cells. The third step is the update step:

$$U^{n+1} = U^n + \delta U^n. \quad (3.6.4)$$

Any other necessary flowfield properties are determined from the updated conserved variables. The boundary cells are updated as the fourth step, which is discussed in the next section.

III.7 Boundary Conditions

The cell face shared by a boundary cell and the first interior cell is the physical boundary. It may be a solid surface, or it may be a line in space defining the edge of the flowfield

to be simulated. The boundary cells provide a means of imposing boundary conditions at the physical boundaries and are defined such that the physical boundary is halfway between the cell centroids of the boundary cell and first interior cell. Additionally the boundary and first interior cells have the same volumes.

At an inflow boundary, the conditions are specified by the freestream conditions. At an outflow boundary zeroth-order extrapolation is applied:

$$\Phi_{il,j} = \Phi_{il-1,j}, \quad (3.7.1)$$

where the boundary cell has indices il, j , and ϕ is any property. Although this extrapolation is strictly valid for supersonic outflow only, it is also applied where boundary layers cross the outflow boundary.

For inviscid simulations, the flow tangency condition specifies the boundary cell properties at solid surfaces. The same conditions are applied at centerline boundaries. Consider a boundary cell with indices $1, j$. The u' velocity is parallel to the boundary, while v' is perpendicular to it. The velocities at the interface should be

$$u'_{\frac{3}{2},j} = \frac{u'_{1,j} + u'_{2,j}}{2} \equiv u'_{2,j} \quad v'_{\frac{3}{2},j} = \frac{v'_{1,j} + v'_{2,j}}{2} = 0. \quad (3.7.2)$$

Solving for the boundary cell velocities,

$$u'_{1,j} = u'_{2,j} \quad (3.7.3)$$

and

$$v'_{1,j} = -v'_{2,j}. \quad (3.7.4)$$

From the definition of contravariant velocities, $u_{1,j}$ and $v_{1,j}$ can be determined. It is assumed that the grid is orthogonal near the boundary, and the remaining properties are reflected:

$$\Phi_{1,j} = \Phi_{2,j}, \quad (3.7.5)$$

where ϕ is any of the elemental or species densities, the temperature, or the pressure. The remaining variables are calculated from these.

For viscous simulations, the no-slip condition is appropriate at solid boundaries. In that case

$$u'_{\frac{3}{2},j} = \frac{u'_{1,j} + u'_{2,j}}{2} = u_{wall} \quad v'_{\frac{3}{2},j} = \frac{v'_{1,j} + v'_{2,j}}{2} = v_{wall} \quad (3.7.6)$$

so

$$u'_{1,j} = 2u'_{wall} - u'_{2,j} \quad (3.7.7)$$

and

$$v'_{1,j} = 2v'_{wall} - v'_{2,j}. \quad (3.7.8)$$

For most cases the walls do not move in relation to the frame of reference of the simulation, and u_{wall} and v_{wall} are both zero. However, the accelerator tube wall moves with respect to the projectile surface, so for viscous ram-accelerator simulations $u'_{wall} = u_{\infty}$ and $v'_{wall} = 0$. The remaining variables are reflected, as in the inviscid surface case. For such a specification an adiabatic boundary is assumed since $T_{1,j} = T_{2,j}$.

CHAPTER IV

BLUNT BODY SIMULATIONS

IV.1 Introduction

The purpose of the blunt body simulations is to validate the numerical method. The simulations concern the hypersonic, inviscid, reacting flow over cylinders of various diameters. Blunt body flowfields contain a bow shock that is normal near the stagnation line but weakens away from it. A moderate expansion is also present as flow accelerates around the body. Accurately capturing these features requires a robust flow solver.

For combusting flows, the bow shock prompts ignition because of the high temperatures in the shock layer. Ignition generally refers to the beginning of rapid energy release. Depending on the conditions, a steady energy-release front can form between the bow shock and the body. The energy-release front is also called the reaction front because it is where the fuel is consumed and converted to combustion products. The region between this front and the shockwave is called the induction zone; after reaching a temperature high enough to initiate ignition, there is a time delay before the energy is released, called the induction time. The length of the induction zone is essentially the distance covered by the reacting particles during the induction time.

Accurate modelling of the induction zone requires a sound chemical kinetics mechanism. The induction time is highly dependent on the temperature, pressure, and composition of the gas. Thus, the shock and reaction front standoff distances are sensitive to the chemistry model implemented, and for this reason are used as the basis of comparison to established solutions. The results exhibit the advantages and drawbacks of the quasi-global mechanism and demonstrate the ability of the numerical scheme to simulate hypersonic, combusting flowfields.

IV.2 Flow Conditions

The blunt body flowfields presented model the flow over rods of 1, 3, and 7 mm diameter. The gas mixture is stoichiometric methane-air at freestream temperature

$T_\infty = 295\text{ K}$, pressure $p_\infty = 51000\text{ Pa}$, and velocity $u_\infty = 2330\text{ m/s}$. The resulting Mach number is 6.61. The induction time depends only on the conditions of the gas behind the shockwave. However, since the bow shock and energy-release front standoff distances are coupled, the flowfields induced by each rod size are not the same when non-dimensionalized by diameter.

The computational grid has the same proportions for the different rod sizes; it is linearly scaled to the appropriate diameter. To reduce the expense of the simulations, only one half of the rod is considered. The full flowfield can be generated by reflection across the centerline. Since the data of interest is contained in the flow ahead of the body, the wake region is not included in the simulation. The mesh is shown in Figure 4.1. The grid consists of 95 points radially and 91 points around the body. The boundary conditions are freestream conditions along the left (curved) boundary, centerline conditions along the

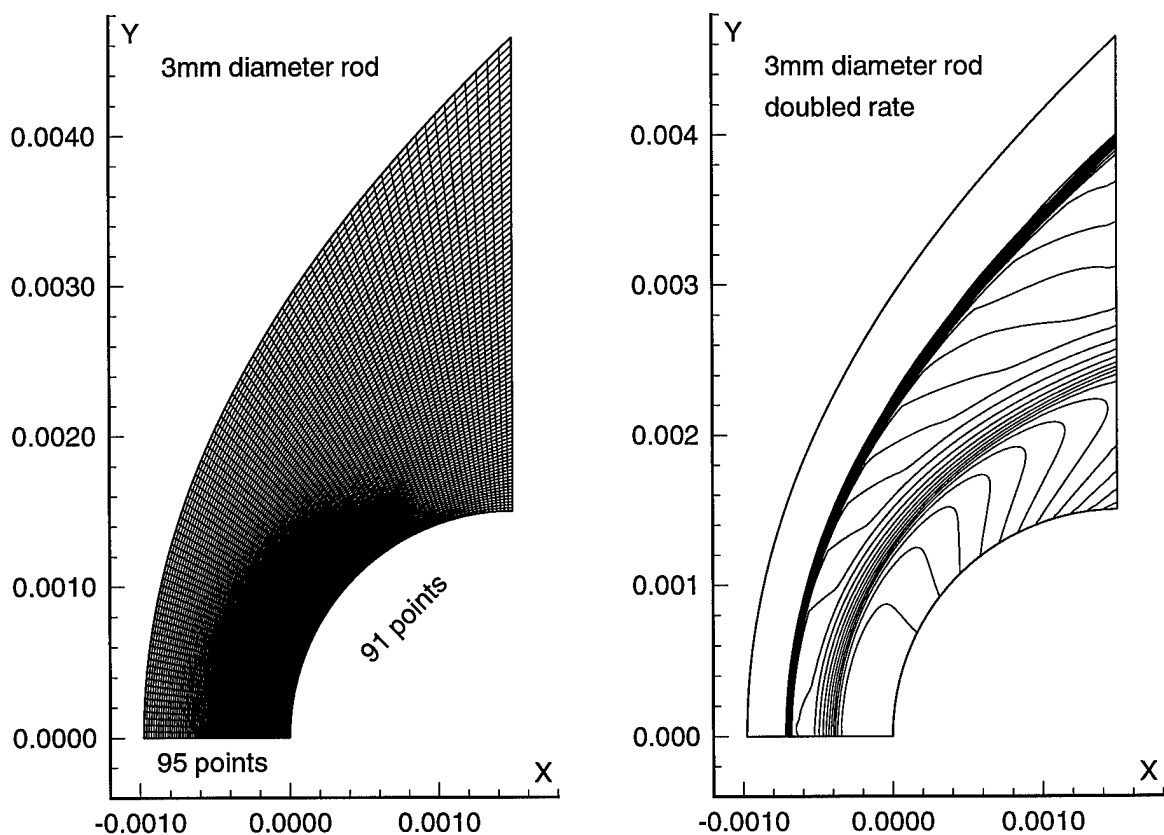


Figure 4.1 Blunt body mesh and representative temperature contours.

bottom boundary, inviscid wall along the body surface, and outflow conditions at the right edge of the domain. Additionally a temperature contour plot is shown in Figure 4.1. The temperature contours illustrate the relevant flowfield features. The shockwave and energy-release front are unambiguous.

The cases were originally investigated by Yungster and Rabinowitz.¹ Those authors used a 20 species, 52 reaction chemical kinetics mechanism, which was carefully derived from a 33 species, 149 reaction model² based on a comparisons with experimentally measured ignition delay times in shock tubes. Because of its systematic development, the Yungster and Rabinowitz solutions are the benchmark for the validations in the present research. The data for comparison are pressure and temperature profiles on the centerline. Pressure profiles clearly illustrate the shock standoff distance, while the temperature profiles additionally show the energy-release front.

IV.3 Discussion of the Simulations

Flowfield simulations were obtained for the conditions described above. Two sets of runs were made. In the first set, the value of the pre-exponential coefficient A_6 is that suggested in the original reference.³ In the second set, double the original value is used. Recall that the subscript 6 refers to the sixth reaction, which is the global reaction. As discussed in section II.6, the pre-exponential coefficient should be calibrated to match established data.

Each reacting simulation ran between 4000 and 6000 iterations. The nonreacting run took 2000 iterations. For all cases the residual dropped at least 4 orders of magnitude. In some instances an interaction between the Damkohler limiting and the global reaction rate inhibited further reduction of the residual. However, flowfield properties remained unchanged after ~ 2500 iterations.

For the results obtained using the original rate, the nondimensionalized pressure profiles along the centerline are shown in Figure 4.2. The pressure is nondimensionalized by

-
1. See Yungster and Rabinowitz (1993).
 2. See Frenklach, Wang, and Rabinowitz (1992)
 3. See Westbrook and Dryer (1981).

p_∞ and the x -axis is nondimensionalized by the radius of the rod. The established data of Yungster is represented by dashed lines, while for the present results they are solid. The pressure profile for the nonreacting case is also shown for comparison and is denoted by the solid line with square symbols. Flow is from left to right. For all cases the bow shock is indicated by the steep pressure rise. It is clear from the plot that the shock standoff distance is underpredicted using the original rate coefficient A_6 .

The nondimensional temperature profiles are shown in Figure 4.3 with the same line and symbol conventions. The first increase in temperature denotes the shockwave. The second increase signifies the energy-release front. The benchmark profiles show the reaction front further from the body than the current results. On the basis of these comparisons, the conclusion is that the original value of the pre-exponential coefficient is too low. If the induction time was smaller, the standoff distance of the energy-release front would be further from the body. As a second consequence, the shock standoff distance would also be greater.

A second set of runs was generated with double the original value for A_6 . The corresponding pressure and temperature profiles are shown in Figures 4.4 and 4.5, respectively. Clearly the pressure and temperature profiles are in better agreement with the doubled rate. The induction zone is roughly the same length for the present results and the simulations of Yungster and Rabinowitz, indicating the different kinetics models are in agreement.

Although the shock and energy-release front standoff distances and the induction zone length are improved using the doubled rate, there are still slight incongruities in the results. While the profiles are similar, their shapes are not the same. Compared to the baseline data, the energy-release front is smeared. The temperature behind the energy-release front is higher. The shock standoff distance matches very well for the 1 mm rod, but discrepancies can be seen for the larger diameters. The results underscore the shortcomings of the quasi-global mechanism; by modelling many detailed reactions with a single phenomenological reaction, the details of the reaction front are sacrificed.

On the other hand, the advantage of the quasi-global model is that reasonable estimates of the induction zone, standoff distances, and gas composition and temperature are

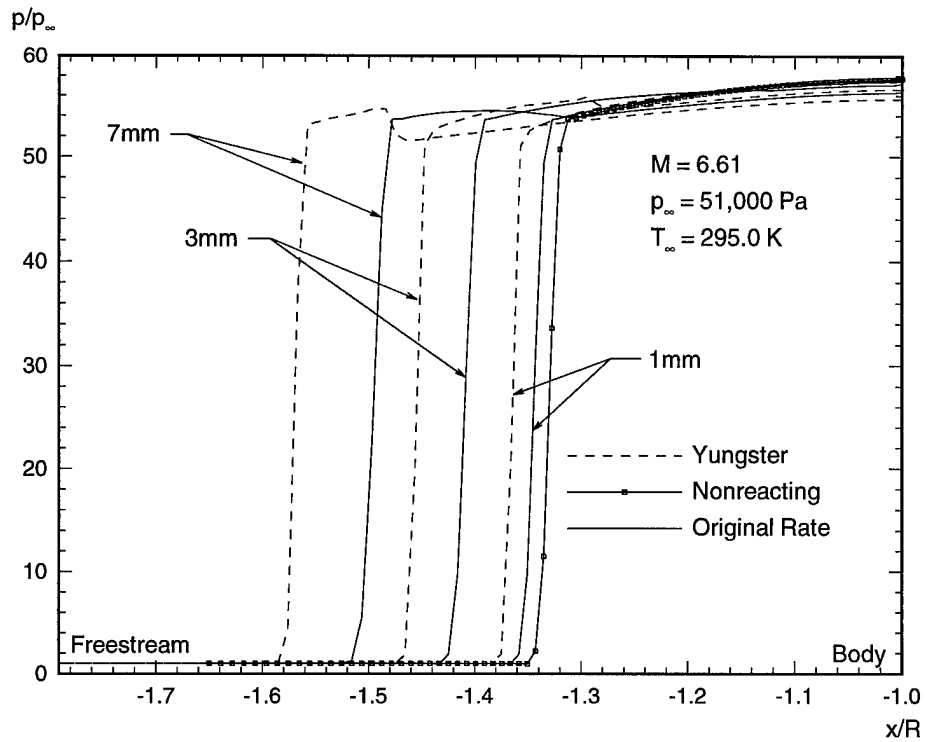


Figure 4.2 Pressure profile comparison using the original rate.

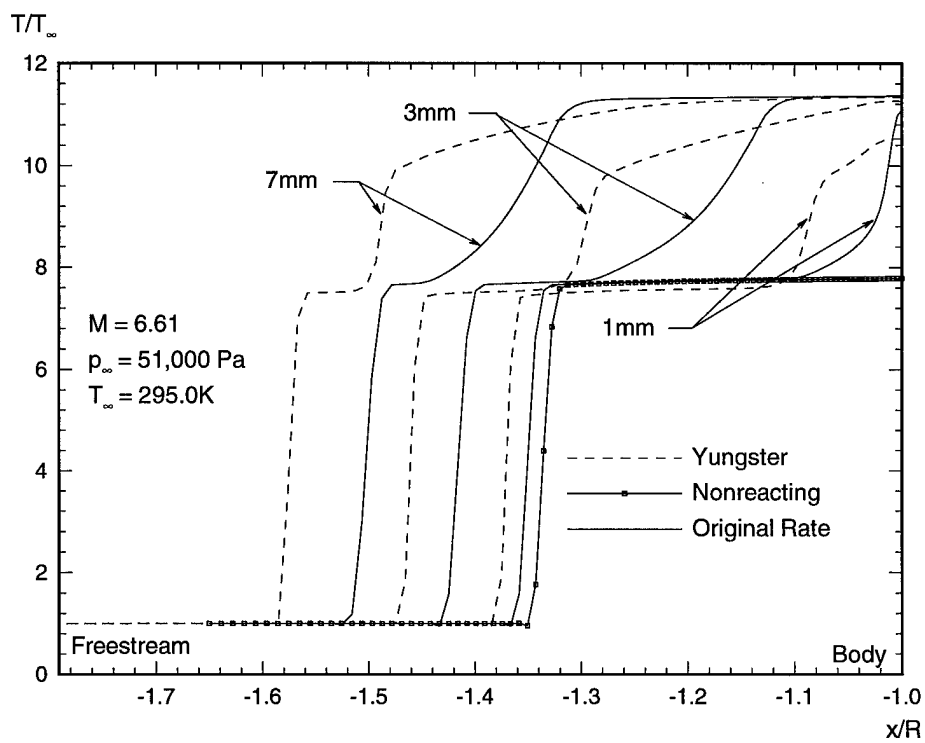


Figure 4.3 Temperature profile comparison using the original rate.

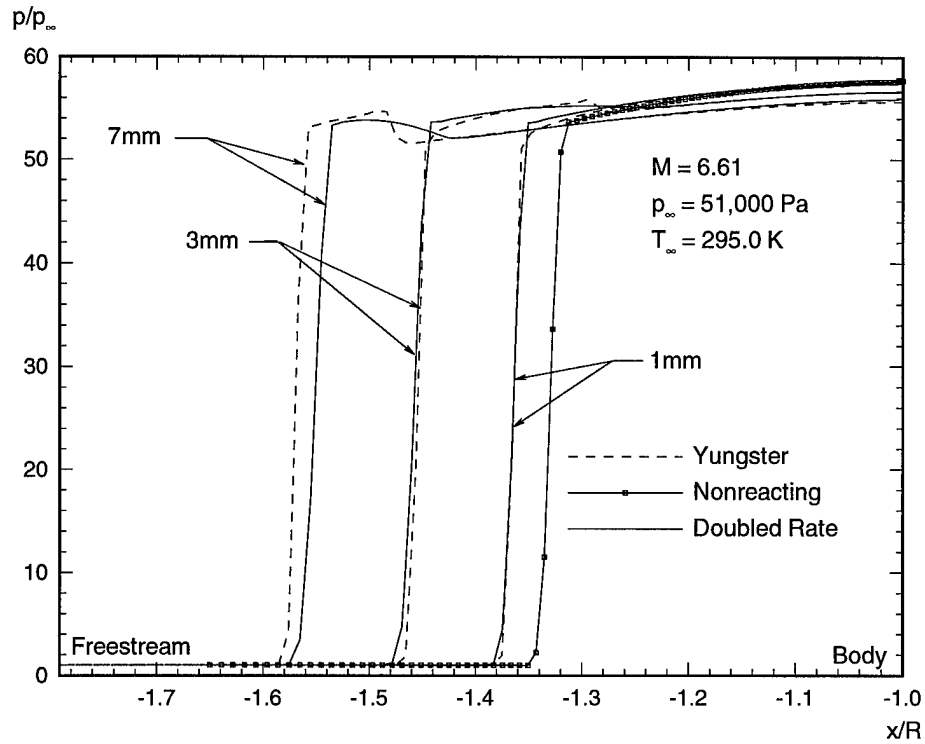


Figure 4.4 Pressure profile comparison using the doubled rate.

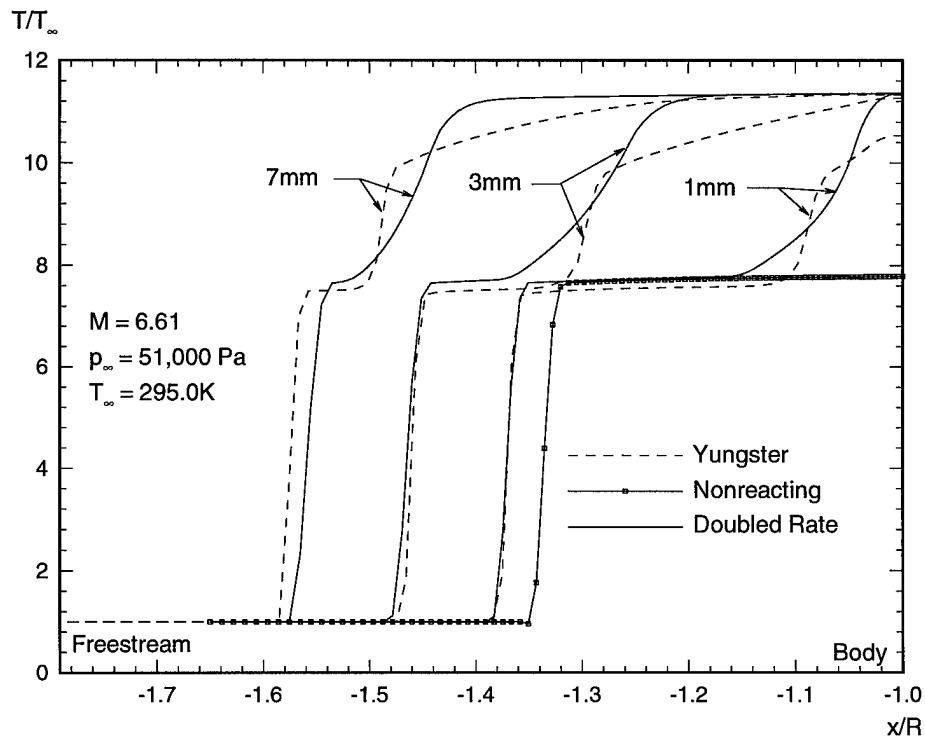


Figure 4.5 Temperature profile comparison using the doubled rate.

obtained at a lower computational cost. For the quasi-global model, 13 partial differential equations are solved at each grid point: 10 elemental or species mass equations, 2 momentum equations, and 1 energy equation. If the mechanism of Yungster and Rabinowitz were implemented, there would be 10 more mass conservation equations, bringing the total to 23. The computational cost per iteration scales roughly as the square of the number of equations. Thus, doubling the number of species almost quadruples the expense of the solution.

The outcome of the blunt body simulations is that the numerical method is validated. Conditions are representative of those in ram-accelerator flows in that strong shock waves and expansions are present, and the freestream Mach number, temperature, pressure, and mixture composition are similar to those of the simulations presented in the next chapter. With the doubling of the pre-exponential coefficient of the global reaction, the induction time and associated flowfield effects are accurately approximated. While more detailed reaction mechanisms exist, the quasi-global mechanism is suitable at a considerably lower computational cost.

CHAPTER V

RAM-ACCELERATOR SIMULATIONS

V.1 Introduction

In this chapter the ram-accelerator flowfields are presented. The purpose of these simulations is to investigate the performance of the double-cone projectile geometry. In particular, the unstart characteristics of such a projectile are sought. Stable ram-accelerator operation may be inhibited for a variety of reasons, some of which were mentioned in Chapter I. In this thesis only gasdynamic circumstances are considered, and in particular the focus is on unstarts due to combustion on the forebody.

V.2 Ram-Accelerator Geometry and Simulation Conditions

For all the simulations the solution technique described in Chapter III is utilized. The flowfields are assumed to be axisymmetric and laminar and the gas thermally perfect. As a result of the blunt body solutions discussed in Chapter IV, the pre-exponential coefficient for the global reaction is doubled.

The projectile geometry of interest was first reported by Yungster and Rabinowitz.¹ The dimensions (in *mm*) and computational grid are shown in Figure 5.1. The grid has 205 x 72 points. They are clustered in the region near the projectile shoulder to resolve the complex shockwave interactions and chemistry and near the projectile and accelerator tube surfaces to resolve boundary layers. Without adequate grid resolution, the flowfield can be substantially mispredicted. In inviscid simulations at Mach 11 (not included here,) a coarse mesh in the shoulder region resulted in a slightly weaker transmitted shock; consequently ignition did not occur until behind the reflected shockwave. On an improved grid the ignition moved upstream to the transmitted shock, in agreement with the viscous results presented.

A no-slip condition is applied at the projectile surface and the accelerator tube wall. Note that the tube wall moves at a velocity u_∞ with respect to the projectile. There are

1. See Yungster and Rabinowitz (1993).

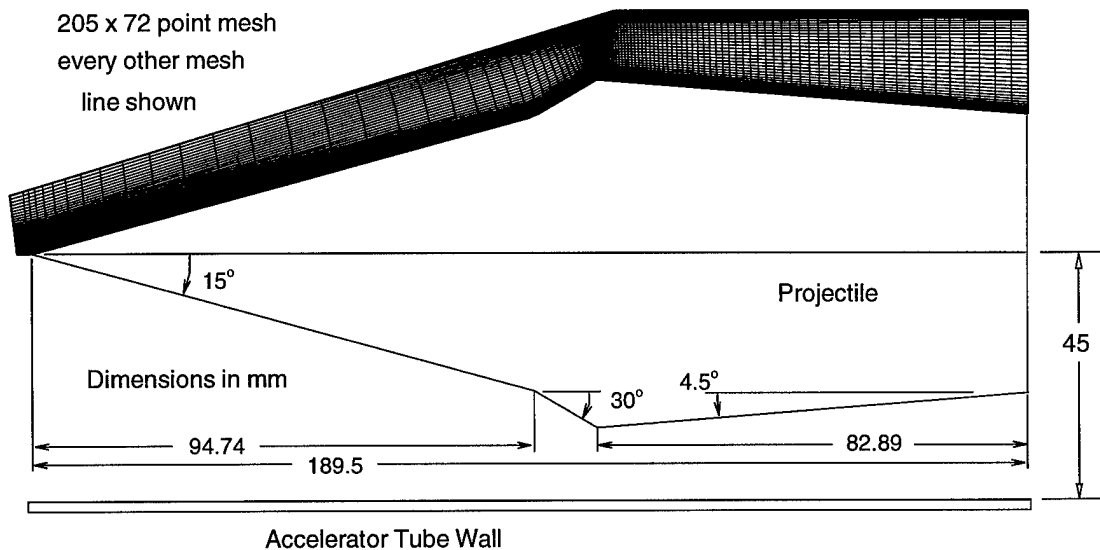


Figure 5.1 Ram-accelerator computational mesh and projectile geometry.

several cells ahead of the projectile where a centerline boundary condition is implemented. The inflow is supersonic and properties along the inflow boundary are set to freestream conditions. Zeroth-order extrapolation is applied at the outflow boundary.

The simulations do not consider the region behind the projectile, referred to as the wake, for several reasons. First of all, extending the computational domain necessitates many more grid points. In some region behind the projectile base, flow is subsonic. For the lower projectile speeds, the subsonic region can extend many projectile lengths downstream. The entire subsonic region must be included within the domain for the combined system of partial differential equations and boundary conditions to be well-posed. Such a large number of additional grid points markedly increases the cost of the simulation. Additionally this subsonic region converges much more slowly than the rest of the flowfield because of its elliptic character. As a result, many more iterations are required, also increasing the cost of the solutions. Finally, while some mechanisms of unstart rely on thermal choking of the subsonic flow in the projectile wake, the current study focuses on forebody preignition of the fuel. While the inclusion of the wake in the simulation can be valuable, it is not necessary for the present investigation.

The freestream gas is a methane-air mixture with equivalence ratio of 0.5; that is, there is one-half of the fuel needed for a stoichiometric mixture. The composition is

$CH_4 + 4 O_2 + 15.04 N_2$, where nitrogen is a diluent. The freestream conditions specified are $p_\infty = 1 \text{ atm}$ and $T_\infty = 300 \text{ K}$. Five different projectile speeds are considered: 2459.2, 3161.8, 3864.4, 4567.0, and 5269.6 m/s , corresponding to Mach numbers of 7, 9, 11, 13, and 15.

For the solutions presented, the residual is reduced at least five orders of magnitude. Each simulation required between 12,500 and 15,000 iterations, except for the Mach 9 case which required 22,500 iterations. Runs were carried out on two machines. On a single-processor Sun SparcStation 10, each 1000 iterations took 11 hours. The same calculations require about 6 hours on a single-processor SGI R4400 Indigo.

V.3 Discussion of the Flowfields

To clarify the discussion, the features of the ram-accelerator flowfield are introduced. A schematic of the flowfield is shown in Figure 5.2. The flow is from left to right. The shock S1 is formed by the projectile tip and is called the initial shock. The ramp shock is labelled S2 and results from the increase in cone half-angle. These two shocks coalesce into the transmitted shock, S3; after intersecting with the accelerator tube wall, it is called the reflected shock, S4. Behind the projectile shoulder, flow is separated due to the interaction between the reflected shock and the boundary layer along the projectile surface. Thorough discussion of this separation bubble is postponed to Section V.4. Behind this separation, flow reattaches; as a result, a reattachment shock, S5, is formed.

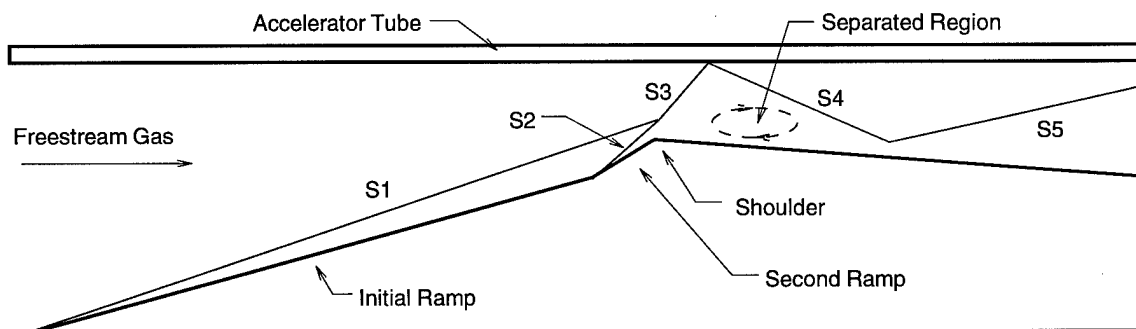


Figure 5.2 Features of the ram-accelerator flowfield.

The schematic illuminates only the shock system. Not shown are a variety of contact surfaces, expansions, energy-release fronts, and their interactions with the shockwaves and each other. For the runs at lower projectile velocities, there is also a small separation at the beginning of the second ramp. Because of these interacting waves, the chemical reactions occurring in the mixture, and the viscous effects of the boundary layers and separated regions, the flowfields presented are highly complex.

Some of the features described are seen in Figure 5.3, showing the Mach number contours for each projectile velocity, and Figure 5.4, showing the density contours. The shock system is clearly delineated in both figures, but the separation behind the projectile shoulder is more evident in the Mach number contours. The energy-release fronts are not apparent; they are revealed in mass fraction contour plots. The boundary layer along the projectile surface is recognizable; however, the accelerator tube boundary layer is obscured because the velocity gradient at the accelerator tube wall is much lower.

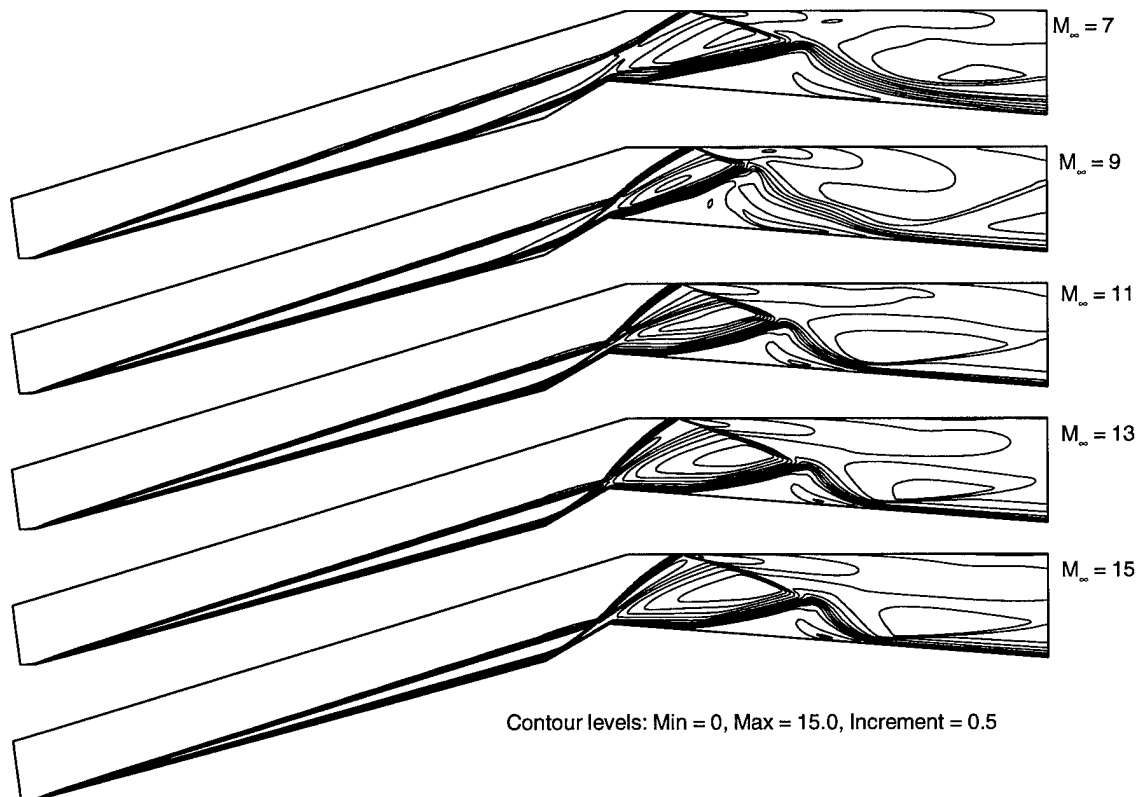


Figure 5.3 Mach number contours.

For the $M_\infty = 7$ case, a smaller separation at the beginning of the second ramp effectively rounds the compression corner; in place of the S2 shock, weaker compression waves form off the separation. As the speed increases, the corner separation diminishes in size until flow is completely attached at $M_\infty = 15$.

At the point where the initial and ramp shocks combine to form the transmitted shock, a contact surface divides the downstream flow into two parts. The gas that has passed through the S1 and S2 shockwaves is not compressed as much as that which has passed through the transmitted shock. Thus, the contact surface divides gases at two different states. This state difference is propagated downstream and can affect the ignition location.

In the projectile boundary layer the gas is heated significantly. The methane mass fraction is plotted in Figure 5.5 and shows that the boundary layer is hot enough to ignite the fuel at all the velocities considered. For the $M_\infty = 7$ case, burning is limited to the boundary layer. The burned gas flows into the separation bubble and out of the domain

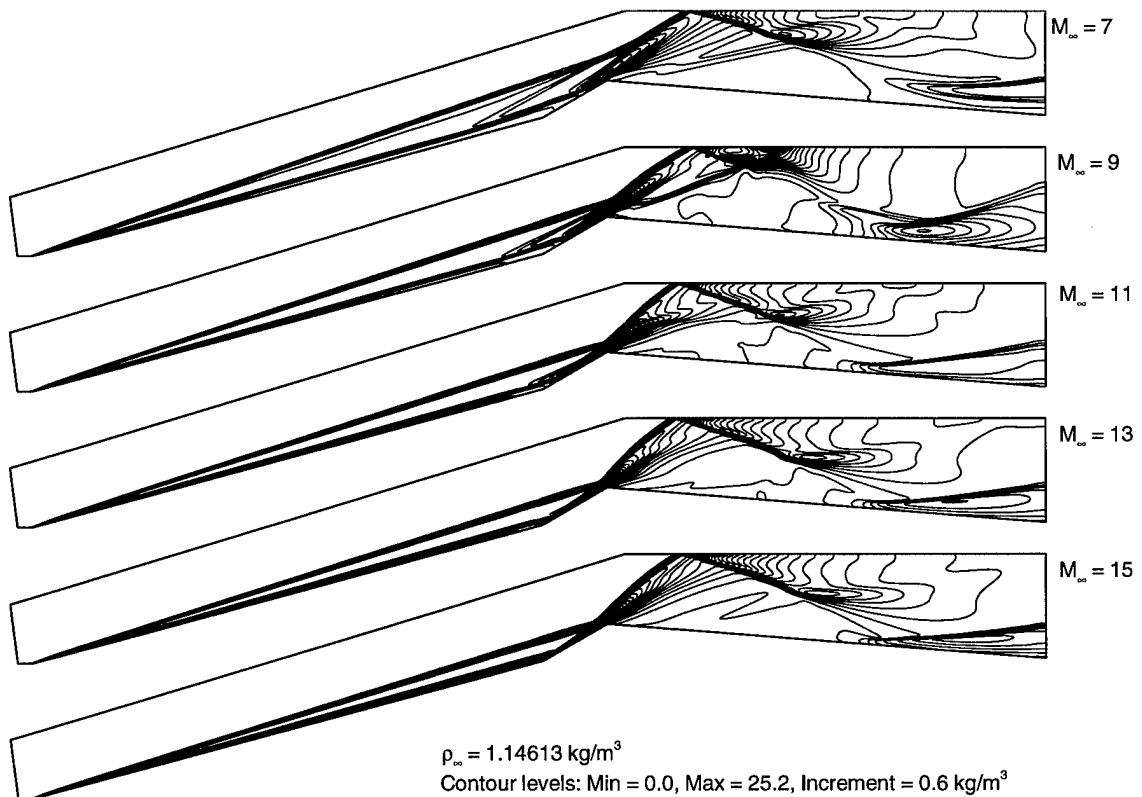


Figure 5.4 Density contours.

without igniting the rest of the flowfield. Although gas is burning ahead of the projectile, not enough energy is released to cause unstart.

For the Mach 9 case, the reflected shock is strong enough to ignite the gas. In the $M_\infty = 11$ case the transmitted shock ignites the gas. However, the gas that has passed through the initial and ramp shocks is not as highly compressed and heated, so it is not burned until it reaches the reflected shock. The transmitted and ramp shocks ignite the flow at Mach numbers of 13 and 15; there is a small induction zone behind the ramp shock in the $M_\infty = 13$ case that is not present at Mach 15.

While the methane mass fraction contours crisply illuminate the burned and unburned regions of the flow, they give the impression that once the fuel is burned there are no more chemical reactions. Carbon dioxide mass fractions, shown in Figure 5.6, indicate this is not the case. After the methane is consumed, carbon atoms are distributed between CO and CO_2 . For hotter temperatures, the balance shifts toward carbon monoxide; at

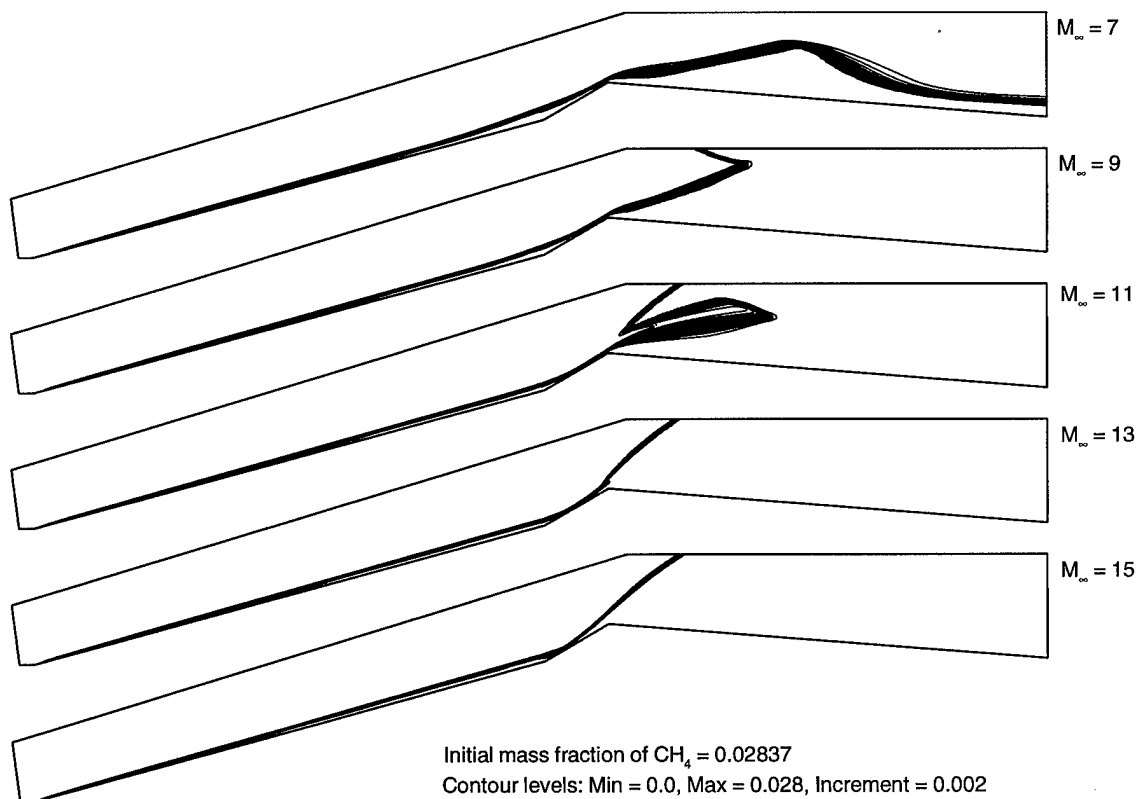


Figure 5.5 Methane mass fraction contours.

relatively lower temperatures, CO_2 dominates. For the Mach 7 case, the temperature in the separation bubble (behind the projectile shoulder) is roughly 3200 K, and carbon dioxide concentrations are high. At increasing projectile velocities, the temperature of the gas in the separation bubble rises. For the Mach 13 case the temperature is ~ 4000 K, and there is practically no CO_2 . For the higher speed cases, the state difference resulting from the different S1/S2 and S3 shock strengths is visible. Flow near the tube wall is hotter because it has come through the transmitted shock, and there is less carbon dioxide; as it expands downstream, it cools, and the CO_2 fraction increases.

The different cases demonstrate the ability of the quasi-global mechanism to distinguish subtle differences in gas conditions, in particular the detection of the induction zone behind the ramp shock in the Mach 13 case and the state difference in the Mach 11 case. The mass fraction contours of carbon dioxide and other species (not presented here) establish that all the species included in the gas model are significant in some region of the

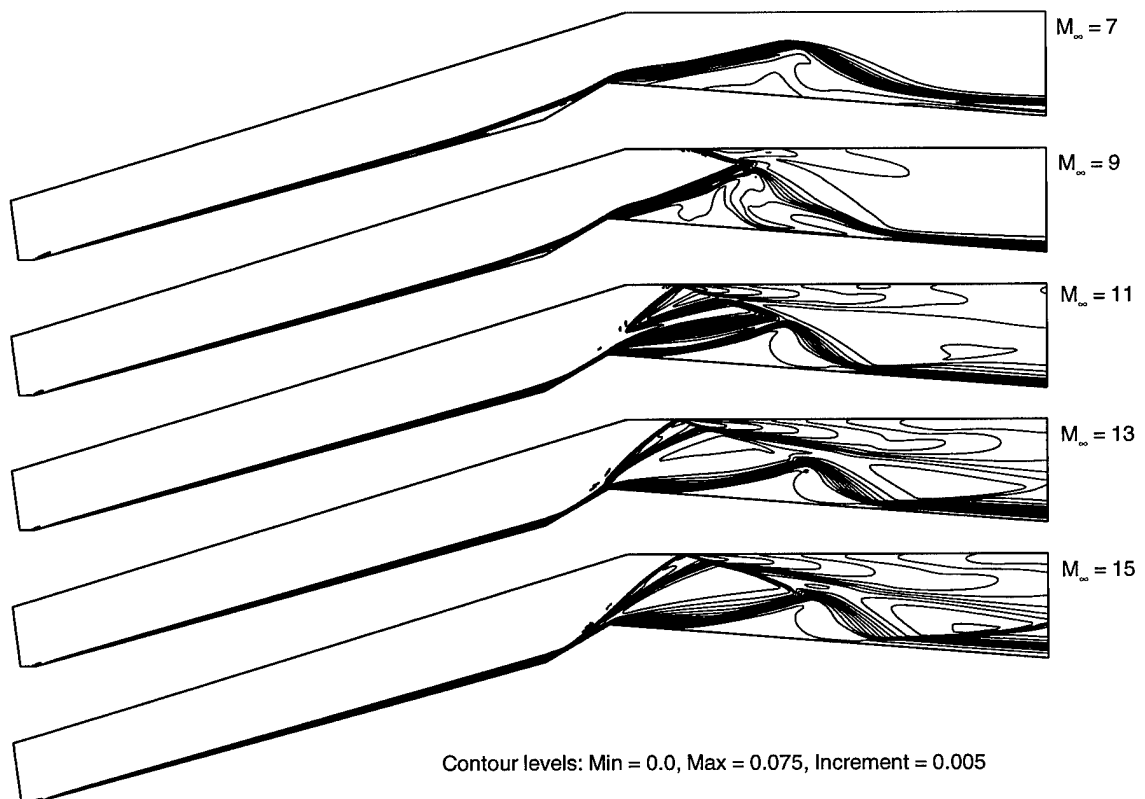


Figure 5.6 Carbon dioxide mass fraction contours.

flowfield. This suggests that simulations including fewer species may not be adequate for ram-accelerator applications. In particular the gas composition in high temperature regions may suffer.

As the projectile velocity increases, the ignition location moves upstream. The double-cone geometry was designed to delay combustion on the forebody by using a shallower initial cone angle; the second ramp initiates combustion, which primarily occurs on the afterbody. The simulations show that through Mach 15, at least, the projectile performs as intended. There is little combustion on the forebody upstream of the second ramp. Although there is some burning in the forebody boundary layer, it does not significantly affect the flowfield.

The peak temperature in the Mach 15 case is approximately 6000 K, which is at the limit of the curve fits used for calculating the equilibrium constants. Additionally the assumption that nitrogen does not react is questionable at this high temperature. Nonetheless, simulations for $M_\infty = 17$ and $M_\infty = 19$ have been carried out. Mach number contours for these flowfields are shown in Figure 5.7, and methane mass fraction contours are presented in Figure 5.8. They suggest that the initial shockwave is strong enough to ignite the gas at Mach 19, but not at Mach 17. The peak temperatures in these flowfields are observed along the forebody surface. Since nitrogen is not allowed to dissociate, the temperatures are artificially high. Consequently the simulations overpredict the expansion of the gas behind the initial shock. Despite this, unstart is not observed. If the gas model is

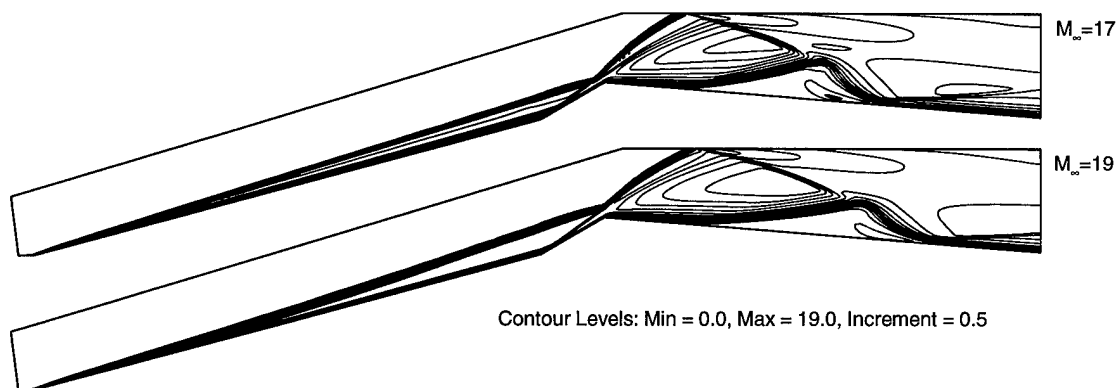


Figure 5.7 Mach number contours for Mach 17 and Mach 19 cases.

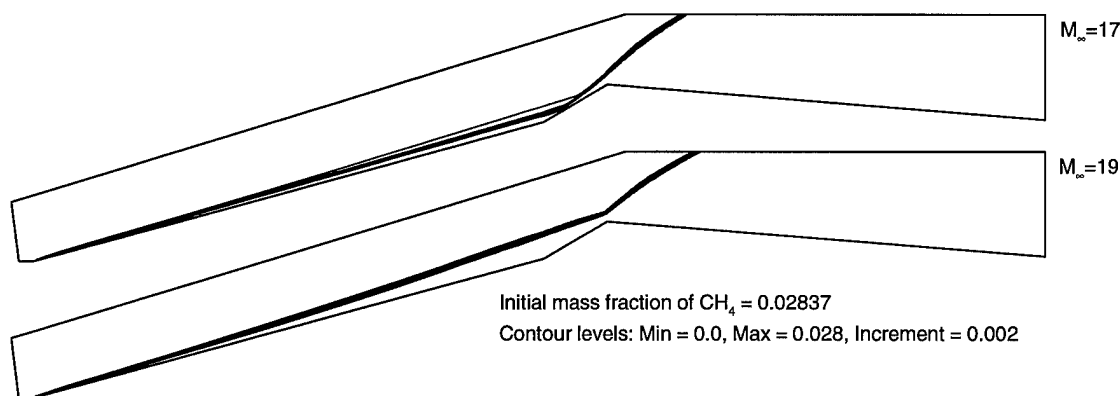


Figure 5.8 Methane mass fraction contours for Mach 17 and Mach 19 cases.

accurate, the simulations suggest that the projectile can be accelerated to Mach 19 without disrupting stable operation.

V.4 Discussion of the Separation Bubble

Particular attention is now given to the separation bubble generated by the impingement of the reflected shock on the projectile boundary layer. For $M_\infty = 9$ case the bubble is larger and fills more of the available tube cross-section than for the other projectile speeds; additionally the shape of the recirculation region is not the same. In this section, the factors influencing the size and shape of the separation bubble behind the projectile shoulder are investigated.

The separated region is most easily seen in the Mach number contours in Figure 5.3. Flow in the bubble is primarily subsonic. Streamlines presented in Figure 5.9, for the Mach 11 case, illuminate the region of interest. Several vortices can be seen within the separation. Mach number contours are also shown so other flowfield features can be identified and correlated to the streamline behavior.

As discussed in Section V.3, the ignition location moves upstream as the projectile velocity increases. After the gas is ignited, chemical energy is released into the flow. Consequently the temperature rises. Since the pressure and composition change only slightly, the ideal gas law stipulates the gas density must decrease. In a flow system the hot gas expands, filling a greater volume, and accelerates. This expansion affects the size of the

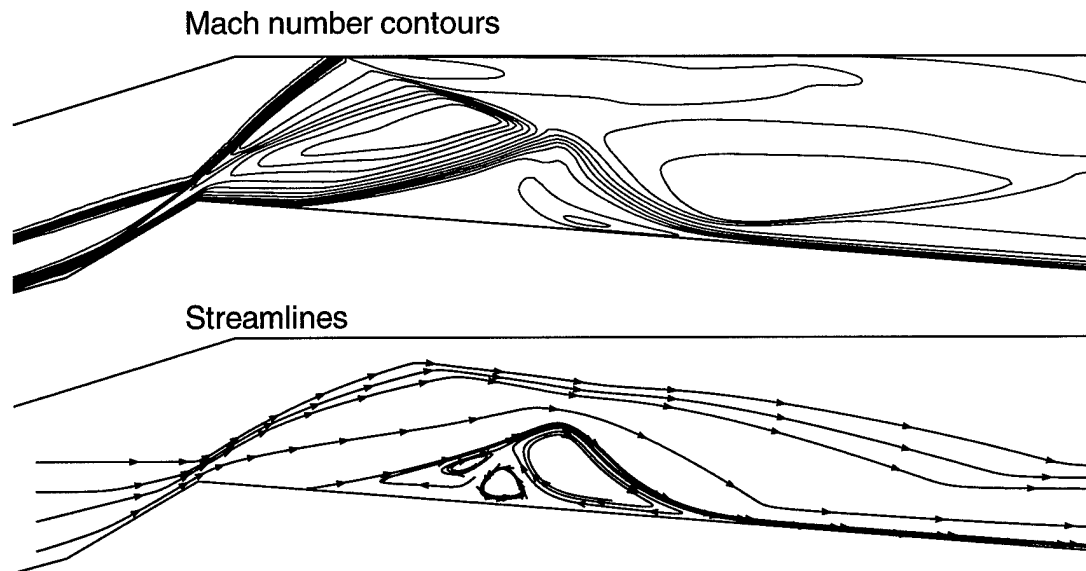


Figure 5.9 Mach number contours and streamlines illustrating the separation bubble.

separation bubble.

For the $M_\infty = 7$ case, no combustion occurs except in the forebody boundary layer. By the time the burned gas reaches the recirculation zone, any expansion due to chemical energy release has been assimilated into the flow. For projectile Mach numbers of 11, 13 and 15, combustion and significant energy release take place upstream and downstream of the separation bubble. However, for the Mach 9 case, the reflected shock ignites the gas. Chemical energy release happens entirely behind the separation. The corresponding, unbalanced expansion enhances the shockwave/boundary layer interaction that generates the separation. For the higher projectile speeds, the expansion downstream of the bubble is balanced by the energy release upstream.

To demonstrate that the chemical energy release intensifies the separation bubble, the Mach 9 simulation was repeated assuming the gas was inert. The composition is fixed to the freestream proportions. Figure 5.10 shows streamlines for the nonreacting and reacting flowfields. The differences in the separation between the Mach 9 case and the higher velocities can be seen by comparing Figures 5.9 and 5.10. For the streamlines starting near the left edge of each flowfield, the streamline origins have the same coordinates. An arrow marks the upstream limit of the separation bubble. The arrows and streamlines clearly

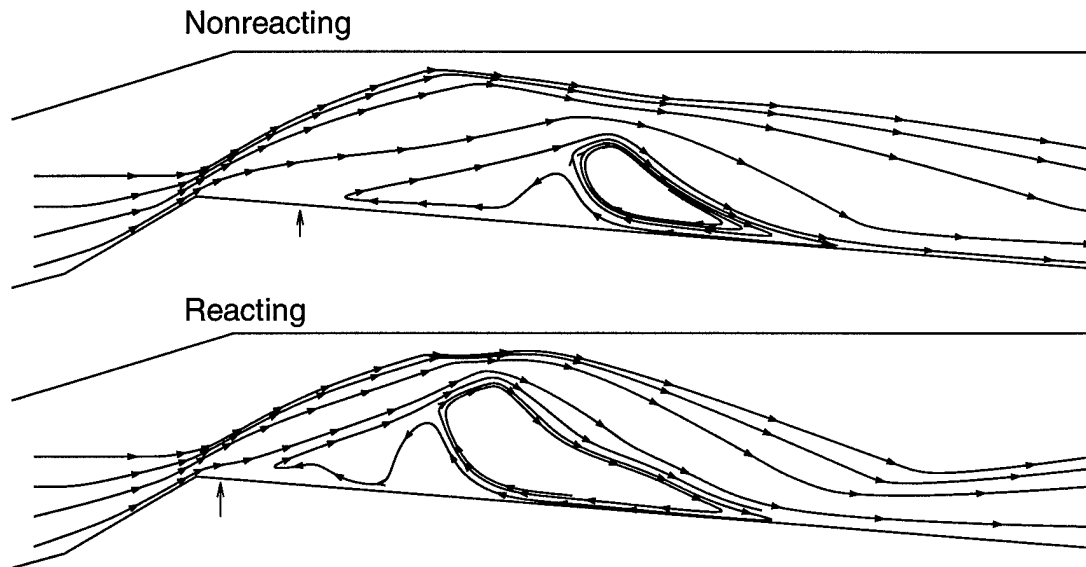


Figure 5.10 Streamlines showing expansion for nonreacting and reacting Mach 9 flow.

show the separation is larger for the reacting case, extending closer to both the tube wall and the projectile shoulder. Behind the reflected shock, the streamlines turn away from the accelerator tube more severely in the reacting solution, indicating more expansion.

V.5 Unstart Characteristics

Unstart was not observed for any of the projectile velocities considered. The size of the separation bubble at Mach 9 is cause for concern, though. For slightly different conditions, enough of the tube area might be obstructed to choke the flow. In simulations carried out by Soetrisno et. al.² on canted projectiles, a detonation wave propagates upstream when the flow chokes. The detonation wave passes the projectile tip, burning all the fuel prematurely, and the projectile accordingly loses thrust. Once the detonation starts moving upstream, stable operation is lost. Whether or not the separation bubble would unstart the flow is not clear, though. If the flow choked, a detonation wave moving upstream would alter the shock structure around the projectile. A change in the shock system might reduce the size of the separation bubble, allowing the necessary mass flow. Further study is needed to determine the role of factors other than projectile speed on the

2. See Soetrisno, Imlay, and Roberts (1993).

size of the separation, in particular the gas composition and the tube fill pressure.

The double-cone geometry was designed to delay or eliminate unstarts due to forebody ignition of the fuel. From the simulations, it appears that the geometry accomplishes this objective. For projectile Mach numbers from 7 to 15, the initial shock did not induce combustion. The simulation at Mach 19, although questionable because of the high temperatures reached, suggests that even when the initial shockwave ignites the gas stable operation is realized. Further modifications of the geometry or operational parameters (gas composition and fill pressure) may be required to eliminate unstarts caused by mechanical or thermal choking.

CHAPTER VI

CONCLUSIONS

VI.1 Conclusions

The key findings of the research presented in this thesis are summarized in this section. Remarks are made about the chemistry model and its suitability for future studies. Some statements concerning the modified diagonal implicit scheme are made. Finally, the results of the ram-accelerator simulations are summarized.

The most important results of the blunt body simulations are the findings concerning the quasi-global methane reaction mechanism. The pressure and temperature profiles highlight the limitations of the model. In particular, the details of the reaction front are not well predicted. Temperature profiles are smeared in the energy-release zone. As will be explained below, for ram-accelerator flowfields the smearing of the reaction front may not significantly affect the flowfield. Because the single, global reaction represents a number of detailed reactions, its range of applicability is restricted; however, with calibration to established numerical or experimental data, the quasi-global mechanism provides a reasonable estimate of the induction time. The main advantage of the model is that it is computationally less expensive than a more detailed mechanism.

To the author's knowledge, this thesis is the first application of the modified diagonal implicit scheme to combusting flows. Previous applications have been for atmospheric reentry simulations. A problem with the scheme is that it does not preclude the computation of negative mass fractions for the replaced species. This difficulty has not been reported previously. The negative mass fractions are not the result of discretization error or floating-point arithmetic. Negative densities develop because the algorithm relaxes each species using a different time scale, and at the same time elemental mass conservation is strictly enforced. Even if the negative mass fractions do not prevent the algorithm from generating a solution, they may alter the progression of the simulation in such a way that the negative fractions remain at the final steady state. Different choices for the replaced species alter the evolution of the flowfield, and consequently some choices may

result in negative mass fractions, while others do not. At this point, careful testing through trial and error is the only method of determining if negative densities will arise.

The purpose of the research was to investigate ram-accelerator flowfields. Projectile Mach numbers ranged from 7 to 15 and beyond. As the projectile velocity was increased, combustion moved upstream. In most instances a shockwave separated the burned and unburned gases. Very few induction zones were seen, and those were very short. At a given speed, a shock that was strong enough to ignite the gas generally did so immediately. For this reason, the quasi-global model's smearing of the reaction front may not be a major drawback for ram-accelerator simulations.

The unstart characteristics of the double-cone projectile geometry were sought. For the conditions studied, no unstarts were observed. For all velocities investigated, the gas in the forebody boundary layer was burned; however, combustion does not spread to the rest of the flowfield. Simulations suggest that the initial shockwave ignites the flow above Mach 17, but that unstart does not result. On the basis of these two points, the double-cone geometry performs as designed.

An unstart appears most likely near Mach 9. A shockwave/boundary layer interaction results in a large separated region behind the projectile shoulder. The size of the separation is greatest at Mach 9 where it extends almost to the accelerator tube wall. Unstart seems most likely near this speed because, for slightly different conditions, the separation might choke the flow. The separation is largest at this speed because combustion and energy-release occur only on the downstream side of the separation bubble. Unbalanced expansion of the combustion products enhances the shockwave/boundary layer interaction, which enlarges the separation.

VI.2 Future Work

Based on the experiences endured in the research, several recommendations for future investigations can be made. The suggestions are for improvements of in two areas: physical modelling and numerical methods.

Improvements in the physical modelling of ram-accelerator flows, and hypersonic and combusting flows in general, can be further divided into two groups. First, the accuracy of

the available models can be improved. Specifically, there is no reliable chemical kinetics mechanism for the high pressure conditions in ram-accelerator flowfields. A tremendous amount of research has been, and continues to be, devoted to hydrocarbon oxidation; unfortunately the research is concentrated on subsonic flames at roughly atmospheric pressures. Typical fill pressures in experimental ram-accelerators are from 20 to 50 *atm*; after passing through several shocks and reflections, pressures reach thousands of *atms*. The lack of a reliable chemistry model prevents accurate high-pressure simulations and was the major factor for using 1 *atm* as the freestream pressure in the simulations in this thesis. Perhaps through the use of modern flow visualization techniques, such as Planar Laser Induced Fluorescence (PLIF), reliable kinetics mechanisms can be developed for high-pressure, detonation wave applications.

Once reliable experimental data is obtained, numerical simulations can be used to test newly formulated reaction mechanisms. A technique for validating combustion chemistry models is suggested by Wilson.¹ Blunt-nosed projectiles fired into detonable gases can generate unsteady, periodic flowfields, which are highly sensitive to the kinetics and flow conditions.² By comparing computational flowfield solutions to experimentally measured frequencies, the performance of the chemistry model can be assessed.

Simulations can also be improved by the inclusion of more accurate physical models. Despite the lack of a validated chemical model, ram-accelerator simulations at higher pressures should be carried out. Different fuel/oxidizer/diluent combinations should also be examined. While the author's computational resources prohibit the inclusion of the projectile wake, current supercomputers can handle the additional requirements. The assumptions of a thermally perfect mixture and laminar flow could be relaxed with the inclusion of the appropriate physical models. Presently three-dimensional and unsteady simulations are prohibitively expensive when reacting gas models are included, but with the rapid advances in computer power they are not far in the future.

The computation of negative mass fractions by the modified diagonal implicit scheme

1. See Wilson (1991).

2. In addition to Wilson, numerical solutions of these unsteady flows have been obtained by Sussman (1994) and Yungster (1994) among others.

must be addressed. Experience to date suggests that the global reaction rate form amplifies the difficulties in the current application. On the other hand, the occurrence of negative densities does not rely on the inclusion of the global reaction. The conditions that lead to negative mass fractions can be satisfied by a kinetics model comprised of detailed reactions with Arrhenius rate forms. Clearly more research must be committed to this solution advancement method.

REFERENCES

- Anderson, D. A., Tannehill, J. C., and Pletcher, R. H., (1984), *Computational Fluid Mechanics and Heat Transfer*, Hemisphere Publishing Corporation, New York.
- Bruckner, A. P., Bogdanoff, C., Knowlen, C., and Hertzberg, A., (1987), "Investigation of Gasdynamic Phenomena Associated with the Ram Accelerator Concept," AIAA Paper 87-1327.
- Candler, G. V., (1988), "The Computation of Weakly Ionized Hypersonic Flows in Thermo-Chemical Nonequilibrium," *Ph. D. Thesis*, Stanford University, Stanford, CA.
- Candler, G. V., and Olynick, D. R., (1991), "Hypersonic Flow Simulations Using A Diagonal Implicit Method," *Proceedings of the 10th International Conference on Computing Methods in Applied Sciences and Engineering*, Paris, France, Ed. R. Glowinski, pp. 29-48, Nova Sciences Publishers, Inc., New York.
- Canupp, P. W., (1992), "Computational Analyses of Hypersonic Nozzles," *M. S. Thesis*, North Carolina State University, Raleigh, NC.
- Chew, G. and Bruckner, A. P., (1994), "A Computational Study of Projectile Nose Heating in the Ram Accelerator," AIAA Paper 94-2964.
- Coffee, T. P., (1985), "On 'Simplified Reaction Mechanisms for the Oxidation of Hydrocarbon Fuels in Flames' by C. K. Westbrook and F. T. Dryer," *Combustion Science and Technology*, Vol. 43, pp. 333-339.
- Dixon-Lewis, G., (1984) "Computer Modelling of Combustion Reactions in Flowing Systems with Transport," *Combustion Chemistry*, Ed. W. C. Gardiner, Jr., pp. 21-125, Springer-Verlag New York, Inc., New York.
- Eberhardt, S., and Imlay, S., (1990), "A Diagonal Implicit Scheme for Computing Flows with Finite-Rate Chemistry," AIAA Paper 90-1577.

- Frenklach, M., Wang, H., and Rabinowitz, M. J., (1992) "Optimization and Analysis of Large Chemical Kinetic Mechanisms Using the Solution Mapping Method - Combustion of Methane," *Progress in Energy Combustion Science*, Vol. 18, pp. 47-73.
- Hassan, B., (1993), "Thermo-Chemical Nonequilibrium Effects on the Aerothermodynamics of Hypersonic Vehicles," *Ph. D. Thesis*, North Carolina State University, Raleigh, NC.
- Hassan, B., Candler, G. V., and Olynick, D. R., (1992), "The Effect of Thermo-Chemical Nonequilibrium on the Aerodynamics of Aerobraking Vehicles," AIAA Paper 92-2877.
- Hertzberg, A., Bruckner, A. P., and Bogdanoff, D. W., (1988), "Ram Accelerator: A New Chemical Method for Accelerating Projectiles to Ultrahigh Velocities," *AIAA Journal*, Vol. 26, pp. 195-203.
- Hinkey, J. B., Burnham, E. A., and Bruckner, A. P., (1992), "High Spatial Resolution Measurements of Ram Accelerator Gas Dynamic Phenomena," AIAA Paper 92-3244.
- Hirsch, C., (1988), *Numerical Computation of Internal and External Flows, Volume 1: Fundamentals of Numerical Discretization*, John Wiley & Sons, New York.
- Hirsch, C., (1990), *Numerical Computation of Internal and External Flows, Volume 2: Computational Methods for Inviscid and Viscous Flows*, John Wiley & Sons, New York.
- Imlay, S. T., Roberts, D. W., Soetrisno, M., and Eberhardt, S., (1991), "Nonequilibrium Thermo-Chemical Calculations Using a Diagonal Implicit Scheme," AIAA Paper 91-0468.
- Knowlen, C., Higgins, A. J., and Bruckner, A. P., (1994), "Investigation of Operational Limits to the Ram Accelerator," AIAA Paper 94-2967.

- Kruczynski, D. L., and Nusca, M. J., (1992), "Experimental and Computational Investigation of Scaling Phenomena in a Large Caliber Ram Accelerator," AIAA Paper 92-3245.
- Kruczynski, D., (1991), "Analysis of RAM Acceleration for High Velocity Applications," AIAA Paper 91-2488.
- Kruczynski, D., Libertore, F., and Kiwan, M., (1994), "Flow Visualization of Steady and Transient Combustion in a 120-mm Ram Accelerator," AIAA Paper 94-3344.
- Kuo, K. K., (1986), *Principles of Combustion*, John Wiley & Sons, New York.
- Li, C., Kailasanath, K., and Oran, E. S., (1992), "Stability of Oblique Detonations in Ram Accelerators," AIAA Paper 92-0089.
- Li, C., Kailasanath, K., and Oran, E. S., (1994a), "Detonation Structures on Ram Accelerator Projectiles," AIAA Paper 94-0551.
- Li, C., Kailasanath, K., and Oran, E. S., (1994b), "Detonation Structures Behind Oblique Shocks," *Physics of Fluids*, Vol. 6, No. 4, April 1994, pp. 1600-1611.
- Li, C., Kailasanath, K., Oran, E. S., Boris, J. P., and Landsberg, A. M. (1993), "Numerical Simulations of Transient Flows in Ram Accelerators," AIAA Paper 93-1916.
- Li, C., Kailasanath, K., Oran, E. S., Landsberg, A. M., and Boris, J. P., (1993), "Analysis of Transient Flows in Thermally Choked Ram Accelerators," AIAA Paper 93-2187.
- McBride, B. J., Heimel, S., Ehlers, J. G., and Gordon, S., (1963), "Thermodynamic Properties to 6000°K for 210 Substances Involving the First 18 Elements," NASA SP-3001.
- Nusca, M. J., (1993), "Numerical Simulation of Fluid Dynamics with Finite-Rate and Equilibrium Combustion Kinetics for the 120-mm Ram Accelerator," AIAA Paper 93-2182.
- Nusca, M. J., (1994), "Reacting Flow Simulation for a Large Scale Ram Accelerator,"

- AIAA Paper 94-2963.
- Nusca, M., (1991), "Numerical Simulation of Reacting Flow in a Thermally Choked RAM Accelerator Projectile Launch System," AIAA Paper 91-2490.
- Oran, E. S., and Boris, J. P., (1987), *Numerical Simulation of Reactive Flow*, Elsevier Science Publishing Co., Inc., New York.
- Rom, J., and Avital, G., (1992), "The External Propulsion Accelerator: Scramjet Thrust Without Interaction with Accelerator Barrel," AIAA Paper 92-3717.
- Sinha, N., York, B. J., Dash, S. M., Drabczuk, R., and Rolader, G. E., (1992), "Progress Towards the Development of Transient Ram Accelerator Simulation As Part Of the U. S. Air Force Armament Directorate Research Program," AIAA Paper 92-3248.
- Soetrisno, M, Imlay, S. T., and Roberts, D. W., (1993), "Numerical Simulations of the Superdetonative Ram Accelerator Combusting Flowfield," AIAA Paper 93-2185.
- Soetrisno, M., and Imlay, S. T., (1991), "Simulation of The Flowfield of a Ram Accelerator," AIAA Paper 91-1915.
- Soetrisno, M., Imlay, S. T., and Roberts, D. W., (1992), "Numerical Simulations of The Transdetonative Ram Accelerator Combusting Flowfield on a Parallel Computer," AIAA Paper 92-3249.
- Srulijes, J., Smeets, G., and Seiler, F., (1992), "Expansion Tube Experiments for the Investigation of Ram-Accelerator-Related Combustion and Gasdynamic Problems," AIAA Paper 92-3246.
- Stull, D. R., (1965), *JANAF Thermochemical Tables*, by Dow Chemical Company, Thermal Research Laboratory, Clearinghouse for Federal Scientific and Technical Information, Springfield, VA.

- Stull, D. R., and Prophet, H., (1971), "JANAF Thermochemical Tables, 2nd. Edition," NSRDS-Report 37, National Bureau of Standards.
- Sussman, M., (1994), "A Computational Study of Unsteady Shock Induced Combustion of Hydrogen-Air Mixtures," AIAA Paper 94-3101.
- Tivanov, G., and Rom, J., (1993), "Investigation of Hypersonic Flow of a Detonable Gas Mixture Ahead of a Forward Facing Step," AIAA Paper 93-0611.
- Tysinger, T. L., and Caughey, D. A., (1991), "Implicit Multigrid Algorithm for the Navier-Stokes Equations," AIAA Paper 91-0242.
- Vincenti, W. G., and Kruger, C. K., (1965), *Introduction to Physical Gas Dynamics*, Krieger Publishing Co., Florida.
- Weirs, V. G., and Candler, G. V., (1994), "Ram-Accelerator Simulations Using Elemental Conservation Equations," AIAA Paper 94-2966.
- Westbrook, C. K., and Dryer, F. L., (1981), "Simplified Reaction Mechanisms for the Oxidation of Hydrocarbon Fuels in Flames," *Combustion Science and Technology*, Vol. 27, pp. 31-43.
- Wilke, C. R., (1950), "A Viscosity Equation for Gas Mixtures," *Journal of Computational Physics*, Vol. 18, pp. 517-519.
- Wilson, G. J., (1991), "Computation of Steady and Unsteady Shock-Induced Combustion Over Hypervelocity Blunt Bodies," *Ph. D. Thesis*, Stanford University, Stanford, CA.
- Yee, H. C., (1989), "A Class of High-Resolution Explicit and Implicit Shock-Capturing Methods," NASA TM-101088.
- Yoon, S. and Jameson, A., (1987), "An LU-SSOR Scheme for the Euler and Navier-Stokes Equations," AIAA Paper 87-0600.

- Yoon, S. and Jameson, A., (1988), "A Lower-Upper Symmetric-Gauss-Seidel Method for the Euler and Navier-Stokes Equations," *AIAA Journal*, Vol. 26, Sept. 1988, pp. 1025-1026.
- Yungster, S., (1991), "Navier-Stokes Simulation of the Supersonic Combustion Flowfield in a Ram Accelerator," AIAA Paper 91-1916.
- Yungster, S., (1992), "Numerical Study of Shock-Wave/Boundary-Layer Interactions in Premixed Combustible Gases," *AIAA Journal*, Vol. 30, No. 10, October 1992, pp.2379-2387.
- Yungster, S., and Rabinowitz, M. J., (1993), "Numerical Study of Shock-Induced Combustion in Methane-Air Mixtures," AIAA Paper 93-1917.
- Yungster, S., and Radhakrishnan, K., (1994), "Fully Implicit Time Accurate Method For Hypersonic Combustion: Application to Shock-Induced Combustion Instability," AIAA Paper 94-2965.
- Yungster, S., Eberhardt, S., and Bruckner, A. P., (1991), "Numerical Simulation of Hypervelocity Projectiles in Detonable Gases," *AIAA Journal*, Vol. 29, No. 2, February 1991, pp.187-199.

APPENDIX A

THE ELEMENTAL FORMULATION

In this section the relationship between two sets of mass conservation equations is made clear. Typically the species mass conservation equations are employed; one equation is included for each chemical species in the gas model. This is referred to as the *species formulation*. In this thesis some of the species equations are replaced by elemental mass conservation equations.¹ The set comprised of ne elemental equations and $ns - ne$ species equations is called the *elemental formulation*.

Both formulations describe the same physics. Both implicitly conserve total mass. The species formulation implicitly conserves elemental mass, and the elemental formulation implicitly conserves the masses of the *replaced* species. Replaced species are those whose mass conservation equation has been replaced by an elemental conservation equation. The *retained* species have conservation equations explicitly included in the set comprising the elemental formulation.

The conservation of mass is an expression of the conservation of atoms. Whether species masses or elemental masses are considered, the number of atoms (or moles) of each element must be conserved. The relationship between the two formulations is based on the conservation of atoms of each element. The total number of moles of a given element e in the mixture is the sum of the moles of that element in each chemical species s :

$$\frac{\tilde{\rho}_e}{M_e} = a_{e,1} \frac{\rho_1}{M_1} + \dots + a_{e,ns} \frac{\rho_{ns}}{M_{ns}} = \sum_{s=1}^{ns} a_{e,s} \frac{\rho_s}{M_s}. \quad (\text{A.1})$$

The species or elemental density (*mass / volume*) divided by the molecular weight is the number of atoms (*moles / volume*). The coefficient $a_{e,s}$ is the number of atoms of element e in a molecule of species s . Consider carbon dioxide, for example. For CO_2 , $a_{C,CO_2} = 1$ and $a_{O,CO_2} = 2$.

The governing equations are written in terms of densities. A more convenient way of

1. The reasons for including the elemental equations are discussed in Chapter III, as well as in Candler and Olynick (1991) and Hassan, Candler, and Olynick (1992).

writing equation A.1 is to include the molecular weights in the coefficients:

$$\tilde{\rho}_e = \alpha_{e,1}\rho_1 + \dots + \alpha_{e,ns}\rho_{ns} = \sum_{s=1}^{ns} \alpha_{e,s}\rho_s, \quad (\text{A.2})$$

where

$$\alpha_{e,s} = a_{e,s} \frac{M_e}{M_s}. \quad (\text{A.3})$$

Given the constituent species of the gas model, the coefficients $\alpha_{e,s}$ can be determined. In matrix form, equation A.2 can be written

$$\begin{bmatrix} \tilde{\rho}_1 \\ \vdots \\ \tilde{\rho}_{ne} \end{bmatrix} = \begin{bmatrix} \alpha_{1,1} & \dots & \alpha_{1,ns} \\ \vdots & \ddots & \vdots \\ \alpha_{ne,1} & \dots & \alpha_{ne,ns} \end{bmatrix} \begin{bmatrix} \rho_1 \\ \vdots \\ \rho_{ns} \end{bmatrix}. \quad (\text{A.4})$$

At times it is necessary to determine the replaced densities, given the elemental and retained densities. The coefficient matrix can be inverted to yield

$$\begin{bmatrix} \rho_1 \\ \vdots \\ \rho_{ne} \end{bmatrix} = \begin{bmatrix} \beta_{1,1} & \dots & \beta_{1,ns} \\ \vdots & \ddots & \vdots \\ \beta_{ne,1} & \dots & \beta_{ne,ns} \end{bmatrix} \begin{bmatrix} \tilde{\rho}_1 \\ \vdots \\ \tilde{\rho}_{ne} \\ \rho_{ne+1} \\ \vdots \\ \rho_{ns} \end{bmatrix}. \quad (\text{A.5})$$

For the gas model used in this thesis, there are 10 species and 4 elements ($ns = 10$ and $ne = 4$.) The elements and their indices are

Element:	<i>C</i>	<i>H</i>	<i>O</i>	<i>N</i>
Index:	1	2	3	4

The species and their indices are

Species:	<i>CH₄</i>	<i>O₂</i>	<i>H₂</i>	<i>N₂</i>	<i>CO₂</i>	<i>CO</i>	<i>H₂O</i>	<i>OH</i>	<i>O</i>	<i>H</i>
Index:	1	2	3	4	5	6	7	8	9	10

In this case the first four species are replaced, while the rest are retained. The corresponding coefficient matrices are

$$[\alpha_{e,s}] = \begin{bmatrix} \frac{M_C}{M_{CH_4}} & 0 & 0 & 0 & \frac{M_C}{M_{CO_2}} & \frac{M_C}{M_{CO}} & 0 & 0 & 0 & 0 \\ 4\frac{M_H}{M_{CH_4}} & 0 & 2\frac{M_H}{M_{H_2}} & 0 & 0 & 0 & 2\frac{M_H}{M_{H_2O}} & \frac{M_H}{M_{OH}} & 0 & 1 \\ 0 & 2\frac{M_O}{M_{O_2}} & 0 & 0 & 2\frac{M_O}{M_{CO_2}} & \frac{M_O}{M_{CO_2}} & \frac{M_O}{M_{H_2O}} & \frac{M_O}{M_{MH}} & 1 & 0 \\ 0 & 0 & 0 & 2\frac{M_N}{M_{N_2}} & 0 & 0 & 0 & 0 & 0 & 0 \end{bmatrix} \quad (A.6)$$

and

$$[\beta_{e,s}] = \begin{bmatrix} \frac{M_{CH_4}}{M_C} & 0 & 0 & 0 & -\frac{M_{CH_4}}{M_{CO_2}} & -\frac{M_{CH_4}}{M_{CO}} & 0 & 0 & 0 & 0 \\ 0 & 0 & 1 & 0 & -\frac{M_{O_2}}{M_{CO_2}} & -\frac{1}{2}\frac{M_{O_2}}{M_{CO}} & -\frac{1}{2}\frac{M_{O_2}}{M_{H_2O}} & -\frac{1}{2}\frac{M_{O_2}}{M_{OH}} & -1 & 0 \\ -4\frac{M_H}{M_C} & 1 & 0 & 0 & 2\frac{M_{H_2}}{M_{CO_2}} & 2\frac{M_{H_2}}{M_{CO}} & -\frac{M_{H_2}}{M_{H_2O}} & -\frac{1}{2}\frac{M_{H_2}}{M_{OH}} & 0 & -1 \\ 0 & 0 & 0 & 1 & 0 & 0 & 0 & 0 & 0 & 0 \end{bmatrix} \quad (A.7)$$

APPENDIX B

PHYSICAL CONSTANTS

In this appendix constants and parameters used in various physical models are listed. Data is from a variety of sources. Table B.1 contains constants and parameters which specify the behavior of each species in the gas.

Collision integrals must be calculated to determine the transport coefficients. These integrals are functions of the reduced temperature, T^* . For each species the Lennard-Jones 6-12 potentials are required to determine the reduced temperature. The curve fit polynomial for the collision integrals is

$$f(T^*) = a_0 + a_1 T^* + a_2 T^{*2} + a_3 T^{*3} + a_4 T^{*4}. \quad (\text{B.1})$$

Table B.2 lists the Lennard-Jones parameters, while the collision integral curve fit coefficients are given in Table B.3. Note that there is a separate curve fit for H_2O because of its polar nature.

Curve fits are used to specify the Gibbs free energies of each species which are required for the determination of the equilibrium constant for each chemical reaction. The curve fit is given by

$$\frac{g_s}{RT} = C_{1,s} (1 - \ln T) - \frac{C_{2,s}}{2} T - \frac{C_{3,s}}{6} T^2 - \frac{C_{4,s}}{12} T^3 - \frac{C_{5,s}}{20} T^4 + \frac{C_{6,s}}{T} - C_{7,s}. \quad (\text{B.2})$$

Two sets of coefficients are listed. The first set is valid for temperatures between 300 K and 1000 K and is presented in Table B.4. The second set is valid from 1000 K to 6000 K and is shown in Table B.5. Since nitrogen is not included in any of the chemical reactions, its Gibbs' free energy is not required.

The chemical kinetics mechanism is listed in Table B.6. Included are the 12 reactions and the associated parameters for Arrhenius form reaction rates.

Table B.1: Molecular Constantsⁱ

Index	Species, s	M_s (kg/kmol)	h_s^o (J/kg)	$\frac{c_{v,s}}{\left[\frac{R}{M_s}\right]}$	$ndeg(s)$	$\theta_{v,s,m}$ (K)
1	CH_4	16.043	-4.649153e6	3.0	9	1879.1(3) 2207.2(2) 4196.4 4343.4(3)
2	O_2	32.00	0.0	2.5	1	2273.7
3	H_2	2.016	0.0	2.5	1	6338.5
4	N_2	28.016	0.0	2.5	1	3392.1
5	CO_2	44.011	-8.907252e6	2.5	4	960.14(2) 1932.2 3380.3
6	CO	28.011	-3.930740e6	2.5	1	3121.6
7	H_2O	18.016	-1.337154e7	3.0	3	2294.4 5262.0 5404.0
8	OH	17.008	2.286420e6	2.5	1	5374.2
9	O	16.00	1.551512e7	1.5	0	-
10	H	1.008	2.154376e8	1.5	0	-

i. The data is from Stull (1965), except for the characteristic temperature of vibration for OH which is taken from Stull and Prophet (1971).

Table B.2: Molecular parameters for Lennard-Jones 6-12 potentialsⁱ

Species, <i>s</i>	σ_s (nm)	$\frac{\epsilon_s}{k_B}$ (K)
CH ₄	0.3758	148.6
O ₂	0.3467	106.7
H ₂	0.2827	59.7
N ₂	0.3798	71.4
CO ₂	0.3941	195.2
CO	0.3690	91.7
H ₂ O	0.2800	260.0
OH	0.3147	79.8
O	0.3050	106.7
H	0.2070	37.0

i. Data is from Dixon-Lewis (1984).

Table B.3: Collision integral curve-fit coefficientsⁱ

$f(T^*)$	T^*	a_0	a_1	a_2	a_3	a_4
$\Omega^{(1,1)*}$	< 5.0	0.23527333×10^1	-0.13589968×10^1	0.52202460×10^0	$-0.94262883 \times 10^{-1}$	$0.64354629 \times 10^{-2}$
	5.0 - 10.0	0.12660308×10^1	-0.16441443×10^0	$0.22945928 \times 10^{-1}$	$-0.16324168 \times 10^{-2}$	$0.45833672 \times 10^{-4}$
	> 10.0	0.85263337×10^0	$-0.13552911 \times 10^{-1}$	$0.26162080 \times 10^{-3}$	$-0.24647654 \times 10^{-5}$	$0.86538568 \times 10^{-8}$
A*	< 5.0	0.11077725×10^1	$-0.94802344 \times 10^{-2}$	$0.16918277 \times 10^{-2}$	0.0	0.0
	5.0 - 10.0	0.10871429×10^1	$0.31964282 \times 10^{-2}$	$-0.89285689 \times 10^{-4}$	0.0	0.0
	> 10.0	0.11059000×10^1	$0.65136364 \times 10^{-3}$	$-0.34090910 \times 10^{-4}$	0.0	0.0
A* H ₂ O	< 10.0	0.10764205×10^1	$0.46037515 \times 10^{-1}$	$-0.13506975 \times 10^{-1}$	$0.15404522 \times 10^{-2}$	$-0.60887567 \times 10^{-4}$
	> 10.0	0.11141689×10^1	$0.48711959 \times 10^{-3}$	$-0.44570091 \times 10^{-5}$	$0.99643413 \times 10^{-8}$	$0.686639118 \times 10^{-10}$

i. Data is from Dixon-Lewis (1984).

Table B.4: Polynomial coefficients for Gibbs' free energiesⁱ: low temperature rangeⁱⁱ

Species, <i>s</i>	C_1	C_2	C_3	C_4	C_5	C_6	C_7
CH_4	4.2497678	$-6.9126562 \times 10^{-3}$	3.1602134×10^{-5}	$-2.9715432 \times 10^{-8}$	$9.5103580 \times 10^{-12}$	-1.0186632×10^4	$-9.1754991 \times 10^{-1}$
O_2	3.7189946	$-2.5167288 \times 10^{-3}$	8.5837353×10^{-6}	$-8.2998716 \times 10^{-9}$	$2.7082180 \times 10^{-12}$	-1.0576706×10^3	3.9080704
H_2	2.8460849	4.1932116×10^{-3}	$-9.6119332 \times 10^{-6}$	$9.51222662 \times 10^{-9}$	$-3.3093421 \times 10^{-12}$	-9.6725372×10^2	-1.4117850
CO_2	2.1701000	1.0378115×10^{-2}	$-1.0733938 \times 10^{-5}$	6.3459175×10^{-9}	$-1.6280701 \times 10^{-12}$	-4.8326602×10^4	1.0664388×10^1
CO	3.7871332	$-2.1709526 \times 10^{-3}$	5.0757337×10^{-6}	$-3.4737726 \times 10^{-9}$	7.721684×10^{-13}	-1.4363508×10^4	2.6335459
H_2O	4.1565016	$-1.7244334 \times 10^{-3}$	5.6982316×10^{-6}	$-4.5930044 \times 10^{-9}$	$1.4233654 \times 10^{-12}$	-3.0288770×10^4	$-6.8616246 \times 10^{-1}$
OH	3.8234708	$-1.1187229 \times 10^{-3}$	1.2466819×10^{-6}	$-2.1035896 \times 10^{-10}$	$-5.2546551 \times 10^{-14}$	3.5852787×10^3	5.8253029×10^{-1}
O	3.0218894	$-2.1737249 \times 10^{-3}$	3.7542203×10^{-6}	$-2.9947200 \times 10^{-9}$	$9.0777547 \times 10^{-13}$	2.9137190×10^4	2.6460076
H	2.50	0.0	0.0	0.0	0.0	2.5470497×10^4	$-4.6001096 \times 10^{-1}$

i. Data is from McBride, Heimel, Ehlers, and Gordon (1963).

ii. Valid for $300K < T < 1000K$.

Table B.5: Polynomial coefficients for Gibbs' free energiesⁱ: high temperature rangeⁱⁱ

Species, <i>s</i>	C_1	C_2	C_3	C_4	C_5	C_6	C_7
CH_4	1.1795744	1.0950594×10^{-2}	$-4.0622131 \times 10^{-6}$	$7.1370281 \times 10^{-10}$	$-4.7490353 \times 10^{-14}$	-9.8556627×10^3	1.2505934×10^1
O_2	3.5976129	7.8145603×10^{-4}	$-2.2386670 \times 10^{-7}$	$4.2490159 \times 10^{-11}$	$-3.3460204 \times 10^{-15}$	-1.1927918×10^3	3.7492659
H_2	3.0436897	6.1187110×10^{-4}	$-7.3993551 \times 10^{-9}$	$-2.0331907 \times 10^{-11}$	$2.4593791 \times 10^{-15}$	-8.5491002×10^2	-1.6481339
CO_2	4.4129266	3.1922896×10^{-3}	$-1.2978230 \times 10^{-6}$	$2.4147446 \times 10^{-10}$	$-1.6742986 \times 10^{-14}$	-4.8944043×10^4	$-7.2875769 \times 10^{-1}$
CO	2.9511519	1.5525567×10^{-3}	$-6.1911411 \times 10^{-7}$	$1.1350336 \times 10^{-10}$	$-7.7882732 \times 10^{-15}$	-1.4231827×10^4	6.5314450
H_2O	2.6707532	3.0317115×10^{-3}	$-8.5351570 \times 10^{-7}$	$1.1790853 \times 10^{-10}$	$-6.1973568 \times 10^{-15}$	-2.9888994×10^4	6.8838391
OH	2.8895544	9.9835061×10^{-4}	$-2.1879904 \times 10^{-7}$	$1.9802785 \times 10^{-11}$	$-3.8452940 \times 10^{-16}$	3.8811792×10^3	5.5597016
O	2.5372567	$-1.8422190 \times 10^{-5}$	$-8.8017921 \times 10^{-9}$	$5.9643621 \times 10^{-12}$	$-5.5743608 \times 10^{-16}$	2.9230007×10^4	4.9467942
H	2.50	0.0	0.0	0.0	0.0	2.5470497×10^4	$-4.6001096 \times 10^{-1}$

i. Data is from McBride, Heimel, Ehlers, and Gordon (1963).

ii. Valid for $1000K < T < 6000K$.

Table B.6: Quasi-global methane reaction mechanismⁱ

Index, r	Reaction	A ⁱⁱ	η	θ_d (K)
1	$CO + O + M \rightleftharpoons CO_2 + M$	5.9×10^{15}	0	2055
2	$OH + M \rightleftharpoons O + H + M$	8.0×10^{19}	-1.0	51,990
3	$O_2 + M \rightleftharpoons O + O + M$	5.1×10^{15}	0	57,650
4	$H_2 + M \rightleftharpoons H + H + M$	2.2×10^{14}	0	48,130
5	$H_2O + M \rightleftharpoons OH + H + M$	2.2×10^{16}	0	52,640
6 ⁱⁱⁱ	$CH_4 + 1/2 O_2 \rightleftharpoons 2H_2 + CO$	4.0×10^9	0	24,260
7	$CO + OH \rightleftharpoons CO_2 + H$	1.5×10^7	1.3	-401.0
8	$CO + O_2 \rightleftharpoons CO_2 + O$	3.1×10^{11}	0	18,850
9	$H + O_2 \rightleftharpoons OH + O$	2.2×10^{14}	0	8422
10	$O + H_2 \rightleftharpoons OH + H$	1.8×10^{10}	1.0	4462
11	$OH + H_2 \rightleftharpoons H + H_2O$	2.2×10^{13}	0	2557
12	$H_2O + O \rightleftharpoons OH + OH$	6.8×10^{13}	0	9224

i. Data is from Westbrook and Dryer (1981).

ii. Units are *mol, cm, K, sec*

iii. Global reaction, original rate. In some calculations, A_6 is doubled. Concentration exponents: $a = -0.3$, $a' = -0.5$, and $b = b' = 1.3$.

APPENDIX C

GENERALIZED COORDINATE TRANSFORMATION

The governing equations discussed in Chapter II are written in index notation, which is most easily extended to Cartesian coordinates. However, a general curvilinear coordinate system is preferred because most interesting geometries are difficult to represent efficiently in Cartesian coordinates. In this appendix the transformation between Cartesian and general curvilinear coordinates is delineated.

The Cartesian coordinate directions are x and y ; for the general curvilinear coordinates, they are ξ and η . The chain rule of calculus is used to relate derivatives in the two systems:

$$\frac{\partial \phi}{\partial x} = \frac{\partial \xi}{\partial x} \frac{\partial \phi}{\partial \xi} + \frac{\partial \eta}{\partial x} \frac{\partial \phi}{\partial \eta} \quad (\text{C.1})$$

and

$$\frac{\partial \phi}{\partial y} = \frac{\partial \xi}{\partial y} \frac{\partial \phi}{\partial \xi} + \frac{\partial \eta}{\partial y} \frac{\partial \phi}{\partial \eta} \quad (\text{C.2})$$

where ϕ is any property. The derivatives $\frac{\partial \xi}{\partial x}$, $\frac{\partial \xi}{\partial y}$, $\frac{\partial \eta}{\partial x}$ and $\frac{\partial \eta}{\partial y}$ are called the *metrics* of the transformation. With the abbreviation ξ_x for $\frac{\partial \xi}{\partial x}$ and so on for the other metrics, equations C.1 and C.2 can be written in matrix form:

$$\begin{bmatrix} \frac{\partial}{\partial x} \\ \frac{\partial}{\partial y} \end{bmatrix} = \begin{bmatrix} \xi_x & \eta_x \\ \xi_y & \eta_y \end{bmatrix} \begin{bmatrix} \frac{\partial}{\partial \xi} \\ \frac{\partial}{\partial \eta} \end{bmatrix} = [T] \begin{bmatrix} \frac{\partial}{\partial \xi} \\ \frac{\partial}{\partial \eta} \end{bmatrix} \quad (\text{C.3})$$

Inversion yields an equation for derivatives in the Cartesian space:

$$\begin{bmatrix} \frac{\partial}{\partial \xi} \\ \frac{\partial}{\partial \eta} \end{bmatrix} = \begin{bmatrix} x_\xi & y_\xi \\ x_\eta & y_\eta \end{bmatrix} \begin{bmatrix} \frac{\partial}{\partial x} \\ \frac{\partial}{\partial y} \end{bmatrix} = [T]^{-1} \begin{bmatrix} \frac{\partial}{\partial x} \\ \frac{\partial}{\partial y} \end{bmatrix}, \quad (\text{C.4})$$

where x_ξ , x_η , y_ξ , and y_η are referred to as *inverse metrics*. Equation C.3 can be expressed in terms of the inverse metrics:

$$\begin{bmatrix} \frac{\partial}{\partial x} \\ \frac{\partial}{\partial y} \end{bmatrix} = \left([T]^{-1} \right)^{-1} \begin{bmatrix} \frac{\partial}{\partial \xi} \\ \frac{\partial}{\partial \eta} \end{bmatrix} = \frac{1}{x_\xi y_\eta - x_\eta y_\xi} \begin{bmatrix} y_\eta & -y_\xi \\ -x_\eta & x_\xi \end{bmatrix} \begin{bmatrix} \frac{\partial}{\partial \xi} \\ \frac{\partial}{\partial \eta} \end{bmatrix}. \quad (\text{C.5})$$

The inverse metrics are easier to compute than the metrics, so the forms in equations C.4 and C.5 are preferred. The mesh metrics are used to evaluate the viscous terms, as discussed in Section III.4.

The surface cosines s_{ix}' , s_{iy}' , s_{jx}' , and s_{jy}' can be calculated by inspection of Figure C.1. For the $i + 1/2$ cell face, the surface is defined by

$$\bar{S}_{i+\frac{1}{2}} = \left(s_{ix}' \hat{i} + s_{iy}' \hat{j} \right) S_{i+\frac{1}{2}} \quad (\text{C.6})$$

where the cell face area is

$$S_{i+\frac{1}{2}} = \sqrt{\Delta x^2 + \Delta y^2} \quad (\text{C.7})$$

and the surface cosines are

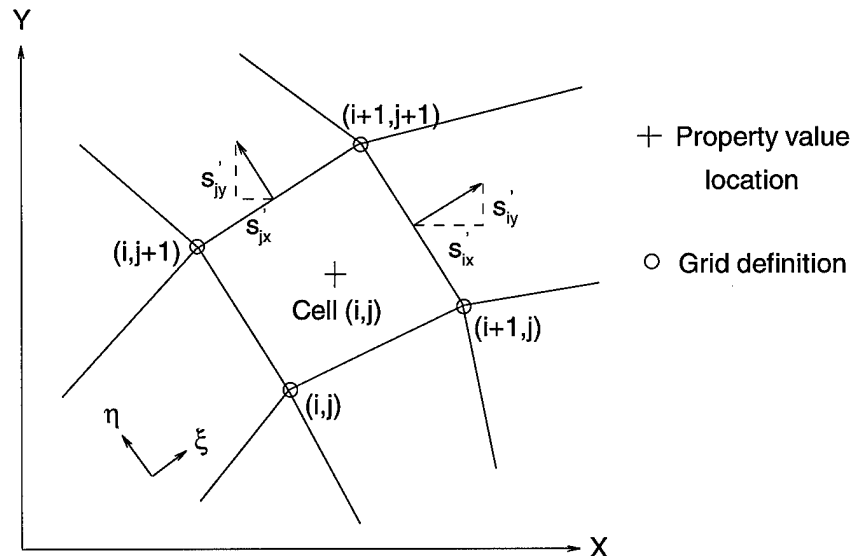


Figure C.1 Surface cosines for a representative mesh cell.

$$s_{ix}' = \frac{\Delta y}{\sqrt{\Delta x^2 + \Delta y^2}} \quad s_{iy}' = \frac{-\Delta x}{\sqrt{\Delta x^2 + \Delta y^2}}. \quad (\text{C.8})$$

Similarly for the $j + 1/2$ cell face,

$$\bar{S}_{j+\frac{1}{2}} = (s_{jx}'\hat{i} + s_{jy}'\hat{j})S_{j+\frac{1}{2}}, \quad (\text{C.9})$$

$$S_{j+\frac{1}{2}} = \sqrt{\Delta x^2 + \Delta y^2} \quad (\text{C.10})$$

and

$$s_{jx}' = \frac{-\Delta y}{\sqrt{\Delta x^2 + \Delta y^2}} \quad s_{jy}' = \frac{\Delta x}{\sqrt{\Delta x^2 + \Delta y^2}}. \quad (\text{C.11})$$

For the $i + 1/2$ cell face,

$$\Delta x = x_{i+1,j+1} - x_{i+1,j} \quad \Delta y = y_{i+1,j+1} - y_{i+1,j}, \quad (\text{C.12})$$

while for the $j + 1/2$ face,

$$\Delta x = x_{i+1,j+1} - x_{i,j+1} \quad \Delta y = y_{i+1,j+1} - y_{i,j+1}. \quad (\text{C.13})$$

The surface cosines and the mesh metrics are related by

$$s_{ix}' = \frac{\xi_x}{\sqrt{\xi_x^2 + \xi_y^2}} \quad s_{iy}' = \frac{\xi_y}{\sqrt{\xi_x^2 + \xi_y^2}} \quad (\text{C.14})$$

and

$$s_{jx}' = \frac{\eta_x}{\sqrt{\eta_x^2 + \eta_y^2}} \quad s_{jy}' = \frac{\eta_y}{\sqrt{\eta_x^2 + \eta_y^2}}. \quad (\text{C.15})$$

Finally, a formula for the cell volume is given by Hirsch:¹

$$\Omega = \frac{1}{2} [(x_{i+1,j+1} - x_{i,j})(y_{i,j+1} - y_{i+1,j}) - (x_{i,j+1} - x_{i+1,j})(y_{i+1,j+1} - y_{i,j})], \quad (\text{C.16})$$

and the cell centroid radius is an average radius for the cell:

$$y_{c,i,j} = \frac{1}{4} (y_{i+1,j+1} + y_{i+1,j} + y_{i,j+1} + y_{i,j}). \quad (\text{C.17})$$

1. See Hirsch (1988), p. 247.

APPENDIX D

DIAGONALIZATION OF THE FLUX JACOBIANS

The flux Jacobians are required for both the implicit and explicit fluxes. The diagonal implicit scheme approximates only the inviscid fluxes, and only the inviscid fluxes are considered in the upwind schemes. Therefore, the fluxes and their Jacobians discussed in this appendix consider only the inviscid terms. However, the viscous terms *are* included in the flowfield solutions as detailed in section III.4, after the discussion of the TVD method.

The flux Jacobian in the ξ -direction, A , is defined as $\frac{\partial F'_I}{\partial U}$. It is calculated in this form for the implicit side. On the other hand, the upwind schemes (which are used to evaluate the explicit side) require the decomposition of the Jacobians. The diagonalization of A is facilitated immensely through the use of a similarity transformation.

For convenience, the vector of conserved variables, U , and the vector of primitive variables, V , are repeated here:

$$U = (\tilde{\rho}_1, \dots, \tilde{\rho}_{ne}, \rho_{ne+1}, \dots, \rho_{ns}, \rho u, \rho v, \rho E)^T \quad (D.1)$$

$$V = (\tilde{\rho}_1, \dots, \tilde{\rho}_{ne}, \rho_{ne+1}, \dots, \rho_{ns}, u, v, p)^T. \quad (D.2)$$

The rotated, inviscid flux vectors are

$$F'_I = \begin{bmatrix} \tilde{\rho}_1 u' \\ \vdots \\ \tilde{\rho}_{ne} u' \\ \rho_{ne+1} u' \\ \vdots \\ \rho_{ns} u' \\ \rho u u' + p s'_{ix} \\ \rho v u' + p s'_{iy} \\ (\rho E + p) u' \end{bmatrix} \quad G'_I = \begin{bmatrix} \tilde{\rho}_1 v' \\ \vdots \\ \tilde{\rho}_{ne} v' \\ \rho_{ne+1} v' \\ \vdots \\ \rho_{ns} v' \\ \rho u v' + p s'_{jx} \\ \rho v v' + p s'_{jy} \\ (\rho E + p) v' \end{bmatrix}. \quad (D.3)$$

The flux Jacobians required for the implicit side are

A =

$$\begin{bmatrix}
 \tilde{\rho}_1 u' - \frac{\tilde{\rho}_1 u'}{\rho} & \dots & \frac{\tilde{\rho}_1 u'}{\rho} & \dots & \frac{\tilde{\rho}_1 s'_{ix}}{\rho} & \dots & \frac{\tilde{\rho}_1 s'_{iy}}{\rho} & \dots & 0 \\
 \frac{\tilde{\rho}_2 u'}{\rho} & \dots & \dots & \dots & \dots & \dots & \dots & \dots & \dots \\
 \vdots & \dots & \dots & \dots & \dots & \dots & \dots & \dots & \dots \\
 \frac{\tilde{\rho}_{ne} u'}{\rho} & \dots & \frac{\tilde{\rho}_{ne} u'}{\rho} & \dots & \frac{\tilde{\rho}_{ne} s'_{ix}}{\rho} & \dots & \frac{\tilde{\rho}_{ne} s'_{iy}}{\rho} & \dots & 0 \\
 \frac{\rho_{ne+1} u'}{\rho} & \dots & \frac{\rho_{ne+1} u'}{\rho} & \dots & \frac{\rho_{ne+1} s'_{ix}}{\rho} & \dots & \frac{\rho_{ne+1} s'_{iy}}{\rho} & \dots & 0 \\
 \vdots & \dots & \vdots & \dots & \vdots & \dots & \vdots & \dots & \vdots \\
 \vdots & \dots & \vdots & \dots & \vdots & \dots & \vdots & \dots & \vdots \\
 \frac{\rho_{ns} u'}{\rho} & \dots & \frac{\rho_{ns} u'}{\rho} & \dots & \frac{\rho_{ns} s'_{ix}}{\rho} & \dots & \frac{\rho_{ns} s'_{iy}}{\rho} & \dots & 0 \\
 s'_{ix} \frac{\partial p}{\partial \rho_1} - uu' & \dots & s'_{ix} \frac{\partial p}{\partial \tilde{\rho}_{ne}} - uu' & \dots & s'_{ix} \frac{\partial p}{\partial (\rho u)} + us'_{ix} + u' & \dots & s'_{ix} \frac{\partial p}{\partial (\rho v)} + us'_{iy} & \dots & s'_{ix} \frac{\partial p}{\partial (\rho E)} \\
 s'_{iy} \frac{\partial p}{\partial \rho_1} - vu' & \dots & s'_{iy} \frac{\partial p}{\partial \tilde{\rho}_{ne}} - vu' & \dots & s'_{iy} \frac{\partial p}{\partial (\rho u)} + vs'_{ix} & \dots & s'_{iy} \frac{\partial p}{\partial (\rho v)} + vs'_{iy} + u' & \dots & s'_{iy} \frac{\partial p}{\partial (\rho E)} \\
 \left[\frac{\partial p}{\partial \rho_1} - \frac{\rho E + p}{\rho} \right] u' & \dots & \left[\frac{\partial p}{\partial \tilde{\rho}_{ne}} - \frac{\rho E + p}{\rho} \right] u' & \dots & \left[\frac{\partial p}{\partial (\rho u)} + s'_{ix} \right] u' & \dots & \left[\frac{\partial p}{\partial (\rho v)} + s'_{iy} \right] u' & \dots & \left[1 + \frac{\partial p}{\partial (\rho E)} \right] u'
 \end{bmatrix}$$

(D.4)

and $B =$

$$\begin{bmatrix}
 \tilde{\rho}_1 v' - \frac{\tilde{\rho}_1 v'}{\rho} & \dots & \tilde{\rho}_1 v' - \frac{\tilde{\rho}_1 v'}{\rho} & \dots & \tilde{\rho}_1 s'_{jx} & \dots & \tilde{\rho}_1 s'_{jy} & \dots & 0 \\
 \tilde{\rho}_2 u' - \frac{\tilde{\rho}_2 u'}{\rho} & \dots & \dots & \dots & \dots & \dots & \dots & \dots & \dots \\
 \vdots & \dots & \dots & \dots & \dots & \dots & \dots & \dots & \dots \\
 \tilde{\rho}_{ne} v' - \frac{\tilde{\rho}_{ne} v'}{\rho} & \dots & \tilde{\rho}_{ne} v' - \frac{\tilde{\rho}_{ne} v'}{\rho} & \dots & \tilde{\rho}_{ne} s'_{jx} & \dots & \tilde{\rho}_{ne} s'_{jy} & \dots & 0 \\
 \rho_{ne+1} v' - \frac{\rho_{ne+1} v'}{\rho} & \dots & \rho_{ne+1} v' - \frac{\rho_{ne+1} v'}{\rho} & \dots & \rho_{ne+1} s'_{jx} & \dots & \rho_{ne+1} s'_{jy} & \dots & 0 \\
 \vdots & \dots & \vdots & \dots & \vdots & \dots & \vdots & \dots & \vdots \\
 \vdots & \dots & \vdots & \dots & \vdots & \dots & \vdots & \dots & \vdots \\
 \rho_{ns} v' - \frac{\rho_{ns} v'}{\rho} & \dots & \rho_{ns} v' - \frac{\rho_{ns} v'}{\rho} & \dots & \rho_{ns} s'_{jx} & \dots & \rho_{ns} s'_{jy} & \dots & 0 \\
 s'_{jx} \frac{\partial p}{\partial \rho_1} - uv' & \dots & s'_{jx} \frac{\partial p}{\partial \rho_{ne}} - uv' & \dots & s'_{jx} \frac{\partial p}{\partial \rho_{ns}} + us'_{jx} + v' & \dots & s'_{jx} \frac{\partial p}{\partial (\rho v)} + us'_{jy} & \dots & s'_{jx} \frac{\partial p}{\partial (\rho E)} \\
 s'_{jy} \frac{\partial p}{\partial \rho_1} - vv' & \dots & s'_{jy} \frac{\partial p}{\partial \rho_{ne}} - vv' & \dots & s'_{jy} \frac{\partial p}{\partial \rho_{ns}} + vs'_{jx} & \dots & s'_{jy} \frac{\partial p}{\partial (\rho v)} + vs'_{jy} + v' & \dots & s'_{jy} \frac{\partial p}{\partial (\rho E)} \\
 \left[\frac{\partial p}{\partial \rho_1} - \frac{\rho E + p}{\rho} \right] v' & \dots & \left[\frac{\partial p}{\partial \rho_{ne}} - \frac{\rho E + p}{\rho} \right] v' & \dots & v' \frac{\partial p}{\partial \rho_{ns}} + s'_{jx} \frac{\rho E + p}{\rho} & \dots & v' \frac{\partial p}{\partial (\rho v)} + s'_{jy} \frac{\rho E + p}{\rho} & \dots & \left[1 + \frac{\partial p}{\partial (\rho E)} \right] v'
 \end{bmatrix}$$

(D.5)

The derivatives of the pressure with respect to the conserved variables are

$$\frac{\partial p}{\partial \tilde{\rho}_e} = \sum_{r=1}^{ne} \beta_{re} \left[\left(\frac{R}{M_r} - (\gamma-1) c_{v,r} \right) T - (\gamma-1) E_{v,r} + h_r^o \right] + (\gamma-1) \frac{u^2 + v^2}{2} \quad (\text{D.6})$$

$$\begin{aligned} \frac{\partial p}{\partial \rho_s} = \sum_{r=1}^{ne} \beta_{rs} \left[\left(\frac{R}{M_r} - (\gamma-1) c_{v,r} \right) T - (\gamma-1) E_{v,r} + h_r^o \right] + \\ \left(\frac{R}{M_s} - (\gamma-1) c_{v,s} \right) T - (\gamma-1) E_{v,s} + h_s^o \end{aligned} \quad (\text{D.7})$$

$$\frac{\partial p}{\partial (\rho u)} = -(\gamma-1) u \quad (\text{D.8})$$

$$\frac{\partial p}{\partial (\rho v)} = -(\gamma-1) v \quad (\text{D.9})$$

$$\frac{\partial p}{\partial (\rho E)} = \gamma - 1. \quad (\text{D.10})$$

In these equations,

$$\gamma = 1 + \frac{\rho R}{\rho \bar{C}_v + \sum_{s=1}^{nv} \rho_s c_{v, \text{vib}, s}}, \quad (\text{D.11})$$

$$\rho \bar{C}_v = \sum_{s=1}^{ns} \rho_s c_{v, s}, \quad (\text{D.12})$$

and

$$\rho R = \sum_{s=1}^{ns} \rho_s \frac{R}{M_s}. \quad (\text{D.13})$$

Recall that $c_{v, s}$ contains only contributions from translational and rotational energy; the vibrational energy contribution is handled separately in $c_{v, \text{vib}, s}$. The definitions of $E_{v, s}$ and $c_{v, \text{vib}, s}$ are given in section II.3 and II.5, respectively, but are repeated here for convenience:

$$E_{v, s} = \frac{R}{M_s} \sum_{m=1}^{ndeg(s)} \left[\frac{\theta_{v, s, m}}{\exp\left(\frac{\theta_{v, s, m}}{T}\right)} \right], \quad (\text{D.14})$$

$$c_{v, \text{vib}, s} = \frac{\partial E_{v, s}}{\partial T} = \frac{R}{M_s} \sum_{m=1}^{ndeg(s)} \frac{\left(\frac{\theta_{v, s, m}}{T}\right)^2 \exp\left(\frac{\theta_{v, s, m}}{T}\right)}{\left[\exp\left(\frac{\theta_{v, s, m}}{T}\right) - 1\right]^2}. \quad (\text{D.15})$$

For the explicit discretization the Jacobians are decomposed. The Jacobian A can be diagonalized to

$$A = P_A \Lambda_A P_A^{-1}, \quad (\text{D.16})$$

where Λ_A is a diagonal matrix, with the diagonal comprised of the eigenvalues of A , and the columns of P_A are the corresponding right eigenvectors. In practice it is difficult to find the eigenvalues and eigenvectors by directly decomposing A .

Using the identity matrix and the chain rule, the Jacobian can be expressed as

$$A = I \frac{\partial F'_I}{\partial V} \frac{\partial V}{\partial U} = \frac{\partial U}{\partial V} \frac{\partial V}{\partial U} \frac{\partial F'_I}{\partial V} \frac{\partial V}{\partial U}. \quad (\text{D.17})$$

Defining

$$M = \frac{\partial U}{\partial V} \quad (\text{D.18})$$

and

$$\tilde{A} = \frac{\partial V}{\partial U} \frac{\partial F'_I}{\partial V}, \quad (\text{D.19})$$

equation D.14 is rewritten

$$A = M \tilde{A} M^{-1}. \quad (\text{D.20})$$

Through the use of the similarity transformation just described, the determination of the eigenvalues is considerably simplified. The decomposition of \tilde{A} is

$$\tilde{A} = P_{\tilde{A}} \Lambda_{\tilde{A}} P_{\tilde{A}}^{-1}. \quad (\text{D.21})$$

The eigenvalues of A are the same as of \tilde{A} , but the diagonalization of \tilde{A} is much easier to accomplish because of its simpler structure. The right eigenvalues of \tilde{A} and A are related by

$$P_A = M P_{\tilde{A}}. \quad (\text{D.22})$$

In a similar fashion the flux Jacobian in the η -direction can be expressed as

$$B = I \frac{\partial G'_I}{\partial V} \frac{\partial V}{\partial U} = \frac{\partial U}{\partial V} \frac{\partial V}{\partial U} \frac{\partial G'_I}{\partial V} \frac{\partial V}{\partial U} = M \tilde{B} M^{-1}. \quad (\text{D.23})$$

The matrix M is

$$M = \begin{bmatrix} 1 & 0 & \dots & 0 \\ 0 & \ddots & \ddots & \vdots \\ \vdots & \ddots & \ddots & 0 \\ 0 & \dots & 0 & 1 \\ & & & 1 & 0 & \dots & 0 \\ & & & 0 & \ddots & \ddots & \vdots \\ & & & \vdots & \ddots & \ddots & 0 \\ & & & 0 & \dots & 0 & 1 \\ u & \dots & \dots & u & & \rho & 0 & 0 \\ v & \dots & \dots & v & & 0 & \rho & 0 \\ \frac{\partial \rho E}{\partial \tilde{\rho}_1} & \dots & \dots & \frac{\partial \rho E}{\partial \tilde{\rho}_{ne}} & \frac{\partial \rho E}{\partial \rho_{ne+1}} & \dots & \dots & \frac{\partial \rho E}{\partial \rho_{ns}} & \frac{\partial \rho E}{\partial u} & \frac{\partial \rho E}{\partial v} & \frac{\partial \rho E}{\partial p} \end{bmatrix}. \quad (\text{D.24})$$

The terms in the last row are

$$\frac{\partial (\rho E)}{\partial \tilde{\rho}_e} = \sum_{r=1}^{ne} \beta_{re} \left[\left(c_{v,r} - \frac{R}{M_r} \frac{1}{\gamma-1} \right) T + h_r^o + E_{v,r} \right] + \frac{u^2 + v^2}{2} \quad (\text{D.25})$$

$$\begin{aligned} \frac{\partial (\rho E)}{\partial \rho_s} &= \sum_{r=1}^{ne} \beta_{rs} \left[\left(c_{v,r} - \frac{R}{M_r} \frac{1}{\gamma-1} \right) T + h_r^o + E_{v,r} \right] + \\ &\quad \left(c_{v,s} - \frac{R}{M_s} \frac{1}{\gamma-1} \right) T + h_s^o + E_{v,s} \end{aligned} \quad (\text{D.26})$$

$$\frac{\partial}{\partial u} (\rho E) = \rho u \quad (\text{D.27})$$

$$\frac{\partial}{\partial v} (\rho E) = \rho v \quad (\text{D.28})$$

$$\frac{\partial (\rho E)}{\partial p} = \frac{1}{\gamma-1}. \quad (\text{D.29})$$

The matrix M^{-1} can be determined by inversion of M , but it is simpler to calculate it directly. It is

This is not a frozen or an equilibrium speed of sound; the composition of the gas is accounted for in γ and \bar{R} .

The eigenvalues of \tilde{A} satisfy

$$\det(\tilde{A} - \lambda_{\tilde{A}} I) = 0. \quad (\text{D.36})$$

Solving this equation, the eigenvalues are

$$\Lambda_{\tilde{A}} = \begin{bmatrix} u' & & & & \\ & \ddots & & & \\ & & u' & & \\ & & & u'+a & \\ & & & & u'-a \end{bmatrix}. \quad (\text{D.37})$$

The eigenvalue u' is repeated ns times; for the equation set described in the Chapter II, there are $ns + 3$ equations and thus $ns + 3$ eigenvalues.

For the η -direction, the result is

$$\Lambda_{\tilde{B}} = \begin{bmatrix} v' & & & & \\ & \ddots & & & \\ & & v' & & \\ & & & v'+a & \\ & & & & v'-a \end{bmatrix}, \quad (\text{D.38})$$

The order of the eigenvalues is arbitrary; however, the eigenvectors should be in the same order as the eigenvalues.

The right eigenvectors of \tilde{A} are solutions to

$$(\tilde{A} - \lambda_{\tilde{A}} I)\tilde{x} = 0, \quad (\text{D.39})$$

where \tilde{x} is the eigenvector corresponding to the eigenvalue $\lambda_{\tilde{A}}$. It turns out the eigenvectors of \tilde{A} are not unique; there are many arbitrary constants allowed. The choice of these constants can affect the convergence of the numerical scheme.¹ Selections for the arbitrary constants are made such that the eigenvectors are linearly independent. In this thesis the following eigenvectors are employed:

1. See Yee(1989).

$$P_{\tilde{A}} = \begin{bmatrix} \frac{1}{a^2} & & & & \frac{\tilde{\rho}_1}{\rho a^2} & \frac{\tilde{\rho}_1}{\rho a^2} \\ & \ddots & & & \vdots & \vdots \\ & & \frac{1}{a^2} & & \frac{\tilde{\rho}_{ne}}{\rho a^2} & \frac{\tilde{\rho}_{ne}}{\rho a^2} \\ & & & \ddots & \vdots & \vdots \\ & & & & \frac{\rho_{ne+1}}{\rho a^2} & \frac{\rho_{ne+1}}{\rho a^2} \\ & & & & \vdots & \vdots \\ & & & & \frac{1}{a^2} & \frac{\rho_{ns}}{\rho a^2} \\ & & & & & \frac{\rho_{ns}}{\rho a^2} \\ & & & & \frac{s'_{iy}}{\rho a} & \frac{-s'_{ix}}{\rho a} & \frac{s'_{ix}}{\rho a} \\ & & & & \frac{-s'_{ix}}{\rho a} & \frac{-s'_{iy}}{\rho a} & \frac{s'_{iy}}{\rho a} \\ & & & & 0 & 1 & 1 \end{bmatrix} \quad (\text{D.40})$$

and

$$P_{\tilde{B}} = \begin{bmatrix} \frac{1}{a^2} & & & & \frac{\tilde{\rho}_1}{\rho a^2} & \frac{\tilde{\rho}_1}{\rho a^2} \\ & \ddots & & & \vdots & \vdots \\ & & \frac{1}{a^2} & & \frac{\tilde{\rho}_{ne}}{\rho a^2} & \frac{\tilde{\rho}_{ne}}{\rho a^2} \\ & & & \ddots & \vdots & \vdots \\ & & & & \frac{\rho_{ne+1}}{\rho a^2} & \frac{\rho_{ne+1}}{\rho a^2} \\ & & & & \vdots & \vdots \\ & & & & \frac{1}{a^2} & \frac{\rho_{ns}}{\rho a^2} \\ & & & & & \frac{\rho_{ns}}{\rho a^2} \\ & & & & \frac{s'_{jy}}{\rho a} & \frac{-s'_{jx}}{\rho a} & \frac{s'_{jx}}{\rho a} \\ & & & & \frac{-s'_{jx}}{\rho a} & \frac{-s'_{jy}}{\rho a} & \frac{s'_{jy}}{\rho a} \\ & & & & 0 & 1 & 1 \end{bmatrix} \quad (\text{D.41})$$

These matrices are inverted to obtain $P_{\tilde{A}}^{-1}$ and $P_{\tilde{B}}^{-1}$:

$$P_{\tilde{A}}^{-1} = \begin{bmatrix} a^2 & & & & & & \frac{\tilde{\rho}_1}{\rho} \\ & \ddots & & & & & \vdots \\ & & a^2 & & & & \frac{\tilde{\rho}_{ne}}{\rho} \\ & & & a^2 & & & \frac{\rho_{ne+1}}{\rho} \\ & & & & \ddots & & \vdots \\ & & & & & a^2 & \frac{\rho_{ns}}{\rho} \\ & & & & & & 0 \\ & & & & & \frac{\rho as_{iy}'}{2} & \frac{-\rho as_{ix}'}{2} \\ & & & & & \frac{-\rho as_{ix}'}{2} & \frac{-\rho as_{iy}'}{2} \\ & & & & & \frac{\rho as_{ix}'}{2} & \frac{\rho as_{iy}'}{2} \end{bmatrix} \quad (D.42)$$

and

$$P_{\tilde{B}}^{-1} = \begin{bmatrix} a^2 & & & & & & \frac{\tilde{\rho}_1}{\rho} \\ & \ddots & & & & & \vdots \\ & & a^2 & & & & \frac{\tilde{\rho}_{ne}}{\rho} \\ & & & a^2 & & & \frac{\rho_{ne+1}}{\rho} \\ & & & & \ddots & & \vdots \\ & & & & & a^2 & \frac{\rho_{ns}}{\rho} \\ & & & & & & 0 \\ & & & & & \frac{\rho as_{jy}'}{2} & \frac{-\rho as_{jx}'}{2} \\ & & & & & \frac{-\rho as_{jx}'}{2} & \frac{-\rho as_{jy}'}{2} \\ & & & & & \frac{\rho as_{jx}'}{2} & \frac{\rho as_{jy}'}{2} \end{bmatrix} \quad (D.43)$$

The eigenvectors of A and B are

$$P_A = \begin{bmatrix} \frac{1}{a^2} & & & & & & \frac{\tilde{\rho}_1}{\rho a^2} & \frac{\tilde{\rho}_1}{\rho a^2} \\ & \ddots & & & & & \vdots & \vdots \\ & & \frac{1}{a^2} & & & & \frac{\tilde{\rho}_{ne}}{\rho a^2} & \frac{\tilde{\rho}_{ne}}{\rho a^2} \\ & & & \frac{1}{a^2} & & & \frac{\rho_{ne+1}}{\rho a^2} & \frac{\rho_{ne+1}}{\rho a^2} \\ & & & & \ddots & & \vdots & \vdots \\ & & & & & \frac{1}{a^2} & \frac{\rho_{ns}}{\rho a^2} & \frac{\rho_{ns}}{\rho a^2} \\ \frac{u}{a^2} & \cdots & \frac{u}{a^2} & & & & \frac{s'_{iy}}{a} & \frac{u - as'_{ix}}{a^2} & \frac{u + as'_{ix}}{a^2} \\ \frac{v}{a^2} & \cdots & \frac{v}{a^2} & & & & \frac{-s'_{ix}}{a} & \frac{v - as'_{iy}}{a^2} & \frac{v + as'_{iy}}{a^2} \\ \frac{1}{a^2} \frac{\partial(\rho E)}{\partial \tilde{\rho}_1} & \cdots & \frac{1}{a^2} \frac{\partial(\rho E)}{\partial \tilde{\rho}_{ne}} & \frac{1}{a^2} \frac{\partial(\rho E)}{\partial \rho_{ne+1}} & \cdots & \frac{1}{a^2} \frac{\partial(\rho E)}{\partial \rho_{ns}} & \frac{-v'}{a} & \frac{\rho E + p}{\rho a^2} - \frac{u'}{a} & \frac{\rho E + p}{\rho a^2} + \frac{u'}{a} \end{bmatrix} \quad (D.44)$$

$$P_B = \begin{bmatrix} \frac{1}{a^2} & & & & & & \frac{\tilde{\rho}_1}{\rho a^2} & \frac{\tilde{\rho}_1}{\rho a^2} \\ & \ddots & & & & & \vdots & \vdots \\ & & \frac{1}{a^2} & & & & \frac{\tilde{\rho}_{ne}}{\rho a^2} & \frac{\tilde{\rho}_{ne}}{\rho a^2} \\ & & & \frac{1}{a^2} & & & \frac{\rho_{ne+1}}{\rho a^2} & \frac{\rho_{ne+1}}{\rho a^2} \\ & & & & \ddots & & \vdots & \vdots \\ & & & & & \frac{1}{a^2} & \frac{\rho_{ns}}{\rho a^2} & \frac{\rho_{ns}}{\rho a^2} \\ \frac{u}{a^2} & \cdots & \frac{u}{a^2} & & & & \frac{s'_{jy}}{a} & \frac{u - as'_{jx}}{a^2} & \frac{u + as'_{jx}}{a^2} \\ \frac{v}{a^2} & \cdots & \frac{v}{a^2} & & & & \frac{-s'_{jx}}{a} & \frac{v - as'_{jy}}{a^2} & \frac{v + as'_{jy}}{a^2} \\ \frac{1}{a^2} \frac{\partial(\rho E)}{\partial \tilde{\rho}_1} & \cdots & \frac{1}{a^2} \frac{\partial(\rho E)}{\partial \tilde{\rho}_{ne}} & \frac{1}{a^2} \frac{\partial(\rho E)}{\partial \rho_{ne+1}} & \cdots & \frac{1}{a^2} \frac{\partial(\rho E)}{\partial \rho_{ns}} & \frac{u'}{a} & \frac{\rho E + p}{\rho a^2} - \frac{v'}{a} & \frac{\rho E + p}{\rho a^2} + \frac{v'}{a} \end{bmatrix} \quad (D.45)$$